DE GRUYTER Radiochim. Acta 2022; aop

Review

Kai Li, Wei Liu, Hailong Zhang, Liwei Cheng, Yugang Zhang, Yaxing Wang*, Ning Chen*, Congqing Zhu*, Zhifang Chai and Shuao Wang*

Progress in solid state and coordination chemistry of actinides in China

https://doi.org/10.1515/ract-2022-0024
Received February 7, 2022; accepted August 24, 2022;

Abstract: In the past decade, the area of solid state chemistry of actinides has witnessed a rapid development in China, based on the significantly increased proportion of the number of actinide containing crystal structures reported by Chinese researchers from only 2% in 2010 to 36% in 2021. In this review article, we comprehensively overview the synthesis, structure, and characterizations of representative actinide solid compounds including oxo-compounds, organometallic compounds, and endohedral metallofullerenes reported by Chinese researchers. In addition, Chinese researchers pioneered several potential applications of actinide solid compounds in terms of adsorption, separation, photoelectric materials, and photo-catalysis, which are also briefly discussed. It is our hope that this contribution not only calls for further development of this area in China, but also arouses new research directions and interests in actinide chemistry and material sciences.

Keywords: Chinese researchers; endohedral metallofullerenes; organometallic compounds; oxo-compounds; solid state chemistry of actinides.

1 Introduction

In the face of increasingly serious environmental pollution and carbon dioxide emissions, nuclear power can not only provide a stable energy supply, but can also partly alleviate the current environmental pollution, having become an important alternative to traditional fossil energy. The International Atomic Energy Agency (IAEA) predicts that by 2050, the potential of global nuclear power will remain high, and it will be mainly concentrated in Asia, especially in China [1]. Currently, as of September 2021, the mainland of China has 52 nuclear reactors in operation with a capacity of 53.49 GW, and its nuclear power accounts for 4.99% of the total power generation. However, with the rapid development of nuclear energy, nuclear fuel reprocessing and waste disposal, which are closely related to the nuclear energy, are facing unprecedented challenges, and have become one of the critical factors restricting the sustainable development of nuclear energy in China. Therefore, the study of actinides, the key elements in nuclear fuel reprocessing and waste disposal, is of great significance.

Actinides, generally referring to elements 90–103, actinium through lawrencium, are essentially unique in the Periodic Table of elements not only because there is no stable isotope for these elements, but also given by their great complexities in chemical bonding, electronic structure, speciation, valence state, redox chemistry, and coordination geometry [2]. A clear understanding of the chemical behaviors of actinide solid compounds is essential for designing waste forms for geological disposal and predicting the fate and remediation of actinide radionuclides in the environment. Over the past decades, significant amounts of actinide

---

The authors Kai Li, Wei Liu, Hailong Zhang, Liwei Cheng, Yugang Zhang have contributed equally to this work.

***Corresponding authors: Shuao Wang and Yaxing Wang**, State Key Laboratory of Radiation Medicine and Protection, School for Radiological and Interdisciplinary Sciences (RAD-X) and Collaborative Innovation Center of Radiation Medicine of Jiangsu Higher Education Institutions, Soochow University, Suzhou, 215123, China, E-mail: shuaowang@suda.edu.cn (S. Wang), yxwang@suda.edu.cn (Y. Wang); **Ning Chen**, College of Chemistry, Chemical Engineering and Materials Science and State Key Laboratory of Radiation Medicine and Protection, Soochow University, Suzhou, Jiangsu, 215123, China, E-mail: chenning@suda.edu.cn; and **Congqing Zhu**, State Key Laboratory of Coordination Chemistry, Jiangsu Key Laboratory of Advanced Organic Materials, School of Chemistry and Chemical Engineering, Nanjing University, Nanjing, 210023, China, E-mail: zcq@nju.edu.cn
Kai Li, Hailong Zhang, Liwei Cheng, Yugang Zhang and Zhifang Chai, State Key Laboratory of Radiation Medicine and Protection, School for Radiological and Interdisciplinary Sciences (RAD-X) and Collaborative Innovation Center of Radiation Medicine of Jiangsu Higher Education Institutions, Soochow University, Suzhou, 215123, China
Wei Liu, School of Environmental and Material Engineering, Yantai University, Yantai, 264005, China

solid compounds, mainly actinide oxocompounds, actinide organometallic compounds and actinide endohedral metallofullerenes, have been synthesized and comprehensively characterized by researchers in China. The majority of known actinide solid compounds in the literature were synthesized under relatively mild conditions including ambient conditions and mild hydrothermal reactions in the temperature range from 100 to 240 °C. Investigations on actinide compounds synthesized at higher temperatures from 300 to 2500 °C and higher pressures (greater than 22.1 MPa) have also been conducted. In addition, the synthesis of actinide solid compounds under harsh conditions, such as anhydrous and anaerobic conditions, has also been reported, mainly focusing on the synthesis of actinide organometallic compounds. In recent years, as shown in Figure 1, approximately 16 universities and research institutes in China have been carrying out actinide solid chemistry research. Obviously, compared with the solid state chemistry of other elements, the universities and research institutes engaged in the study of actinide solid state chemistry in China are quite limited.

Due to the inherent radioactivity and chemotoxicity of actinides, and the lack of corresponding experimental platforms, the study of actinide solid state chemistry is still in its infancy in China. In addition, our current knowledge on the solid state chemistry of actinides is still predominantly limited to thorium and uranium, most likely because of their relatively low chemotoxicity and radiotoxicity and their relatively high natural abundance. Unlike thorium and uranium, transuranium elements starting from neptunium can only be handled in a few specially designed radiochemical laboratories in China. The number of reported crystal structures of thorium and uranium in China reaches 1200; in contrast, the number of entries of transuranic crystals structures is only 4. Fortunately, with the rapid development of nuclear energy in China, researchers working on actinide solid state chemistry have grown significantly in recent years. We summarized the actinide solid compounds reported in the Cambridge Structural Database. Since 2010, the proportion of actinide crystals structures reported herein from in China has been increasing, gradually from less than 2% in 2000–2011 to 36% in 2020–2021 years.

Recently, in addition to the synthesis and characterization of actinide solid compounds, research on their remarkable potential functional materials has also been gradually emerging. Actinide functional compounds have

Figure 1: Actinide solid state chemistry research-related universities and institutes in China.

a wide range of applications in adsorption separation, photoelectric functional materials, and catalysis. The development of actinide functional materials can not only obtain unparalleled high-performance materials but also further deepen the understanding of the physical and chemical properties of actinides, which is of great significance in the development of actinide solid state chemistry.

2 Preparation, structure and characterization of actinide compounds

2.1 Actinide oxocompounds

2.1.1 Inorganic actinide oxocompounds

2.1.1.1 High-temperature, high-pressure (HTHP) hydrothermal method

The majority of known actinide solid compounds in the literature were synthesized under relatively mild conditions including ambient conditions and mild hydrothermal reactions in the temperature range from 100 to 240 °C. Investigations on actinide compounds synthesized at a higher temperature from 300 to 2500 °C and higher pressure (greater than 22.1 MPa) have been conducted but are significantly scarce. High pressure can be either achieved externally or autogenously in a sealed vessel with solvent (i.e. supercritical water synthesis). Under conditions with much-elevated temperature and pressure, the chemical reactions can be efficiently accelerated and the redox chemistry of actinides is significantly shifted compared to those under milder conditions. In addition, the electronic structure of actinides would significantly vary, leading to corresponding changes in the bonding, structure, and properties of the solid compounds. However, the topic of externally-induced high temperature and high-pressure synthesis of actinide compounds is also in its infancy. The only previous investigations of solid-state chemistry of actinides under supercritical water conditions are limited only within the systems of uranium silicate, germanate, phosphate and arsenate, which were mainly reported by Lii et al.

The high-temperature, high-pressure (HTHP) hydrothermal method facilitates crystal growth and the formation of compounds with elements in oxidation states that are difficult to obtain under ambient condition. Of note, Chen et al. synthesized the first U(V) silicate, $K(UO)Si_2O_6$, which is also the first U(V) compound synthesized by the hydrothermal method. Its three-dimensional framework is uniquely characterized by four-membered single rings of corner-sharing SiO_4 tetrahedra and strings of U^VO_6 octahedra sharing opposite corners to give infinite –U–O–U–O– chains [3, 4]. In addition, a large number of uranyl compounds [5–9], several uranium (V) compounds, some uranium (IV) compounds [10, 11], and mixed-valence uranium (IV, V) [12], -(IV, VI) [13], -(V, VI) [14, 15], and -(IV, V, VI) [16] silicates and germanates were synthesized by a high-temperature, high-pressure hydrothermal method, which was nearly impossible to synthesize under normal conditions. However, relative studies on other actinide-bearing oxysalts synthesized by the HTHP hydrothermal method have never been reported, except for silicates, germanates, phosphate, and arsenate [17, 18]. Therefore, further research to synthesize new actinide-bearing compounds, especially neptunium, plutonium, and americium, with a new network and unusual oxidation state will help us better understand the chemical behavior of actinides.

2.1.1.2 Low-temperature melting flux method

The molten flux of inorganic acid at 180–280 °C is a safe and facile way to prepare actinide oxocompounds. Due to the rich combinations of BO_3 triangles and BO_4 tetrahedra with various valent actinides, many new actinide borates have been obtained using molten boric acid as a flux. In 2016, Xu et al. reported a 3D actinyl borate framework, $K([UO_2][B_6O_{10}OH])$ (**KUBO-4**), which was synthesized by a flux reaction at 250 °C. **KUBO-4** crystallizes in the space group *Ama*2 [19]. The actinyl unit prefers equatorial coordination with oxygen donors, which results in the dominance of the layer structure. Each UO_8 unit is surrounded by nine borate groups, including three vertex-sharing BO_3 triangles, three vertex sharing BO_4 tetrahedra, and three edge-sharing BO_4 tetrahedra. Between the adjacent layers, there are diborate B_2O_5 units that consist of two vertex-sharing BO_3 triangles, which bridge adjacent uranyl layers into a three-dimensional framework. Potassium ions are located in the void spaces.

In 2017, Wang et al. reported four new actinide iodates yielded from periodic acid flux reactions at 180 °C [20]. $UO_2(IO_3)_2 \cdot H_2O$ and $UO_2(IO_3)_2(H_2O) \cdot HIO_3$ crystallize in the space groups of $Pna2_1$ and $P2_1/c$, respectively. They exhibit pillared structures consisting of uranyl pentagonal bipyramids and iodate trigonal pyramids. α-$Th(IO_3)_2(NO_3)(OH)$ and β-$Th(IO_3)_2(NO_3)(OH)$ were isolated from the same reaction, and they crystallized in the space groups of *P*-1 and *Pbca*, respectively. They represent two new thorium iodates that are constructed from subunits of thorium dimers that were first observed in the extensive structures of thorium iodates. The structures of these compounds deviate from those afforded from hydrothermal reactions, implying that periodic acid flux could be a new synthetic route toward new iodates.

2.1.1.3 Ionothermal method

Ionic liquids have the advantages of low vapor pressure, good stability, and high solubility. Ionothermal synthesis is a synthesis method in ionic liquids. In ionothermal reactions, the hydrolysis/solvation of actinide cations is effectively avoided. In 2016, Gui et al. reported a thorium(IV) mixed phosphite/pyrophosphate $[BMMim]_2(Th_3[PO_3]_4[H_2P_2O_7]_3)$ (**ThP-1**) (BMMim = 1-butyl-2,3-dimethylimidazolium), synthesized from the ionothermal reaction in 1-butyl-2,3-dimethylimidazolium chloride at 160 °C [21]. Pyrophosphate was formed *in situ* and took part in coordination and crystallization. **ThP-1** crystallizes in the space group *Pm*-3*m*. The thorium center is eight-coordinated with four oxygen atoms provided by four different phosphite ligands and the other four oxygen atoms from two separated chelating pyrophosphate ligands.

In 2019, Gui et al. reported a two-dimensional layered architecture $(H_3O)_4UO_2(PO_4)_2$ (**HUP-1**), by ionothermal reaction in 1-butyl2,3-dimethylimidazolium chloride at 180 °C [22]. **HUP-1** crystallizes in tetragonal space group *I*4*m*2. UO_2^{2+} is equatorially coordinated by four oxygen atoms from four different phosphate groups, resulting in tetragonal bipyramid coordination geometry. UO_6 tetragonal bipyramids and PO_4 tetrahedra are further connected in a corner-sharing manner to achieve uranium phosphate anionic layers of $(UO_2[PO_4]_2)^{4-}$. Charge-balancing hydronium cations are accommodated between the adjacent layers, where the interlayer spacing is 6.373 Å.

2.1.1.4 Hydrothermal method

Hydrothermal synthesis refers to the chemical reaction of substances in aqueous media above 100 °C and 1 bar. Under hydrothermal conditions, the reaction activity of reactants is increased because the reaction is at the molecular level. Due to the accessibility of hydrothermal synthesis, abundant actinide structures were synthesized, including actinide phosphates, sulfates selenites/selenates, iodates, molybdates, vanadates, germinates, etc.

In 2015, $ThF_2(SO_4)(H_2O)$ was successfully isolated by Zhao et al. from hydrothermal reactions at 220 °C [23]. This compound crystallizes in space group, *P*21/*n*. The thorium center is bonded to nine donor atoms, with four sulfate oxygen atoms, four fluorine atom, and one water molecule, forming the ThO_5F_4 polyhedron, which is best described as the tricapped trigonal prism.

In 2016, Wang et al. reported a thorium iodate vanadate $Th(H_2O)(I^{V}O_3)_2(I^{VII}{}_{0.6}V_{1.76}O_7[OH])$ (**ThIVO**), which was isolated from the hydrothermal reaction at 180 °C [24]. **ThIVO** crystallizes in the triclinic space group *P*-1. The structure can be constructed from three fragments: ThO_9 polyhedra, IO_3 trigonal pyramids, and $(I^{VII}{}_{0.6}V_{1.76}O_7[OH])^{2-}$ chains. The Th center is bound by nine oxygen atoms, which are provided by IO_3, VO_6, VO_4, and a coordinated water molecule, forming a tricapped trigonal prism.

Furthermore, in 2017, four novel thorium selenates were reported through systematic control of the molar ratio between thorium hydroxides and selenic acid and their reaction temperature under hydrothermal conditions [25]. The formation of these compounds suggests that variables including acidity and temperature play a critical role in the hydrolysis and oligomerization of Th(IV) ions. The 3D structure is constructed from ThO_8 polyhedra surrounded by an XO_3 trigonal pyramid (X = I/Se). This is the first example of aliovalent substitution between IO_3^- and SeO_3^{2-} sharing the same lattice site.

In 2018, a cationic lamellar material $(Th[MoO_4][H_2O]_4Cl)Cl{\cdot}H_2O$ (**TMC**), was obtained through hydrothermal reactions at 230 °C [26]. **TMC** crystallizes in the space group *P*21/*m* and adopts a cationic layer structure. The coordination environment of Th^{4+} is composed of four O atoms donated from MoO_4^{2-}, four O atoms donated from H_2O molecules, and one Cl^- ion, forming a capped square antiprismatic geometry. The MoO_4^{2-} anion provides all four O atoms and serves as bridges to connect adjacent Th polyhedra, giving zigzagging $(Th[MoO_4][H_2O]_4Cl)^+$ layers. The distance between layers is approximately 4.7 Å with Cl^- residing as charge-balancing anions.

Two new uranyl vanadates were prepared in 2015 from hydrothermal reactions at 200 °C [27]. $(H_3O)UO_2VO_4$ (**UVO-1**) is an anionic layer structure built from UO_2^{2+} pentagonal bipyramids coordinated by edge-sharing VO_5 square pyramids, with the charge balanced by interlayer H_3O^+ cations. $(UO_2)_3(VO_4)_2(H_2O)_3$ (**UVO-2**) is a 3D uranyl(VI) vanadate framework built from monomeric VO_4 tetrahedra coordinating to UO_2^{2+} pentagonal bipyramids. With the addition of $Ln(NO_3)_3$ (Ln = Nd, Eu) in the reactions, it can give heterobimetallic lanthanide uranyl vanadate compounds.

Furthermore, a new heterobimetallic uranium(IV)/vanadium(III) phosphite, $Na_2UV_2(HPO_3)_6$ (**UVP**), was prepared in 2018 from a hydrothermal reaction at 220 °C [28]. U(IV) was generated from the *in situ* reduction of U(VI) and V(III) from V(V), with phosphite as a reductant. Similarly, a novel cesium uranium(IV) sulfate trimer $Cs_4(U_3O[SO_4]_7){\cdot}2.2H_2O$ was obtained by utilizing zinc amalgam as a reductant in a hydrothermal reaction at 150 °C [29]. This compound crystallizes in the space group *P*-3, which possesses a 2D layer structure with open channels. The anionic

$(U_3O[SO_4]_7)^{4-}$ layer is composed of $(U^{IV}{}_3[\mu_3{-}O])^{10+}$ trinuclear cores decorated by three $SO_4{}^{2-}$ ligands.

In 2019, a uranyl molybdate, $Na_2UO_2(MoO_4)_2{\cdot}(H_2O)$ (UMO) was synthesized, which is easily isolated from the hydrothermal reaction at 200 °C [30]. The **UMO** crystallizes in the orthorhombic system in the $P2_12_12_1$ space group. The structure of **UMO** can be viewed as a 3D framework constructed by UO_7 pentagonal bipyramids and monomeric MoO_4 tetrahedra, with the Na^+ ions located in the channel.

`In 2020, two new uranyl zinc germanates were prepared by a solvothermal reaction at 220 °C, namely $(UO_2)_4(ZnO)(Ge_2O_7)_2{\cdot}(H_3O)_4$ (**UZG-1**), and $(UO_2)_3(Zn[H_2O]_3)(GeO_4)_2$ (**UZG-2**) [31]. **UZG-1** and **UZG-2** are constructed from anionic $([UO_2]_4[Ge_2O_7]_2)^{4-}$ and $([UO_2]_3[Ge_2O_8])^{2-}$ 3D open frameworks, respectively, with channels nested with Zn^{2+} cations. Notably, rather unusual heterometallic $U^{VI}{=}O_{yl}{-}Zn^{II}$ CCIs have been identified in both complexes.

2.1.1.5 Solution method

The solution method is a mild synthesis method in which the reactant is dissolved in a solvent and the solute is precipitated as a crystal from a saturated solution obtained by changing the conditions. In 2021, Wang et al. reported an inorganic uranyl phosphate-polyoxometalate of $Na_{17}\{Na@([SbW_9O_{33}]_2[UO_2]_6[PO_3OH]_6)\}{\cdot}xH_2O$ (abbreviated as $\mathbf{Na@U_6P_6}$, with x ≈ 46) synthesized from the reaction of $SbCl_3$, $NaOAc{\cdot}3H_2O$, $Na_2WO_4{\cdot}2H_2O$, H_3PO_4, and $UO_2(NO_3)_2{\cdot}6H_2O$ in aqueous solution at 95 °C [32]. Trilacunary $[\alpha\text{-B-}SbW_9O_{33}]^{9-}$ was formed *in situ* during the reaction. $\mathbf{Na@U_6P_6}$ crystallizes in the triclinic *P*-1 space group and displays a sandwich structure. The cluster of $\{Na@([SbW_9O_{33}]_2[UO_2]_6[PO_3OH]_6)\}^{17-}$ can be represented as a wheel-like uranyl phosphate cluster unit of $(Na@[UO_2]_6[PO_3OH]_6)^+$ sandwiched by two trilacunary $[\alpha\text{-B-}SbW_9O_{33}]^{9-}$ units.

In 2021, Zhang et al. reported a mixed-valent uranium(V/VI) cluster $[H_3O^+](U^V[U^{VI}O_2]_8[\mu_3{-}O]_6{-}[PhCOO]_2[Py(CH_2O)_2]_4[DMF]_4)$ (Ph = phenyl, Py = pyridyl, DMF = N,N-dimethylformamide), synthesized by solvothermal reaction of $UO_2(NO_3)_2{\cdot}6H_2O$, macrocyclic oligoboronate, and benzoic acid in a mixed solvent of DMF, methanol, and ethanol at 120 °C [33]. This compound crystallizes in the monoclinic space group of $P2_1/c$. The central U^V resides in the center of the cluster and is surrounded by eight uranyl(VI) units. This well-assembled architectural feature nicely stabilizes pentavalent uranium. The U(V) center is a tetragonal bipyramid geometry coordinated by four $\mu_3{-}O$ atoms and two oxygen atoms from DMF molecules.

In 2021, Lu et al. reported a series of organic aromatic carboxylic ligand-modified hexanuclear thorium clusters synthesized by solvothermal reactions and studied their radiation chromic behaviors or photoluminescence quenching responses toward X-rays, β-rays, and γ-rays. The structures comprise a typical $[Th_6O_8]$ unit, which is chelated by monotopic carboxylic ligands [34, 35].

2.1.2 Actinide metal-organic framework (An-MOFs)

Metal-organic frameworks materials have attracted numerous attentions due to their fascinating structural diversity and multiple applications [36]. An-MOFs have been developed rapidly over the last two decades and have shown unique coordination geometries over other main groups and transition metal elements in the family [37, 38]. From 2003 to 2010, only a few examples of actinide MOFs were reported in China [39–42]. After 2010, many researchers in China showed great enthusiasm for scientific research in An-MOFs and devoted efforts to this booming area. This section stresses the synthesis and structure of An-MOFs; the applications will be discussed in another section.

2.1.2.1 Thorium based metal-organic frameworks (Th-MOFs)

All the thorium metal nudes occur in the 4+ oxidation state in Th-MOFs. The strong Lewis acidity of Th^{4+} has a high tendency to coordinate with carboxylate ligands. The combination of organic ligands and spherical coordinated thorium centers gives rise to a wide diversity of MOF structures. To simplify the structure description, several second building units (SBU) can be concluded according to different nuclearities from mono- to hexanuclear motifs.

Mononuclear and binuclear motifs are rarely observed in Th-MOFs. One example is $Th(TCPB)(C_3H_7NO)_3(H_2O)_2$ (H_4TCPB = 1,2,4,5-tetrakis[4-carboxyphenyl] benzene) reported by Yu et al. [43]. Each thorium atom is coordinated to eight O atoms from six TCPB ligands. The mononuclear Th motifs are chelated and bridged by the TCPB ligands, forming a microporous three-dimensional framework. With the adjustment of the reaction conditions, two other Th-TCPB MOFs based on binuclear motifs were obtained. Such observations of nuclearity transformation are not very common in Th-containing materials. Li et al. reported two special Th-MOFs with graphene-like (6,3) sheet topologies [44]. In this research, compound 1, $[C_7H_{11}N_2]_5(Th_2[L_1]_2Cl_6){\cdot}Cl$, is based on binuclear motifs, while compound 2, $([CH_3]_2NH_2)(Th_2[L_2]_3[H_2O]_2){\cdot}8H_2O{\cdot}6DMF$, is based on mononuclear motifs (H_3L_1 = 1,3,5-tri(4′-carboxylphenyl) benzoic acid; H_3L_2 = 4,4′,4′-nitrilotribenzoic acid). In compound 1, one Th^{4+} cation is bonded to three L_1 units and three other Cl^- anions. Two thorium atoms are connected by one Cl^- anion in a binuclear motif of compound 1. By replacing the rigid ligand H_3L_1 with a more flexible ligand H_3L_2, a three-dimensional framework compound 2 can be obtained. In this structure, one Th atom is coordinated with six L_2 units and one water molecule. Every thorium atom is chelated with other thorium atoms by three carboxylate groups from three isolated ligands. Although these two Th-MOFs have different SBUs and coordination geometries of thorium metal centers, a common character that can be observed is that these two kinds of Th metal centers both feature the coordination geometries of high-valent actinide metals, the hula-hoop, and the tetracapped trigonal prismatic coordination geometry, respectively. Another mononuclear motif observed in Th-MOFs is recognized as ten-coordinated with a bicapped square prism coordination environment Th^{4+} site [45]. Every two thorium mononuclear can serve as dimers by bridging with four carboxylate groups. Eight L ligands and six thorium dimers are connected to a molecular cage, further yielding a three-dimensional porous structure, named SCU-11. The most interesting thing is that the closed Th metal sites of SCU-11 can be switched to open Th metal sites after degassing at 100 °C for 8 h. With the terminal water molecules of Th^{4+} lost, a ten-coordinated bicapped tetragonal prism becomes an eight-coordinated tetragonal prism. Open metal sites are mostly dominated by divalent transition metals and trivalent RE elements, and only a few are tetravalent metal sites. The abilities of porous Th-MOF SCU-11-A with open metal sites further extended gas adsorption and separation.

Trinuclear SBUs are far more uncommon in Th-MOFs. Li et al. reported a mesoporous cationic thorium-organic framework (SCU-8) with cationic $(Th_3[COO]_9O[H_2O]_{3.78})^+$ clusters [46]. The basic Th^{4+} features a ten-coordinate capped triangular cupola geometry. Each thorium atom is bonded with eight oxygen atoms from five carboxylate groups, one water molecule, and one μ_3–O group. The three thorium atoms are connected by one μ_3–O and six μ_2–O's from carboxylates. Furthermore, the trinuclear clusters and the linkers are connected into a mesoporous thorium-organic framework. The BET surface area is measured to be 1360 $m^2\,g^{-1}$ and the pore size is calculated to be 2.2 nm. In the adsorption experiments of anionic organic pollutants, including PFOS (perfluorooctane sulfonate), SCU-8 showed great sorption capacity and selectivity over PFOS.

The mix-ligand strategy used for synthesizing thorium-MOFs also helps to construct novel structures. The SBU $(Th_6[COO]_{20}[DMF]_4[H_2O]_2[\mu_3–O]_2)$ observed in Th-IHEP-5 consists of one tetranuclear Th_4 core and two bridged Th metal centers, in which Th_2 and Th_3 are nine coordinated while Th_1 is 10 coordinated [47]. In this structure, the $TCPP^{4-}$ ligands are connected to all three kinds of thorium atoms, and the H_2bpydc linkers are only coordinated with Th_2 atoms. The Th_6 clusters are extended into (Th_6) chains and further into a three-dimensional framework. The BET surface area is measured to be 260 $m^2\,g^{-1}$, and the pore size ranges from 6 to 18 Å.

The hexanuclear motifs dominate thorium coordination environments. More than half of the reported Th-MOFs could find analogs in Zr/Hf-MOFs [48–56]. In recent years, Li et al. has systematically studied the structural complexity of thorium polyoxo clusters built from multiple ligands, including formate, MeTPDC (2′-methyl-[1,1':4′,1"-terphenyl]-4,4"-dicarboxylic acid) and TCPBA (tris[40-carboxybiphenyl] amine) [57–59]. An observation of SC–SC (single crystal to single crystal) transformation under the immersion of different organic solvents was reported recently [59]. The hexanuclear motifs feature a $Th_6(\mu_3–OH)_8$ SBU, and each $Th_6(\mu_3–OH)_8$ cluster is further bridged with twelve $TCBPA^{3-}$ ligands. and the remaining coordination sites are offered by two $HCOO^-$ anions, three water molecules, and one DMF. After soaking the crystals of Th-SINAP-200 in methanol, ethanol, or other organic solvent for 5–20 min, the O site of DMF and water molecules will be replaced by the O atom from $TCBPA^{3-}$ ligands. The $Th_6(\mu_3–OH)_8$ cluster of the soaked Th-SINAP-200, named Th-SINAP-201, is coordinated with 12 ligands in two modes. Moreover, when Th-SINAP-200 is soaked in water installed in organic solvent for 30 min, the crystal phase will transform into another crystal phase, named Th-SINAP-202 (Figure 2). Two neighboring $Th_6(\mu_3–OH)_8$ clusters are bridged with O atoms from $TCBPA^{3-}$ ligands, resulting in a $(Th_{12}[\mu_3–OH]_{16})$ part. The terminal DMF and $HCOO^-$ anions are replaced with water molecules. Moreover, this kind of SC–SC transition material is further used for selective detection of ^{129}I with the lowest detection limit.

In addition, a rare case of thorium-based heterometallic MOFs is the first transition-metal-thorium heterometallic MOF introduced by Xu et al. [60]. Each Th_6 cluster is coordinated with 12 ligands, while every Ni atom is bonded to four ligands. Every $(Ni[IN]_4)$ can be regarded as a four-connected linker, further connected with the Th_6 cluster into a cubic $Th_{48}Ni_6$ cubic cage with a diameter of 11.08 Å. In addition, the final structure shows a *ftw*-type topology. DFT studies, natural bond orbital (NBO) and electron localization function (ELF) approaches indicated that the excellent stability of this complex comes from the electronic and covalent interactions between cations and ligands, confirmed to be a cationic framework with free OH^- anions.

2.1.2.2 Uranium based metal-organic frameworks (U-MOFs)

The three classic coordination geometries of uranyl cations, UO_2^{2+}, tetragonal pyramids, pentagonal bipyramid, and hexagonal bipyramid, are incorporated into the

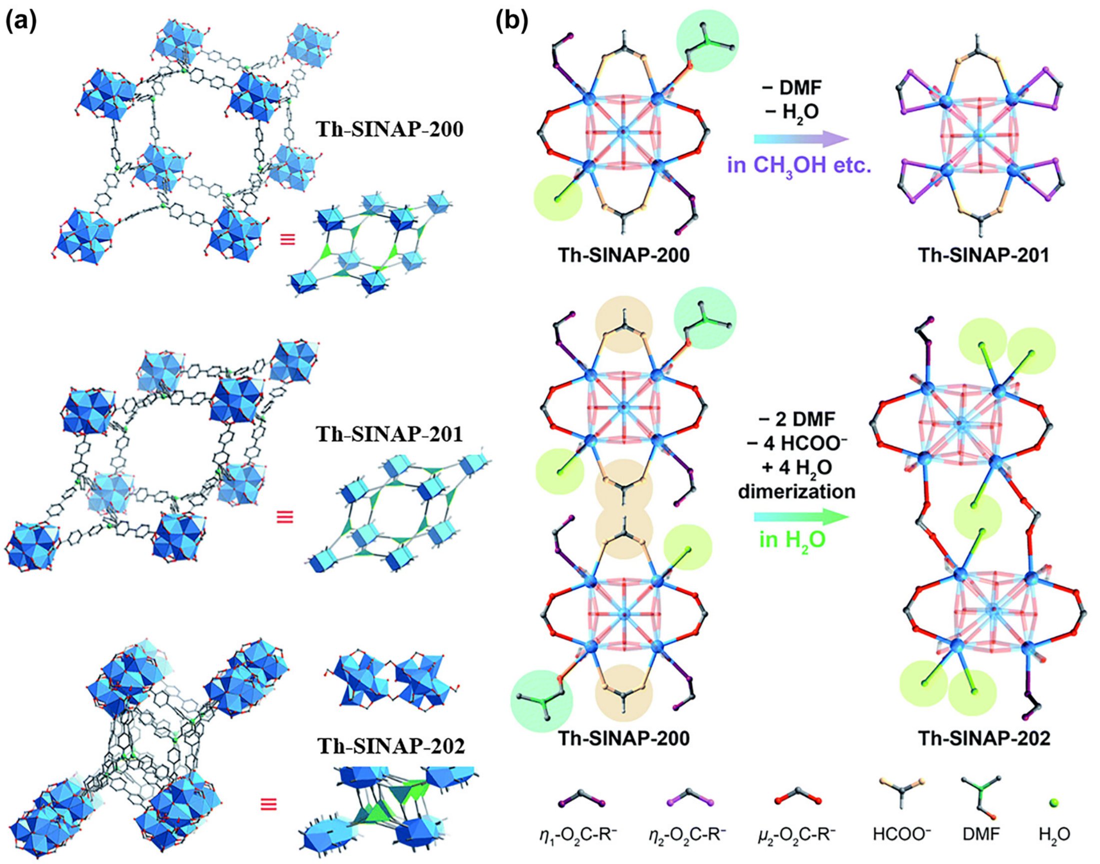

Figure 2: The 3D networks, simplified topologies (a) and the coordination geometry evolution of Th_6O_8 units (b) of Th-SINAP-200, Th-SINAP-201, and Th-SINAP-202. Reproduced with permission [59]. Copyright 2021, Royal Society of Chemistry.

infrastructure unit of the U-MOFs. Own to the strong bonding of U and O_{yl}, the coordinated atoms from ligands are forced to stay in the equatorial plane of U=O [61]. Therefore, most uranyl-organic coordination complexes are 1D chains or 2D layers [62]. A small number of them are three-dimensional frameworks. The structural complexity could be influenced by the flexibility and the length of the ligands.

Hu et al. resented a rare case of non-interpenetrated anionic U-MOF [63]. In this example, the uranyl cations served as tridentate linkers, while the $TCPE^{4-}$ ligands served as tetradentate linkers. Two different kinds of cavities can be observed in the structure. One is an adamantane-like octahedron with a cavity diameter of 15.55 Å, while another is a cuboctahedron with a cavity diameter of 31.10 Å. The properties of this compound with ultra large cavities were further explored. Dye sorption experiments indicated that the anionic FJI–H–U1 can selectively adsorb cationic dyes.

One of the classic topologies observed in U-MOFs is graphene-like (6,3) layers [64–66]. One special example is the polycatenation of three graphene-like uranyl organic networks reported by Wang et al. [67]. In this structure, not the flexibility of the ligand but the umbellate distortion of the uranyl coordination environment leads to the final polycatenation. The uranyl axis and the equatorial plane have U=O bond lengths of 1.728 and 1.805 Å, respectively (Figure 3a). The O=U–O bond angles are significantly smaller than 90°, and all six coordinated O atoms from the ligands bend in the same direction, forming a series of deformed graphene-like layers. Three sets of these (6,3) networks are interlocked by each other, exhibiting a rare case of a 2D to 3D polycatenated framework. In 2020, Cheng et al. reported another three-dimensional polycatenation, from 0 to 3D uranyl organic cages [68]. In this example, uranium centers served as tridentate linkers, while the *in situ* formed $([SC_6H_4COO]_2)^{2-}$ ligands served as bidentate linkers, further forming a rare case of octahedron-shaped adamantane (Figure 3b). Moreover, each cage is interlocked by six neighboring cages through mechanical bonding. The overall structure can be described as a unique uranium-organic framework. In addition, this kind of *in situ* synthesized flexible ligand is rarely used in constructing fantastic MOF structures. Most examples of polycatenations and interpenetrations in U-MOFs are based on multidentate ligands [69–71] and a few are based on hydrogen bonding [72].

One of the strategies to extend the dimensionality of uranium-bearing compounds is to introduce another metal center into the structure [64, 73, 74]. In 2003, Chen et al. reported a uranium-zinc-organic framework and studied the photoelectronic effect of this compound [39]. In 2005, Chen reported another two metal-organic coordination polymer (Ag[bipy]$[UO_2]$[BDC]1.5) (bipy = 2,2′-bipyridyl, BDC = 1,4-benzene- dicarboxylate) [40]. The photocatalytic activity of U-MOFs was first explored. Yang et al. also reported several U-Zn MOFs and their structures and properties [75].

Several researchers have also studied the influence of hydrolysis and ligand variation during the synthesis process of U-MOFs [75–81]. The first cationic uranyl-organic framework, SCU-7, was prepared using a hydrolysis control strategy [76]. SCU-6 was synthesized under solvothermal conditions. The structure analysis reveals that SCU-6 adapts a neutral two-dimensional layered structure. Four uranium metal centers are connected by two μ_3–O atoms and four μ_2–O atoms, forming a U_4 tetranuclear cluster. Each SBU is bonded to six organic linkers, while each ligand links three clusters, further constructing the whole structure. Compared to SCU-6, SCU-7 is obtained by reducing the extent of hydrolysis during the synthesis process. The SBU of SCU-7 turns out to be dinuclear U_2 clusters, and the uranium centers adapt to the pentagonal bipyramid geometry. Notably, all of the carboxylic acids are deprotonated in SCU-7. SCU-7 is confirmed to be a cationic 2D layered network after simple calculation. Anion-exchange experiments were carried out and showed the adsorption capacity and fast dynamics of anionic pollutants such as TcO_4^- (ReO_4^-) of SCU-7. The proton-conducting behaviors of SCU-7 were further studied. In addition to using carboxylates as linkers, phosphonates are also used in constructing fascinating U-MOFs [82].

2.1.2.3 Transuranium-based metal-organic frameworks

Only two examples of transuranium-based MOFs have been reported. In 2018, Mei et al. reported a neptunium(V)-mediated interwoven network, denoted as NRCP-1 [83]. To date, it is still the only transuranium-rotaxane complex. The NRCP-1 crystals were obtained under hydrothermal reaction of the Np(V) aqueous solution with [C6BPCEt@CB6]Br_2 (L–OEt–Br_2). The Np(V) center adapts an eight-coordinated geometry. Each neptunyl is connected to one O atom from the CB6 carbonyl group, four O atoms from two different L carboxylate groups, and one water molecule. The further formed [c2]Daisy chains are connected into a woven neptunium-rotaxane layered network. Interestingly, the uranium analog cannot be obtained under the same synthesis conditions. DFT calculations indicated that the calculated distances of the Np–O bond are close to the single crystal data. The spin density value of neptunium is calculated to be 2.21, indicating the oxidation state of 5+. This result agrees with the single crystal X-ray diffraction and UV–vis-NIR data with a main transition at 980 nm. In addition, a detailed analysis of the contributions of the atomic orbitals of O and Np atoms shows that the 5*f* orbitals of neptunium atoms contribute approximately 22.15–40.16% to all Np–O bonds.

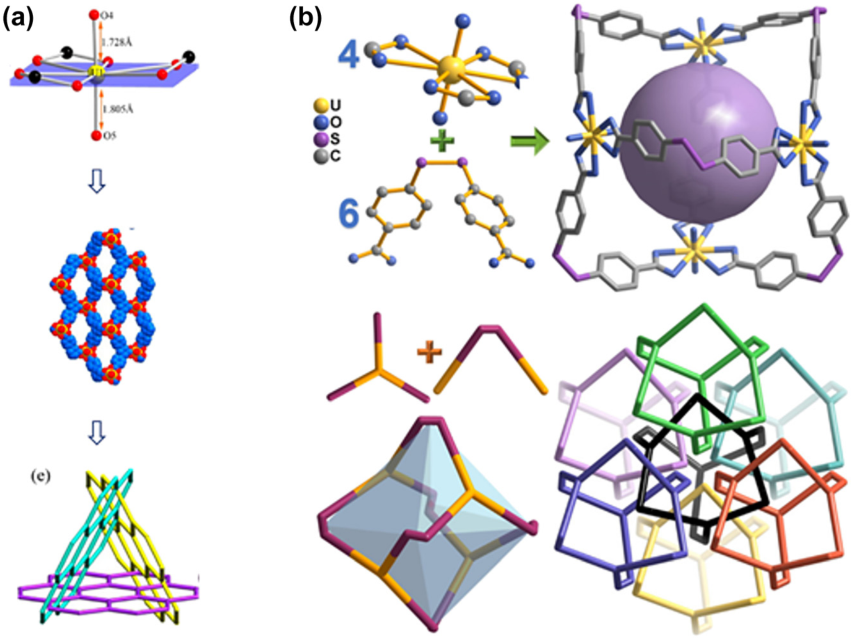

Figure 3: (a) The umbellate distorted uranyl cations are connected into 2D layers, which further result in a three-dimensional polycatenation. Reproduced with permission [67]. Copyright © 2015, American Chemical Society; (b) Illustration of the crystal structure of SCU-14. Reproduced with permission [68]. Copyright © 2020, American Chemical Society.

Another transuranium-based MOF is an Am MOF structure reported by Zhang et al. [84]. AmTPO crystallizes in the monoclinic space group, *P*-1. The asymmetric unit consists of one unique Am^{3+}, one crystallographic TPO^{3-} and one coordinated water molecule. The americium center forms an ellipsoidal polyhedron with nine coordinated oxygen atoms, in which eight oxygen atoms come from carboxyl groups and one oxygen atom comes from the coordinated water molecule. Adjacent Am^{3+} forms a pseudodimer building unit by coordinating with oxygen atoms originating from the TPO molecule. These dimer building units are then linked by the TPO ligands, forming an infinite layer along the [100] plane. Adjacent layers are connected via TPO molecules, forming a three-dimensional structure. Solid-state UV–vis-NIR spectroscopy of AmTPO showed prominent peaks at 507 nm originating from the electron transition from $^7F_0$ to $^5L_6$ and a peak at approximately 817 nm corresponding to the electronic transition from $^7F_0$ to $^7F_6$ (Figure 4).

2.1.3 Simple transuranic organic coordination complexes

In recent years, in addition to uranium and thorium compounds, Chinese researchers have also begun to investigate simple transuranic organic coordination complexes. Owing to the high radiotoxicity of transuranic elements and their unique position in the actinide series, there is a relatively blank gap in coordination chemistry studies. In the last two years, Wang and Li et al. from Soochow University isolated and characterized trivalent and pentavalent plutonium compounds in unusual oxidation states using the hole effect of crown ether [85, 86]. The stability and crystallization of pentavalent plutonium (Pu [V]) is a challenge due to its highly reactive and dynamic surface redox behavior and/or the disproportionation tendency of Pu(V) states. The fact that there are only five Pu(V) reported in the Cambridge database also demonstrates the difficulty of Pu(V) compound synthesis. The key

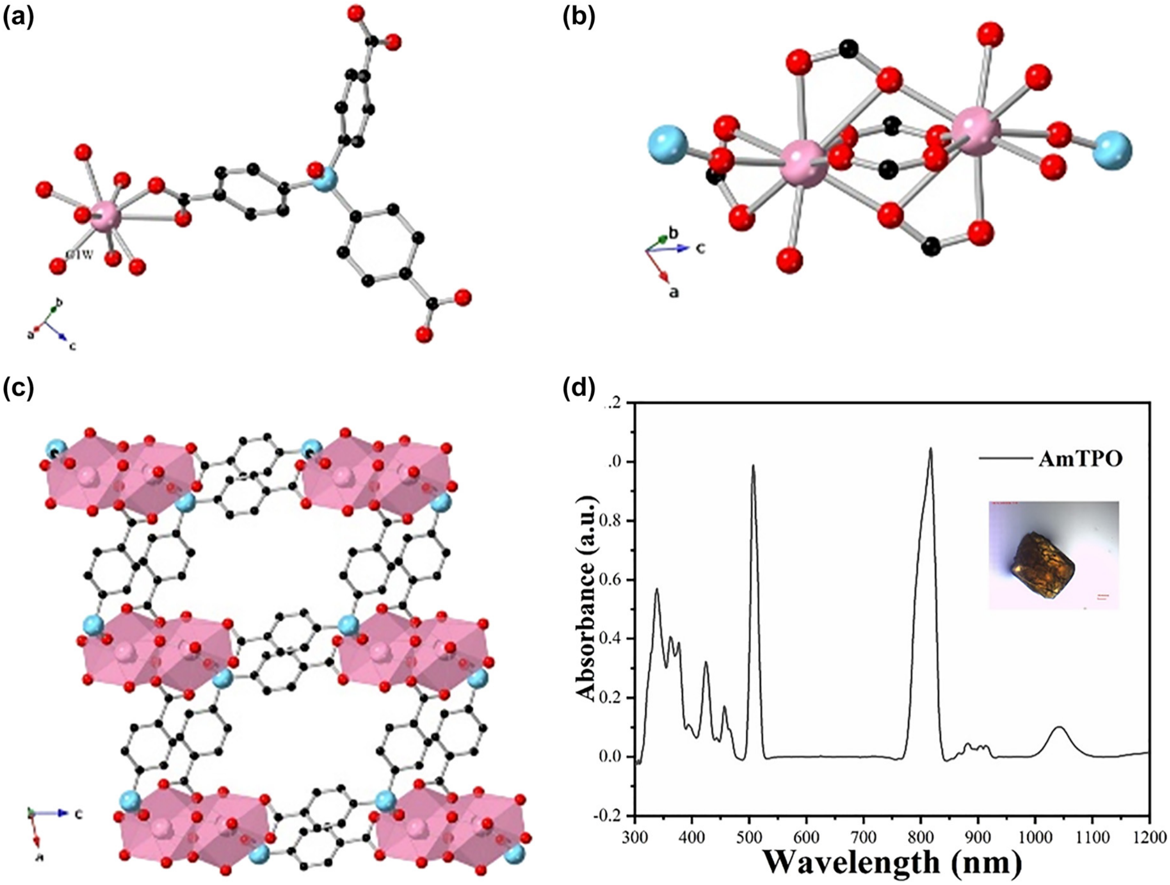

Figure 4: (a) The asymmetric unit of AmTPO. (b) Every two americium center are connected into a dimer building unit. (c) The three-dimensional network of AmTPO. (d) The UV–vis-NIR spectrum of AmTPO. Reproduced with permission [84]. Copyright 2022, Wiley-VCH.

problem associated with isolated Pu(V) complexes is to prevent Pu(V) from disproportionation or further reduction to Pu(IV) during reduction. Crown ethers are members of the cryptand-derived ligand family, with adjustable cavity sizes and multidentate oxygen donors, and exhibit selective coordination of actinide ions through the formation of inclusion complexes. Based on this, Wang et al. proposed a route to synthesize the Pu crown ether inclusion complex (Pu^VO_2[18-crown-6]ClO_4) in aqueous solution with unstable oxidation state [85]. The crystal structure was comprehensively characterized, and single-crystal X-ray diffraction results showed that Pu^VO_2[18-crown-6]ClO_4 crystallized in tetragonal space group $I4_1/a$. In the crystal structure, Pu atoms are found in a strictly linear PuO_2^+ dioxo unit completely encapsulated in disordered crown ether ligands (Figure 5a). In crown ethers, the C–O–C–C units are in the trans conformation, while the O–C–C–O units are the gauche conformation. The six oxygen atoms in the crown ether are equatorial coordinators with PuO_2^+, forming a distorted hexagonal bipyramidal coordination geometry. The axial bond length of the plutonium ion is 1.784(6) × 2 Å, and the equatorial Pu–O distances are 2.574(9)–2.574(9) Å. The steric effect and cavity effect from the 18-Crow-6 ligand resulted in a slight change in the bond distances of Pu^VO_2[18-crown-6]ClO_4 compared with the bond distance of the Pu(V) compound previously reported. The axial bond length is slightly shorter than that of Pu(V) compounds, ranging from 1.78 to 1.82 Å. Consequently, the equatorial bond distance is longer than the reported value (2.43–2.49 Å) [87–89]. It is noteworthy that the axial bond length of Pu^VO_2[18-crown-6]ClO_4 is significantly longer than that of hexavalent plutonyl compounds, where Pu=O ranges from 1.72 to 1.75 Å [90, 91]. Crystallographic results show that actinide contraction dominates the An=O axial bond distance and the An–O equatorial bond distance in Np and Pu isotopes. In the An^VO_2[18-crown-6]ClO_4 (An=Np, Pu) series, these experimental values transited axial: from 1.80 to 1.773(8) Å and equatorial: from 2.602–2.576 to 2.574(9)–2.574(9) Å, respectively [92]. In addition, experimental spectral data of solid Pu(V) complexes with rich electronic transition information were provided for the first time in that paper. Relativistic density functional theory (DFT) calculations confirm that the ground-state electron configuration of Pu(V) is f^3 ([core]$5f_\delta^2 5f_\Phi^1$), and further prove that a combination of cavity and steric repulsion effects contributes to the stability of Pu(V) species in the 18-crown-6 ligand (Figure 5b). This work provides a novel synthesis route combining selective redox/selective

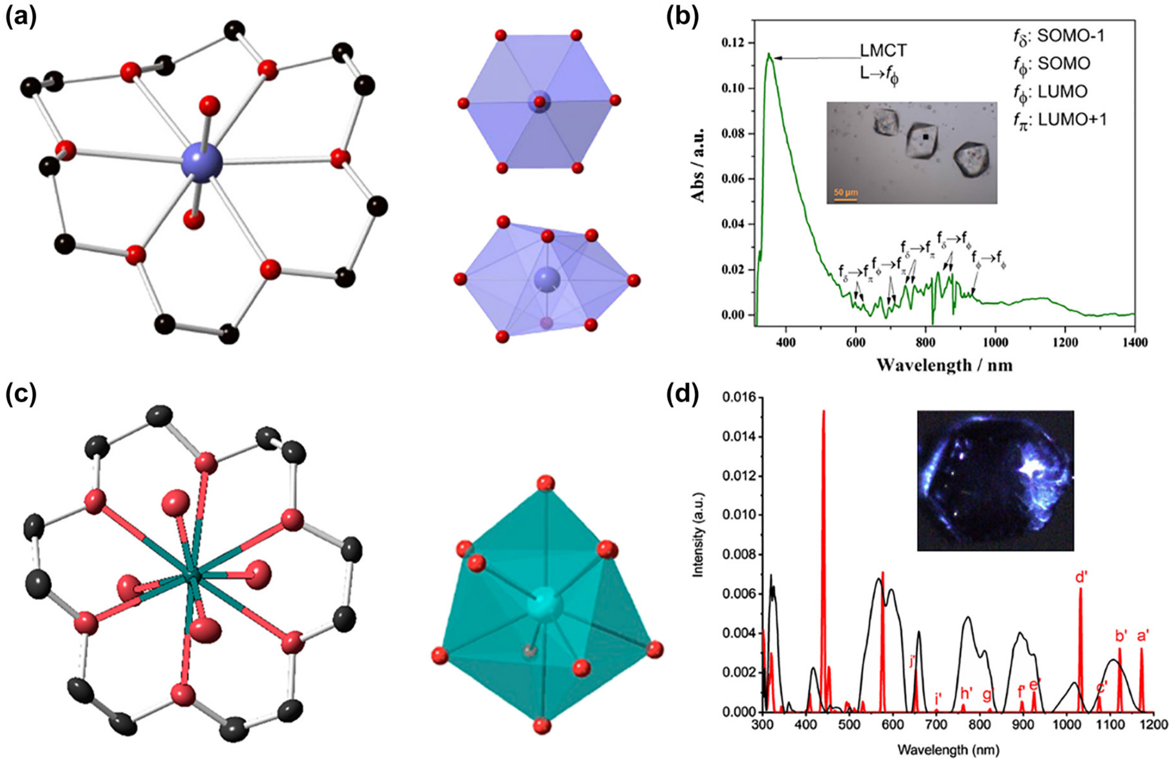

Figure 5: (a) Encapsulation of PuO_2^+ within the cavity of 18-crown-6; (b) Solid-state UV–vis-NIR absorption spectrum for Pu^VO_2[18-crown-6]ClO_4. Inset: the picture of PuO_2[18-crown-6]ClO_4 crystals. Reproduced with permission [85]. Copyright 2020, Chinese Chemical Society. (c) Encapsulation of Pu^{III} within the cavity of 18-crown-6. (d) Solid-state UV–vis-NIR absorption spectrum for Pu(III)–18C6. Inset: the picture of Pu(III)–18C6 crystals. Reproduced with permission [86]. Copyright 2021, American Chemical Society.

coordination/crystallization, promising for the synthesis of atypical valence actinide compounds. Similarly, Li et al. produced a trivalent plutonium crown ether inclusion complex $([H_3O][18\text{-crown-}6])(Pu[H_2O]_4[18\text{-crown-}6])(ClO_4)_4\cdot 2(H_2O)$ (donated as Pu^{III}–18C6) by reacting crown ether ligands with trivalent plutonium, which was reduced by HBr [86]. Single crystal X-ray diffraction reveals that Pu^{III}–18C6 crystallized in the orthorhombic space group of *Pccn*, which is composed of $(Pu[H_2O]_4[18\text{-crown-}6])^{3+}$, $([H_3O][18\text{-crown-}6])^{+}$ and perchlorate anion. The plutonium atoms are completely encapsulated in the 18-crown-6 cavity, creating a distorted bicapped square antiprism geometry (Figure 5c). The electronic structure reveals that the ground-state electronic structure is $f_\delta^2 f_\pi^1 f_\sigma^1 f_\varphi^1$. Theoretical evaluation confirmed the existence of a weak Pu–O coordination bond between 18-crown-6 and Pu(III) ions (Figure 5d).

2.2 Actinide organometallic compounds

Organometallic chemistry has been and still is one of the most important fundamental subjects in chemistry. Organometallic chemistry with transition metals has revolutionized organic synthesis during the last five decades and has numerous applications in synthetic chemistry and materials science, culminating in the award of the Nobel Prize in Chemistry three times (2001, 2005, and 2010) in the 21st century. In sharp contrast, the organometallic chemistry of actinides is less developed, and the applications of actinide organometallic complexes are limited. In the last 10 years, many researchers in China have performed extensive work in this area.

2.2.1 Synthesis, characterization and reactivity

2.2.1.1 Complexes with actinide metallacycles

The first example of stable actinide metallacyclopropene complex **2** was reported by Fang et al. in 2014 and was synthesized by the reduction of complex **1** with potassium graphite (KC_8) in the presence of diphenylacetylene (Scheme 1) [93]. DFT calculations show that the two Th–C σ–bonds are very polarized and that the 5*f* orbitals of Th contribute to this bonding interaction. Therefore, the Th–C bond in complex **2** exhibits nucleophilicity, and thus, heterounsaturated organic molecules such as benzaldehyde could insert into the Th–C bond to form complex **3**. No reaction between complex **2** and alkyne was observed. However, the PhCCPh unit was replaced when Ph_2CO was used as a substrate, leading to the formation of a thorium pinacolate complex **4**.

Thorium metallacyclopropene **2** was thermally stable. However, when the substituent of the alkyne was changed from phenyl to alkyl, the corresponding thorium metallacyclopropenes **5a** and **5b** with phenyl(alkyl)acetylenes were thermally unstable and could not be isolated [94]. Only intramolecular C–H bond activation products **6a** and **6b** were isolated (Scheme 1).

The first actinide metallacumulene was reported by Fang et al. in 2015 [95]. By the reduction of a mixture of complex **7** and 1,4-diphenylbutadiyne with KC_8, thorium

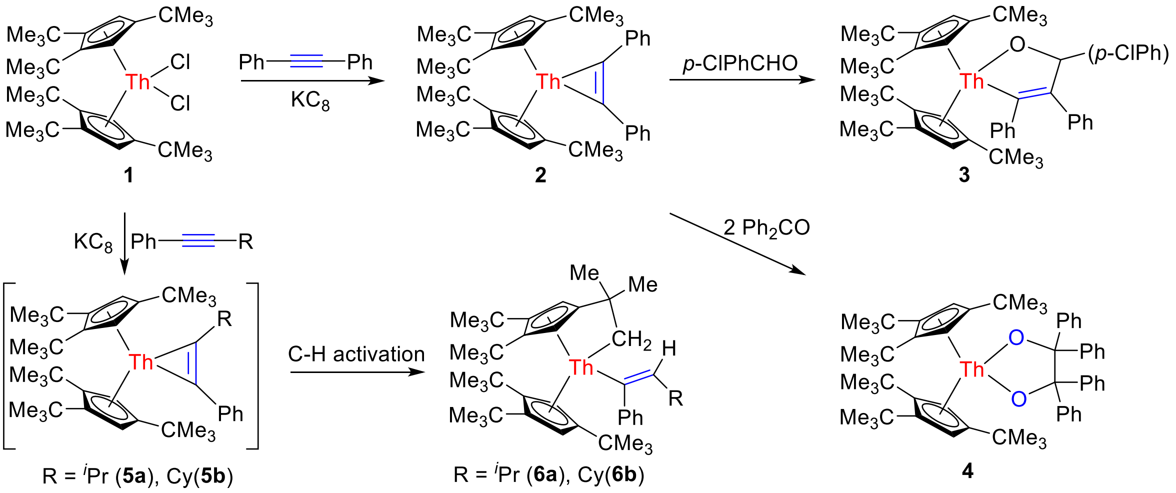

Scheme 1: Synthesis and reactivity of thorium metallacyclopropenes. Reproduced with permission [93]. Copyright 2014, American Chemical Society.

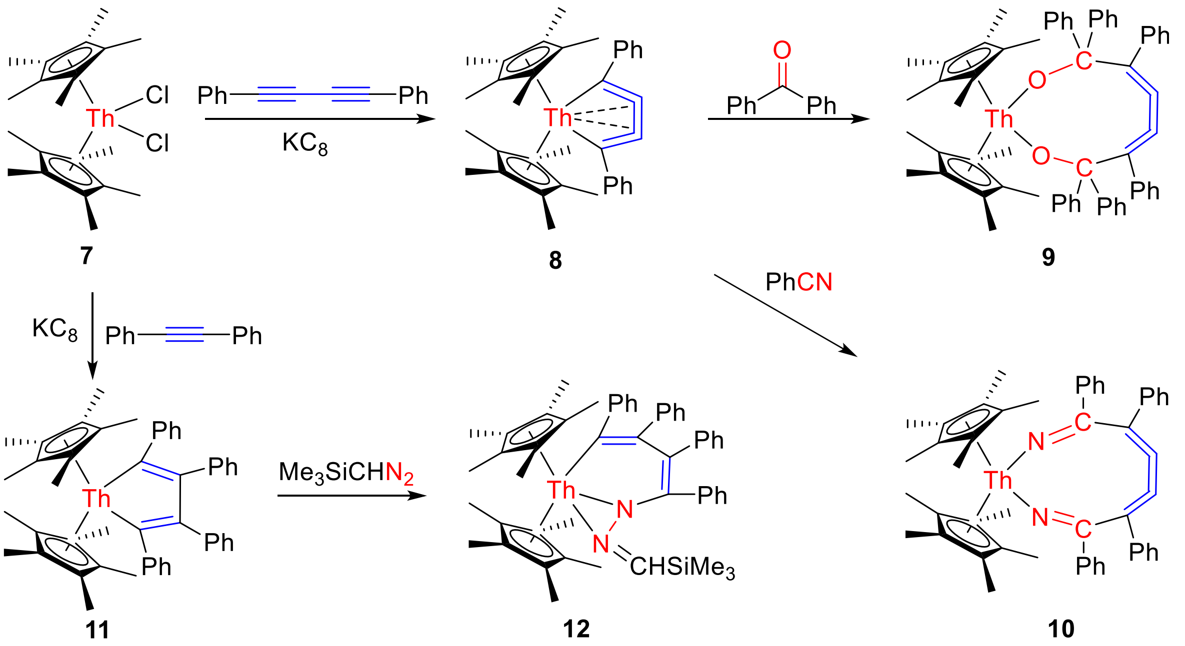

Scheme 2: Synthesis and reactivity of thorium metallacumulene and metallacyclopentadiene. Reproduced with permission [96]. Copyright 2015, Royal Society of Chemistry.

complex **8** with a metallacyclopentatriene unit was isolated and fully characterized (Scheme 2). DFT calculations show that the 5*f* orbitals have a notable contribution to the polarized Th–C bond in this species, which could react as a nucleophile toward a variety of hetero-unsaturated molecules to form nine-membered species **9** and **10** (Scheme 2).

In the same year, Fang et al. reported the first example of thorium metallacyclopentadiene **11**, which was synthesized by the reduction of complex **7** with KC_8 in the presence of diphenylacetylene (Scheme 2) [96]. Similar to thorium metallacyclopropene **2**, DFT analysis shows that the Th–C σ–bonds in **11** were also very polarized. Therefore, the insertion of unsaturated organic substrates into the Th–C bond was favorable. For instance, six-membered hydrazido was formed by the reactions of **12** with Me_3SiCHN_2 (Scheme 2).

Subsequently, a series of thorium metallacyclopen tadienes and metallacyclopropenes were synthesized by similar procedures in Fang et al. [97]. They found that the steric and electronic properties of the alkynes have important influences on the products (Scheme 3). For instance, C_s symmetric thorium metallacyclopentadienes **15** were formed when internal phenyl(alkyl)acetylenes (PhCCR) were used, while C_{2v}-symmetric metallacyclopentadiene **14** was formed when phenyl(silyl)acetylene ($PhCCSiHMe_2$) was used, whereas sterically more encumbered $PhCCSiMe_3$ gives chlorometalacyclopropene complex **16**.

Interestingly, when complex **7** was reduced with KC_8 in the presence of 2,2′-bipyridine (bipy), bipy-stabilized thorium metallocene **17** was isolated (Scheme 3) [98]. Other bipy-stabilized thorium metallocene complexes could also be synthesized by the same method. These complexes can be used as a source of Th(II) synthon, which can react with conjugated alkynes, carbodiimide, isothiocyanate, organic azides, and so on [99–101].

After great success in the synthesis of thorium metallacycles, Zhang et al. tried to synthesize uranium metallacycles via a similar strategy. Thus, the first stable uranium metallacyclopropene **19** was also synthesized by the reduction of complex **18** with KC_8 in the presence of bis(trimethylsilyl)acetylene (Scheme 4) [102]. DFT analysis reveals that the 5*f* orbitals of the uranium center contribute largely to the σ– and π–bonds of the U–(η^2–C=C) moiety; thus, the U–C bonds are more covalent than those of the Th–C bonds in complex **2**. Therefore, the reactivity pattern of this uranium metallacyclopropene was also different from that of the above thorium metallacyclopropene [103, 104]. For example, the coordinated alkyne moiety in uranium metallacyclopropene was readily replaced during the reactions of complex **19** with unsaturated organic molecules such as alkynes and imines (Scheme 4).

Uranium metallacyclocumulene was also reported by Zhang et al. *via* a similar strategy [105, 106]. As shown in Scheme 5, by the reduction of complex **18** with KC_8 in the presence of $Me_3SiC{\equiv}C{-}C{\equiv}CSiMe_3$, uranium metallacyclo

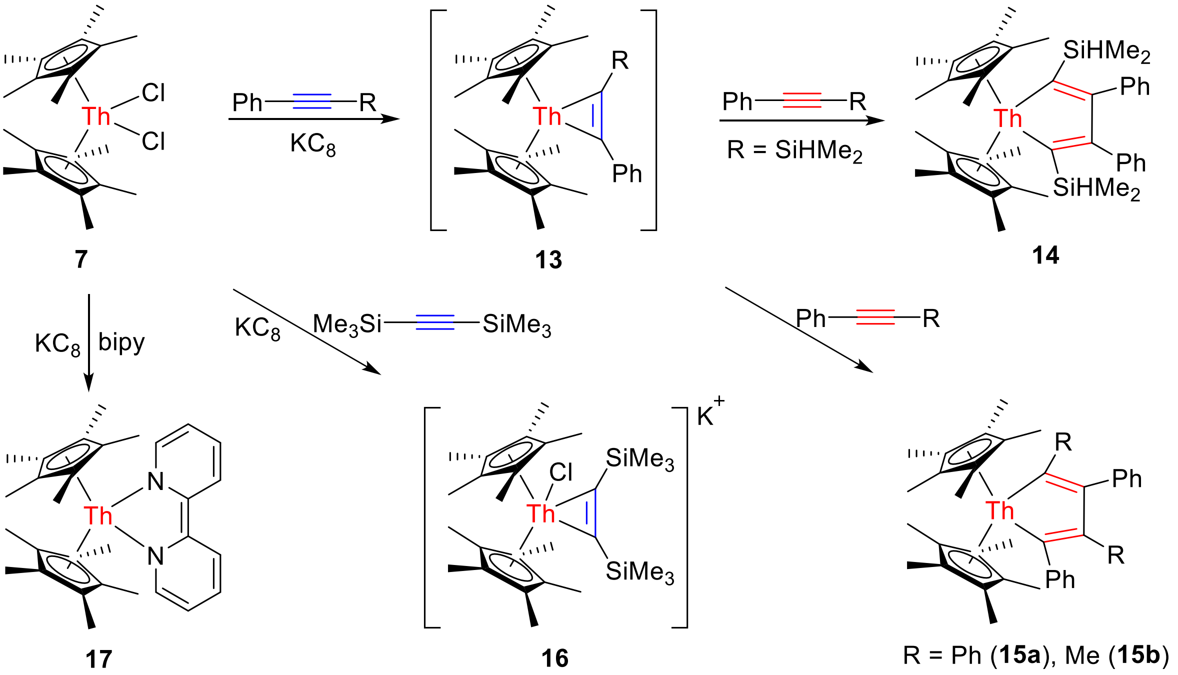

Scheme 3: Synthesis of thorium metallacyclopentadiene. Reproduced with permission [98]. Copyright 2016, American Chemical Society.

cumulene **24** was formed in good yield. DFT calculations show that the 5*f* orbital of uranium has a substantial contribution to the bonding of the U–C bond in the metallacyclopentatriene U(η^4–C=C=C=C) moiety, and thus, the U–C bond in **24** was more covalent than the Th–C bond in analogous complex **8**. Therefore, the reactivity patterns of uranium species **24** were also different from those observed for complex **8**. For instance, complex **24** can be viewed as a U(II) synthon when it reacts with butadiyne and diazabutadiene. However, uranium and thorium metallacyclopentatrienes can also show similar reactivity models, e.g. both of them could react with ketones to form nine-membered heterometallacycles (Scheme 5).

By the reduction of complex **18** with KC$_8$ in the presence of bipy, the corresponding uranium bipyridyl metallocene **28** was formed (Scheme 5) [107]. Although this

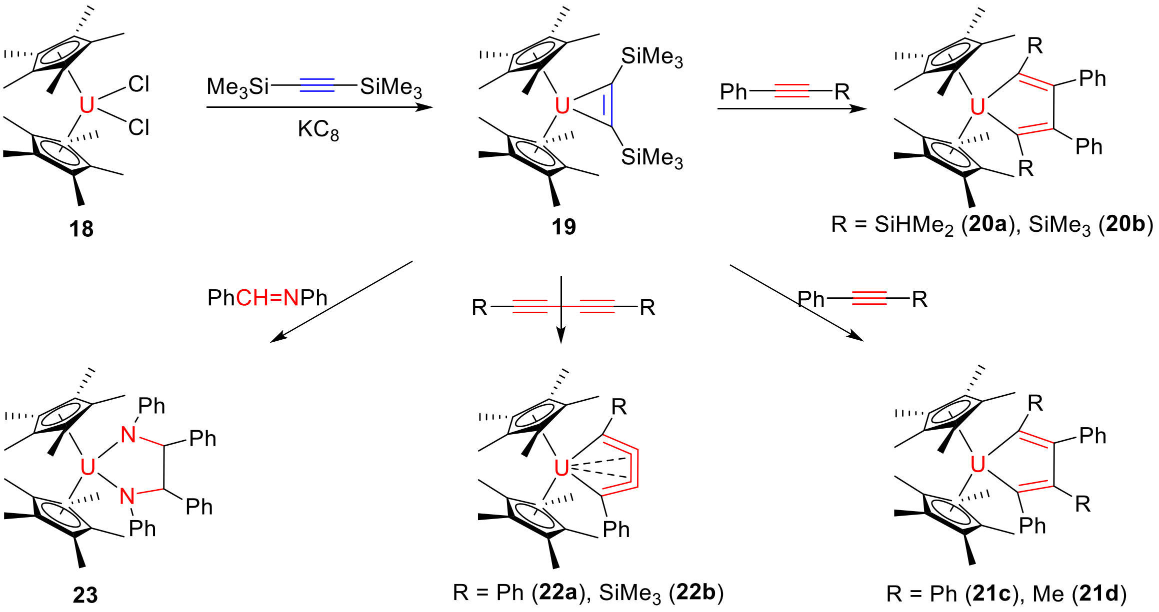

Scheme 4: Synthesis and reactivity of uranium metallacyclopropenes. Reproduced with permission [102]. Copyright 2016, American Chemical Society.

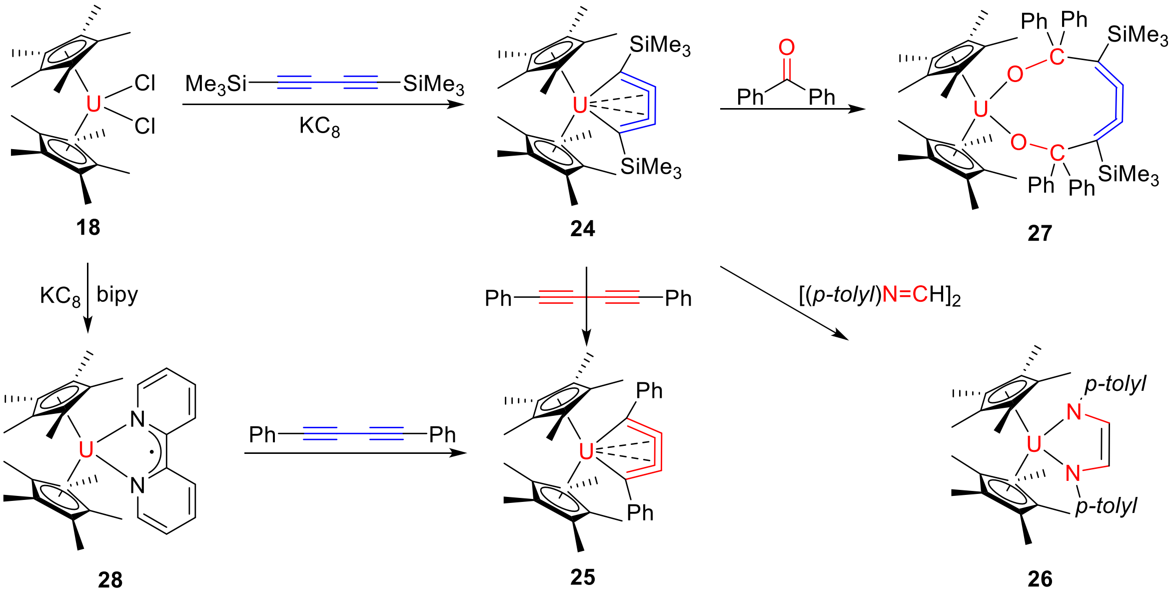

Scheme 5: Synthesis and reactivity of uranium metallacumulene. Reproduced with permission [106]. Copyright 2017, Royal Society of Chemistry.

complex has an analogous framework with Th species **17**, the electronic ground states are different. It is a bipy dianion coordinate to the Th(IV) center in **17**, whereas it is a bipyridyl radical anion coordinate to a U(III) atom in **28**. Therefore, when complex **28** reacts with unsaturated molecules, the two electrons are derived from the bipyridyl radical anion and the U(III) center. However, these electrons are provided by the dianionic ligand of Th in the case of complex **17**.

In 2020, Yu et al. reported a series of inverse-sandwich arene-bridged dithorium complexes **31** – **34** by the reduction of Th(IV) precursor **30** with KC_8 in the presence of different arenes (Scheme 6) [108]. The bridged arenes could be benzene, toluene, biphenyl, and naphthalene in this system. Spectroscopic data and structural analysis consistent with assignment of an arene tetraanion and two Th(IV) centers. DFT calculations revealed a δ bonding interaction between the arene π^* orbitals and the thorium $6d$ and $5f$ orbitals, which was similar to the bonding interaction observed in relevant uranium and rare-earth metal species [109, 110]. Further reactivity studies showed that inverse-sandwich dithorium complexes can be used as a low valent thorium synthon toward a series of organic molecules.

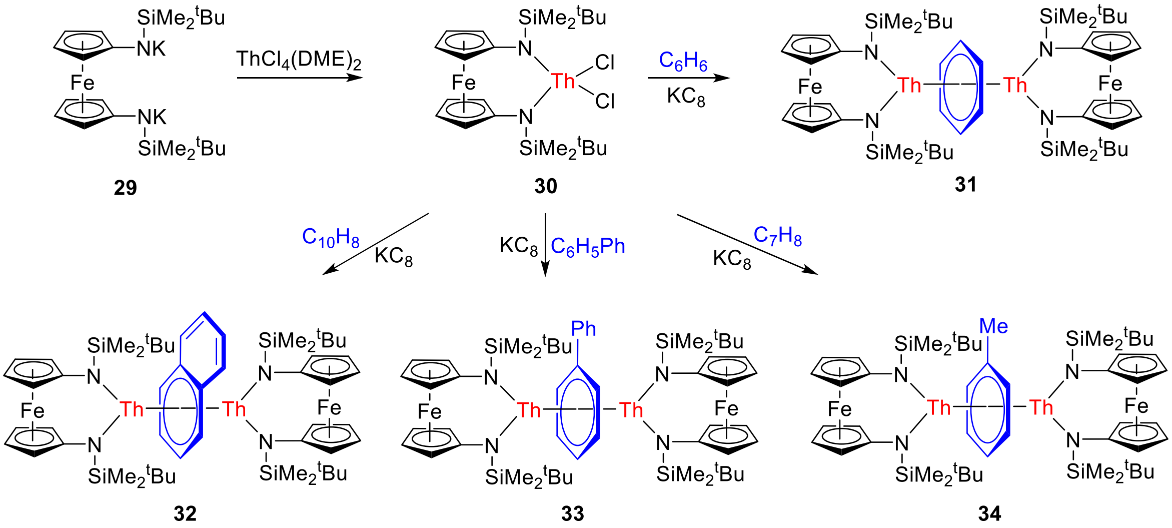

Scheme 6: Synthesis of arene-bridged dithorium complexes. Reproduced with permission [108]. Copyright 2020, American Chemical Society.

2.2.1.2 Complexes with An–C double bond

In 2011, Ren et al. reported the first example of thorium polycarbene complex **36** in good yield by the salt metathesis reaction of ([$Ph_2P{=}S]_2C)Li_2$ with $ThCl_4(DME)_2$ (Scheme 7a) [111]. DFT calculations suggest that the two Th=C double bonds were significantly polarized toward the carbene carbon atom and thus exhibited nucleophilic behavior when it reacted with Ph_2CO.

In 2018, Su et al. reported the first example of a double dative bond between uranium and carbon by the reactions

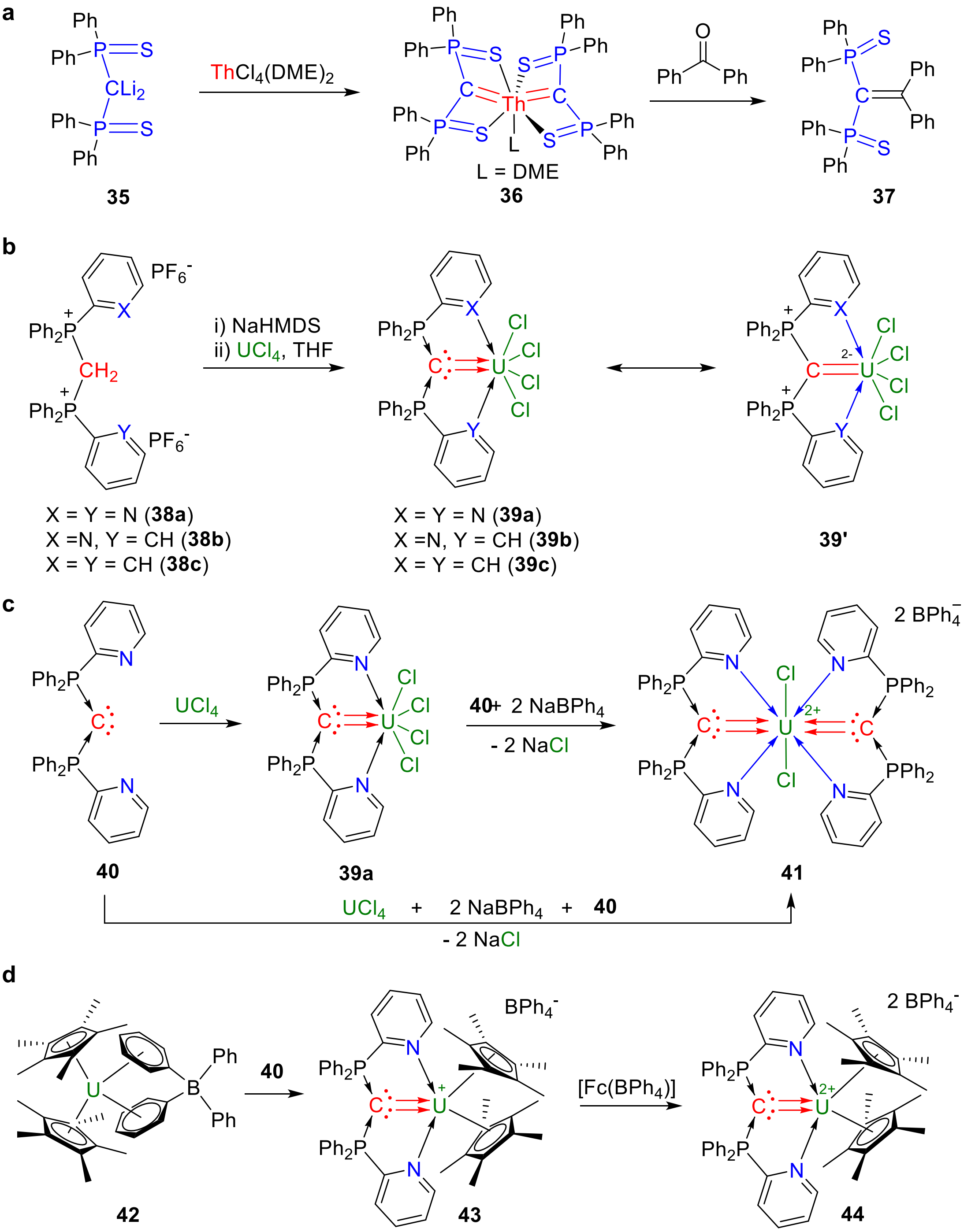

Scheme 7: Synthesis of complexes with An=C double bond. **a**. Reproduced with permission [111]. Copyright 2011, Royal Society of Chemistry. **b**. Reproduced with permission [112]. Copyright 2018, Nature Publishing Group. **c**. Reproduced with permission [114]. Copyright 2021, Chinese Chemical Society. **d**. Reproduced with permission [115]. Copyright 2021, Wiley-VCH.

of UCl_4 with a series of carbodiphosphoranes (CDPs) [112]. CDP–UCl_4 adducts **39** were synthesized by the reactions of UCl_4 with CDPs, which were formed by the deprotonation of corresponding tridentate, bidentate or monodentate CDP precursors **38** with NaHMDS (Scheme 7b). The U–C double bonds in these complexes are in the range of 2.411(3)–2.471(7) Å, which are shorter than the U–C bond lengths found in U–NHC addcuts (2.573–2.788 Å). DFT calculations show that both the σ and π bonds in these complexes are strongly polarized toward the carbon end, and thus, the nature of the U=C bond is a double dative bond from carbone to uranium. The predicted bond dissociation energy for monodentate CDP–UCl4 adduct **39c** is 70.8 kcal mol^{-1}, suggesting that the unsupported $U \leftleftarrows C$ double dative bond is rather strong. The dative bonding interaction between rare-earth metal and carbone was also observed in a CDP–CeBr3 adduct [113].

Further reaction of complex **39a** with two equivalents of $NaBPh_4$ and one equivalent of CDP ligand **40** results in the formation of complex **41**, which contains two double dative bonds with a $[C \rightrightarrows U \leftleftarrows C]$ core (Scheme 7c) [114]. This is the first example of a species with two carbone ligands coordinated with a single U center. The U=C bond length in **41** is 2.491(4) Å, which is slightly longer than the double dative U=C bond in **39a** (2.471(7) Å). The slightly longer distance was probably due to the congested coordination of the uranium center in complex **41**. Both the 5*f* and 6*d* orbitals/electrons of the uranium center remarkably contribute to the U=C double bonds, as revealed by theoretical analysis. Further DFT calculations show that the π–bond is significantly stronger than the σ–bond in this species.

Two CDP-supported uranocene complexes, $([Cp^{\star}]_2U[III][CDP])(BPh_4)$ (**43**) and $([Cp^{\star}]_2U[IV][CDP])(BPh_4)_2$ (**44**), were also reported by Su et al. in 2021 (Scheme 7d) [115]. Although the U(III)=C bond distance (2.666(3) Å) in complex **43** was significantly longer than the U(IV)=C bond length in complex **44**, quantum chemical calculations elucidated that the CDP ligand in both complexes served as both σ– and π–donors to the uranium center. Therefore, the U=C double bonds in **43** and **44** are also significantly polarized, as observed in complexes **39** and **41**.

2.2.1.3 Complexes with An–H bond

In 2011, Ren et al. reported the synthesis of thorium hydride complex **47** by the metathesis reaction of tris-Cp thorium chloride complex **46** with an excess of KH in good yield (Scheme 8a) [116]. Th–H complex **47** is an excellent catalyst for the polymerization of rac-lactide, leading to the formation of atactic polylactides with narrow molecular weight distributions and high molecular weights.

In 2019, Qin et al. reported an example of actinide dihydrido complex **49** with two super-bulky substituted Cp ligands (Scheme 8b), penta-arylcyclopentadienyl ($Cp^{Ar^{\star}}$) and pentamethylcyclopentadienyl ($Cp^{\star}$) [117]. Complex **49** was synthesized by the hydrogenolysis of complex **48** with pentamethylcyclopentadiene in THF under 10 atm H_2. A series of actinide metallacycles, including the first actinide metallacyclopentyne, were generated by the reactions of complex **49** with various unsaturated organic molecules. The super-bulky $Cp^{Ar^{\star}}$ and $Cp^{\star}$ ligands provide an essential coordination environment for the isolation of this monomeric actinide dihydrido species.

As a proof-of-concept, Chen et al. found that with less bulky alkyl-substituted Cp ligands, a series of actinide trihydrido clusters $([Cp^R]Th[\mu\text{–}H]_3)_n$ (n = 5, 6, 7, and 8) were formed [118]. For instance, by the hydrogenolysis of mono-Cp-ligated thorium tribenzyl complexes $([Cp^R]Th[p\text{–}CH_2\text{–}C_6H_4\text{–}Me]_3)$ with 10 or 40 atm H_2, thorium trihydrido clusters $([Cp^{Me4R}]ThH_3)_n$ (R=H, n = 8; R=Me, n = 7; R=$SiMe_3$, n = 6) were formed in good yield. The accurate hydride positions in $([Cp^{Me4}]ThH_3)_8$ were confirmed by single-crystal neutron diffraction. The nuclearity of the metal cluster increases with the less bulky cyclopentadienyl ligand $C_5H_4SiMe_3$ ($Cp^{\#}$); thus, a trideca-nuclear complex $([Cp^{\#}]_{12}Th_{13}H_{40})$ was formed by the hydrogenolysis of $(Cp^{\#})Th(p\text{–}CH_2\text{–}C_6H_4\text{–}Me)_3$.

2.2.1.4 Complexes with An–L bonds

In 2011, Ren et al. reported an example of base-free terminal imido thorium complex **57**, which could be used as an effective precursor for the synthesis of complexes with Th=O and Th=S multiple bonds [119]. By salt metathesis between **54** and MeLi, dimethyl metallocene complex **55** was synthesized (Scheme 9a), which could further react with *p*-toluidine to give bis-amido metallocene **56** in 90% yield. Finally, heating of the mixture of **56** and **55** gives base-free thorium imido complex **57** in 85% yield. In addition, by the cycloaddition-elimination reaction of **57** with Ph_2C=O or Ph_2C=S, complexes **58** were formed in good yield (Scheme 9a).

Further study revealed that terminal imido thorium complex **57** does not react with alkylsilyl halides but could react with unsaturated reagents, such as alkynes, to form complex **59** (Scheme 9b) [120]. Therefore, complex **57** can be viewed as an intermediate for the catalytic hydroamination of internal alkynes. In addition, complex **57** was also an efficient catalyst for the trimerization of PhCN. They found that thorium imido complex **57** could also react with $PhSiH_3$ and Ph_2SiH_2 *via* Si–H bond activation to form complex **60** (Scheme 9b) [121]. Further study reveals that the reactivity of Th^{4+} is more similar to that of an actinide than to that of an early transition metal.

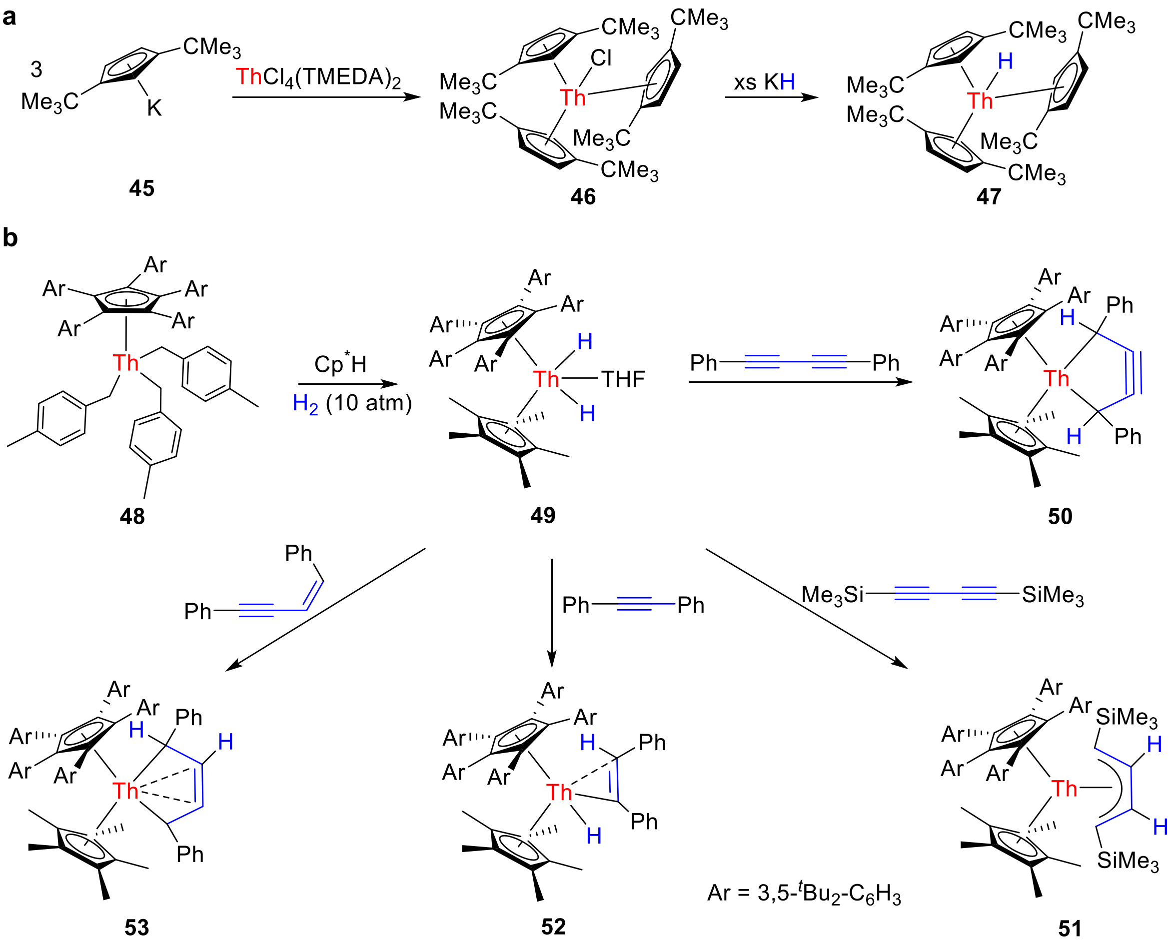

Scheme 8: Synthesis and reactivity of Th–H species. **a.** Reproduced with permission [116]. Copyright 2011, Elsevier. **b.** Reproduced with permission [117]. Copyright 2019, Royal Society of Chemistry.

The Th=N double bond in complex **57** could also react with organic azide and diazoalkane [122]. For example, tetraazametallacyclopentene **61** was formed by irreversible [2 + 3] cycloaddition reaction of **57** with *p*-azidotoluene (Scheme 9b). However, a novel diazenido iminatometallone **62** was generated by the reaction of complex **57** with 9-diazofluorene, in which the N=N bond was cleaved and the N atom was transferred to the Th=NR moiety (Scheme 9b). In addition, a series of 1,2-addition products **63** were formed by the reactions of complex **57** with pyridine derivatives, amines, chlorosilane, etc. (Scheme 9b) [123]. Therefore, this Lewis base-free thorium imido complex **57** exhibits excellent reactivity toward a series of organic substrates.

Zhang et al. also investigated the reactivity of a Lewis base-stabilized thorium imido complex **65**. As shown in Scheme 9c, complex **65** also exhibits broad reactivity toward a series of organic molecules but in a different reaction pattern compared with complex **57** [124]. This difference is probably due to the steric effects of the Cp ligands on the Th center, as the Cp* ligand in **65** provides a more open coordination space in comparison with the more sterically crowded 1,2,4-$(Me_3C)_3C_5H_2$ ligand in **57**.

Actinide terminal imido complexes exhibit unique electronic structures and diversified reactivity; thus, analogous actinide phosphinidenes are the next synthetic challenge. In 2018, Zhang and Wang et al. reported a stable example of base-free terminal actinide phosphinidene complex **68**, which was synthesized by the reaction of Mes*PHK (Mes* = 2,4,6-$(Me_3C)_3C_6H_2$) with thorium methyl iodide precursor **67** (Scheme 10a) [125, 126]. Complex **68** can also be synthesized by the reaction of thorium precursor **1** with 2 equiv. of Mes*PHK in THF [127]. DFT analysis reveals that the Th=P double bond is more covalent than the Th=N bond in the related terminal thorium imido metallocene. The Th=P bond was inert to the alkynes but could react with organic molecules such as isothiocyanate, CS_2, isonitriles, and so on. Interestingly, a three-membered

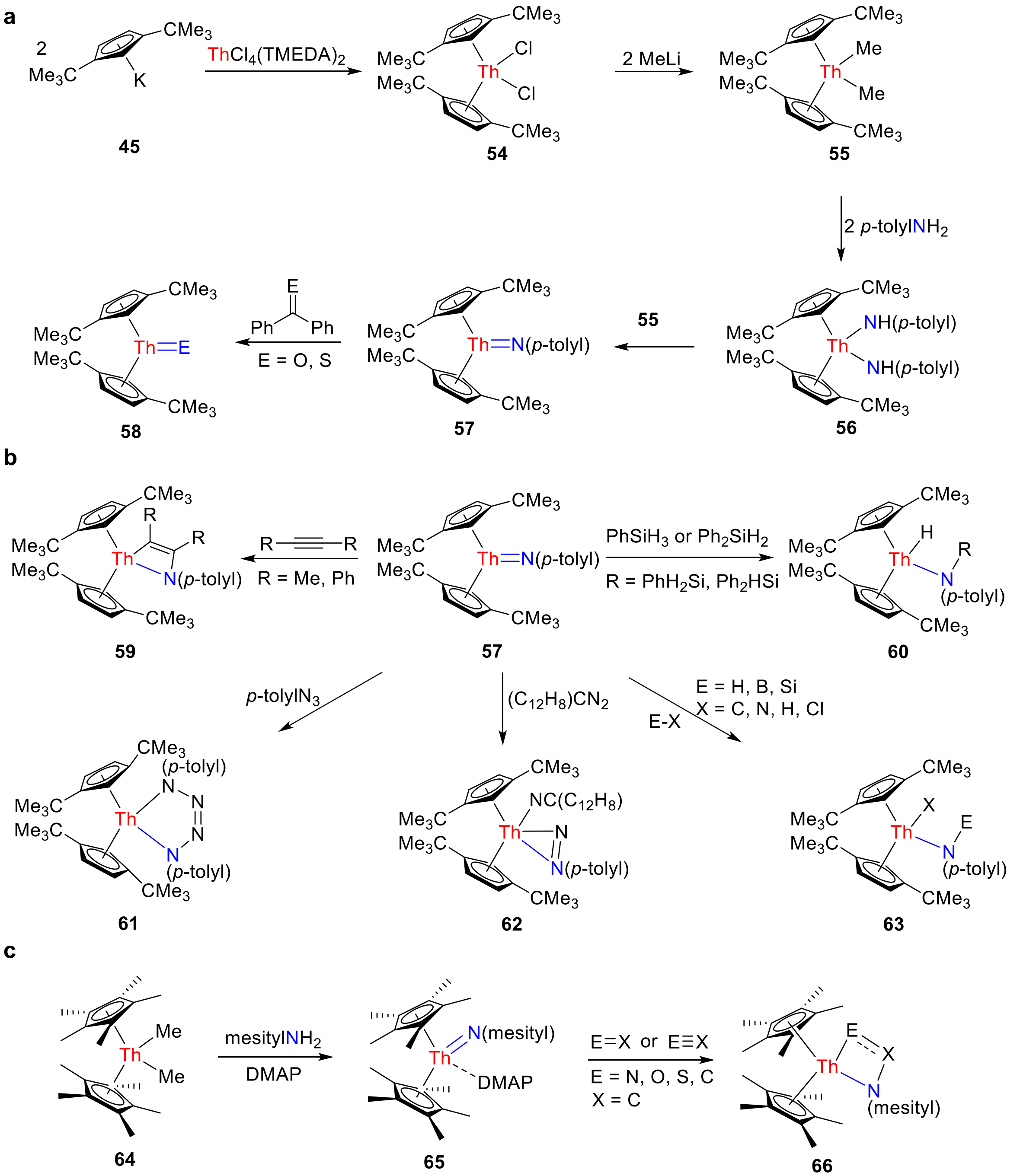

Scheme 9: Synthesis and reactivity of terminal imido thorium species. **a**. Reproduced with permission [119]. Copyright 2011, American Chemical Society. **b**. Reproduced with permission [120]. Copyright 2011, WILEY-VCH; Reproduced with permission [121]. Copyright 2014, Royal Society of Chemistry; Reproduced with permission [122]. Copyright 2014, WILEY-VCH; Reproduced with permission [123]. Copyright 2015, American Chemical Society. **c**. Reproduced with permission [124]. Copyright 2017, American Chemical Society.

metallaheterocycle with a Th–(η^2–P–P) unit was formed by the reaction of complex **68** with less sterically encumbered phosphine $PhPH_2$ [127]. The analogous complex with a Th–(η^2–P–P) unit exhibits more covalence between Th and P than the Th–C bond in the related thorium metallacyclopropene [128].

The different substituents on Cp and the phosphinidene will change the product. For example, the KCl-bridged thorium phosphinidene **73** was formed by the salt metathesis reaction of TippPHK (Tipp = 2,4,6-$^i Pr_3C_6H_2$) with the less steric crowded thorium methyl chloride precursor **72** (Scheme 10b) [129]. This complex can be viewed as a masked

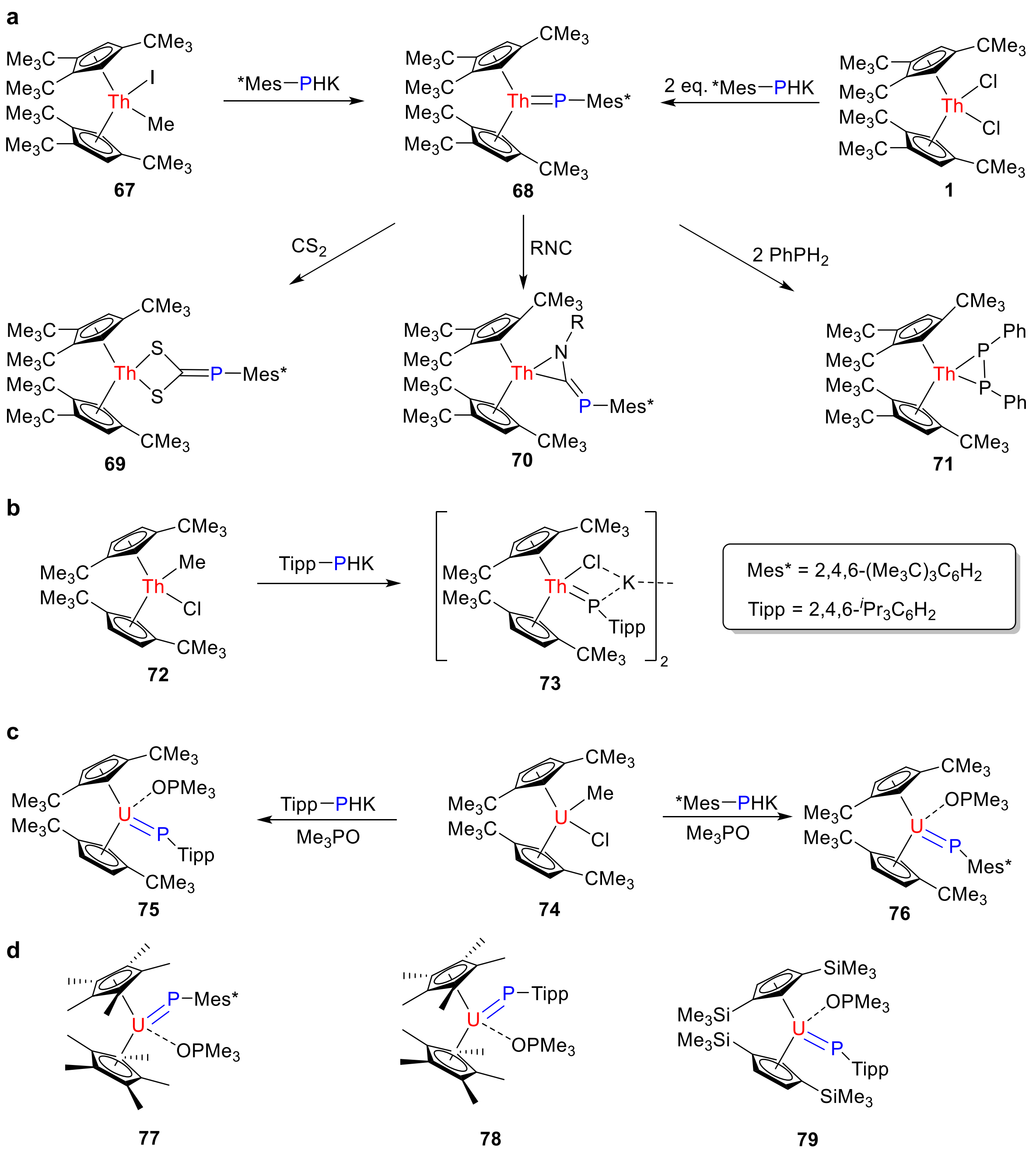

Scheme 10: Synthesis and reactivity of actinide phosphinidene species. **a.** Reproduced with permission [125]. Copyright 2018, American Chemical Society; Reproduced with permission [126]. Copyright 2018, Wiley-VCH. **b.** Reproduced with permission [129]. Copyright 2019, Royal Society of Chemistry. **c.** Reproduced with permission [125]. Copyright 2018, American Chemical Society; Reproduced with permission [129]. Copyright 2019, Royal Society of Chemistry **d.** Reproduced with permission [125]. Copyright 2018, American Chemical Society.

terminal thorium phosphinidene species when it reacts with organic molecules.

Lewis base-stabilized terminal uranium phosphinidene complexes **75** and **76** were isolated by the reactions of uranium methyl chloride complex **74** with 2,4,6-TippPHK or Mes*PHK in the presence of Me_3PO, respectively (Scheme 10c) [130, 131]. This U=P unit exhibits abundant reactivity toward a series of organic small molecules, such as aldehydes, imines, diazenes, isothiocyanates, carbodiimides, organic azides, nitriles, and isonitriles, yielding the corresponding uranium complexes in good yields. Subsequently, a series of Lewis base-stabilized terminal uranium phosphinidenes **77** – **79** were also synthesized via a similar method and showed high reactivities toward various organic substrates (Scheme 10d) [132, 133]. After elimination of the TippP: unit, uranium phosphinidene complex **78** can be viewed as a masked synthon of uranium(II), which can react with small organic molecules, including bipy, carbodiimides, organic azides, ketazines, diazenes, Ph_2S_2, and Ph_2Se_2 [134]. They found that the electronic properties and sterics of the substituent group on the cyclopentadienyl ligand and the coordinated Lewis bases can change the reactivity of uranium phosphinidene complexes [135].

A novel tripodal Trapen ligand was reported by Liu et al. in 2020 and could be used to stabilize uranium(IV) synthon ($U[Trapen^{TMS}][Cl]$) (**80**) [136]. Treatment of complex **80** with NaN_3 or $NaOCP(dioxane)_{2.5}$ formed the corresponding U(IV) complexes **81** and **82** via salt metathesis (Scheme 11a). However, a diuranium oxo complex ($(U[Trapen^{TMS}]_2[\mu\text{–}O]$) (**83**) was generated unexpectedly when complex **80** was reduced with KC_8. The μ–O atom in complex **83** probably comes from the THF solvent.

Recently, they found that by the salt-elimination reaction between $An(Tren^{TIPS})$ Cl precursors (**83**) and $NaOCP(dioxane)_{2.5}$, the corresponding uranium and thorium phosphaethynolate complexes **85** were isolated (Scheme 11a) [137]. DFT calculations reveal that the U–O σ bond in this species exhibits a more covalent character than the Th–O bond.

2.2.1.5 Complexes with An–M bond

Multimetallic complexes with metal-metal bonds have attracted attentions of chemists due to their fascinating structures and potential applications. Compared with prevalent transition metal-metal bonds, examples with actinide-metal bonds are rare, which is probably due to synthetic difficulties. In 2016, Yang et al. reported an example of thorium–copper heterobimetallic complex **86**, which was synthesized by the reaction of thorium imido complex **65** with copper(I) halides (Scheme 12a) [138]. Note that only the uranium(V) species was generated by the reaction of uranium(IV) imido with copper(I) halides [139, 140]. Complex **65** exhibits a short Th–Cu bond distance, which was consistent with the result of the donor–acceptor interaction between the Cu(I) and Th(IV) atoms.

In 2019, Feng et al. developed a straightforward strategy to synthesize a set of heterometallic clusters with four or six U–Ni bonds by a heptadentate N_4P_3 scaffold [141]. Complex **88** was synthesized by the reaction of $N[CH_2CH_2NLiP^iPr_2]_3$ with UCl_4, which could react with $Ni(COD)_2$ to form complex **89** in good yield (Scheme 12b). The formal oxidation state of uranium is +IV. By the reduction of **89** with KC_8, cluster **90** with four U(III)–Ni bonds was generated. The average U–Ni bond distances in **90** (2.844(9) Å) are significantly shorter than those observed in **89** (3.086(4) Å). Interestingly, a trimetallic bridged diuranium cluster **91** with six U–Ni bonds was constructed by the reaction of $Ni(COD)_2$ with an *in situ* generated U(III) intermediate (Scheme 12b). The U–Ni bond distances in this complex range from 2.775(3) to 2.967(2) Å, which are close to the sum of the covalent single bond radii for U and Ni (2.80 Å) [142]. These complexes

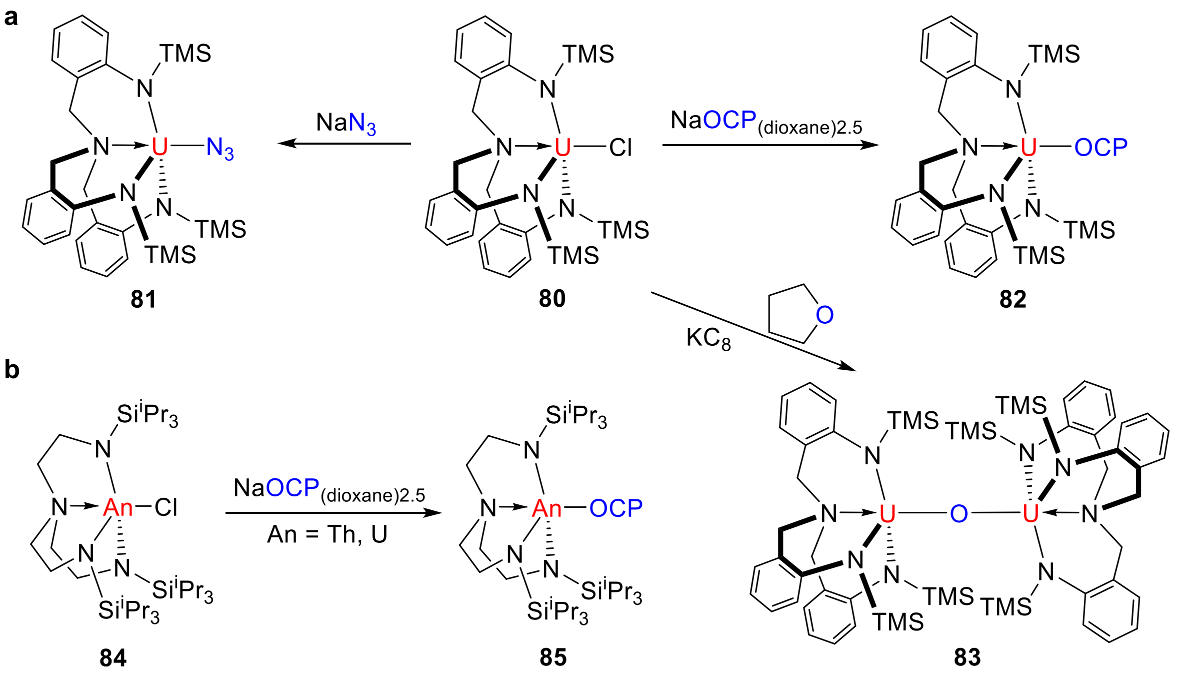

Scheme 11: Synthesis and reactivity of actinide species with tripodal ligand. **a.** Reproduced with permission [136]. Copyright 2018, American Chemical Society. **b.** Reproduced with permission [126]. Copyright 2018, Wiley-VCH.

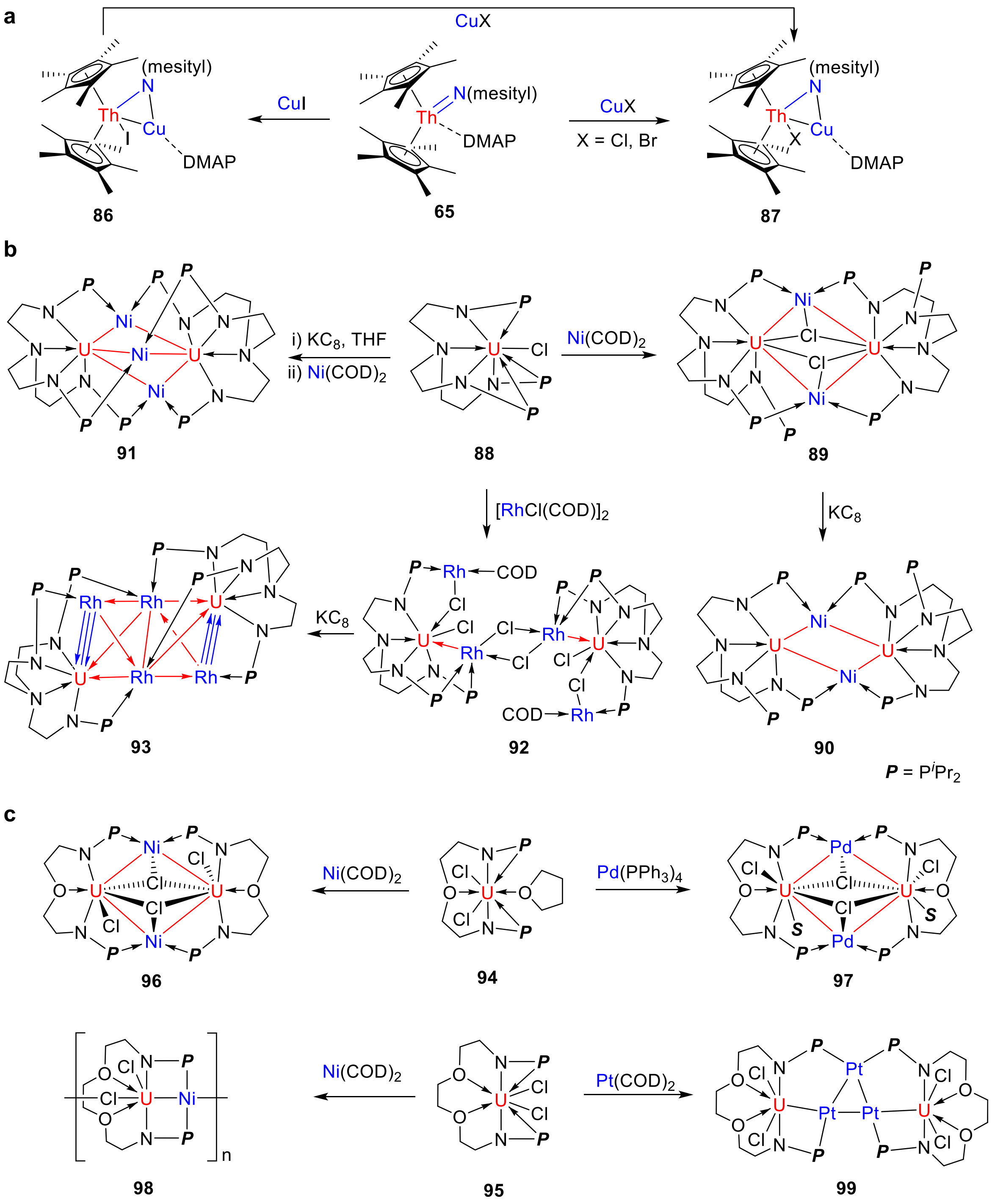

Scheme 12: Synthesis and reactivity of actinide species with An–M bond. **a.** Reproduced with permission [138]. Copyright 2016, American Chemical Society. **b.** Reproduced with permission [141]. Copyright 2019, Nature Publishing Group. **c.** Reproduced with permission [143]. Copyright 2020, Royal Society of Chemistry. **d.** Reproduced with permission [146]. Copyright 2019, NAS.

represent an unusual example of heterometallic clusters with multiple U–M bonds. DFT calculations show that the Wiberg bond index (WBI) for the strongly polarized U–Ni in **89** is 0.20, whereas it is up to 0.4 in complex **90**. Further theoretical analysis reveals that these clusters contain multiple polarized U–Ni bonds and a U–U interaction, and the electronic configurations of U(III) are $5f^2 6d^1$.

This study suggests that the trianionic N–P ligand is an effective scaffold for the synthesis of complexes with multiple U–M bonds. One year later, Feng et al. reported that dianionic N–P ligands could also be used to construct a series of U–M bonds. The different P–P distances in complexes **94** and **95** (6.069 *versus* 4.464 Å, respectively) will lead to different coordination modes when they react with transition metals (Scheme 12c) [143]. For instance, the reactions of complex **94** with $Ni(COD)_2$ or $Pd(PPh_3)_4$ generate heterometallic clusters **96** and **97** with four U–Ni or U–Pd bonds, respectively. However, the reaction of complex **95** with these transition metals affords complexes with single U–M bonds, mainly due to the shorter P–P distance in complex **95**. In addition, the first example of a complex with multiple U–Pt bonds was constructed by the reaction of **95** with $Pt(COD)_2$ (Scheme 12c). This study further highlights the importance of ligands in the synthesis of U–M bonds.

Although transition metal-metal multiple bonds have been extensively studied, the construction of complexes with actinide–metal multiple bonds are significantly more challenging. Two important advances are the isolation of a double dative U–Rh bond by Liddle and coworkers [144] and the generation of a U–Fe triple bond under laser vaporization in the gas phase by Zhou, Li and coworkers [145]. No examples of structurally authenticated actinide–metal triple bonds were reported until 2019. Feng et al. isolated an example of complex **93** with two U–Rh triple bonds by the reduction of complex **92** with KC_8 (Scheme 12b) [146]. The U–Rh triple bond length (2.31 Å) in complex **93** is close to the sum of the covalent triple bond radii of U and Rh (2.24 Å). DFT investigations found that the WBI for the two U–Rh triple bonds is 2.61, whereas the WBI for other U–Rh bonds is only 0.85. Further study reveals that the nature of the U–Rh triple bond is one covalent σ bond with two Rh–to–U dative bonds.

2.3 Actinide endohedral metallofullerenes

Fullerene is the only molecular carbon allotrope with a spherical structure. One of the most attractive structural characteristics of fullerenes is their hollow cage cavity, which creates a unique confined chemical environment and are capable of encapsulating and stabilizing metal ion or metallic cluster species. These host-guest molecules are called endohedral metallofullerenes, which have attracted significant attention in the past three decades due to their potential applications in photovoltaic devices [147], biomedicine science [148], single-molecule magnets [149], and molecular devices [150]. Among various EMFs, actinide EMFs show unique structural and electronic properties, such as characteristic bonding containing 5*f* electrons, flexible oxidation states, and physicochemical properties.

Most of the studied EMFs are based on lanthanide metal ions or clusters. In 2001, Akiyama and his co-workers reported the first isolation of $An@C_{82}$ (An=U, Np, and Am) by high-performance liquid chromatography (HPLC) and the ultraviolet-visible-near infrared (UV–vis-NIR) absorption spectrum of $U@C_{82}$ [151]. They suggested that the oxidation state of U in $U@C_{82}$ is +3 because of its similar UV spectrum to that of $Nd@C_{82}$. Later, the same group performed the L_{III}-edge X-ray absorption near edge structure (XANES) spectroscopy for $U@C_{82}$ and $Th@C_{84}$ and further confirmed the +3 oxidation state of U inside C_{82} [152, 153]. Although $Th@C_{84}$ showed a lower energy side than that of the reference material of $Th(NO_3)_4{\cdot}2H_2O$, they concluded that the oxidation state of encapsulated Th ion is more likely to be +4 rather than +3 due to the more reductive chemical environment inside the fullerene cage. In 2012, Kroto and his co-workers suggested that as the smallest U–based EMF detected in the experiment, $U@C_{28}$ showed a strong formation in a carbon-vapor-rich environment and acted as the precursor for other larger U EMFs, following the bottom-up growth mechanism [154]. Actinide EMFs has also been investigated by the theoretician who worked on both fullerenes and actinides [155, 156]. In 2012, Dai and Liu et al. investigated the electronic structure of isomers of $U@C_{82}$ by computational methods [155–157]. Actinide dimetallic fullerenes, which the possibility of stabilizing actinide metal-metal bond, has drawn considerable attention from computational research. In 2007, Lu and Wu performed the theoretical calculations for $U_2@C_{60}$, of which the electronic structure has been confirmed as $(U_2)^{6+}@(C_{60})^{6-}$ [158]. They also proposed that the encapsulated U_2 formed U–U sixfold one-electron-two-center bonds with a U–U distance of 2.72 Å. Straka and coworkers also made a systematic computational study, in which they concluded that the U–U bond inside fullerene cage C_{80} is an ‘unwilling’ bonding formed only by the confined space inside fullerene cage [159].

These important early studies proved the existence of actinide EMFs by using mass, HPLC, absorption spectroscopy, and DFT predictions [160–169]. However, these studies were not able to determine the detailed structures and physicochemical properties of actinide EMFs, which largely hinder the fundamental understanding of these unique actinide compounds. A significant advance was made by Wang et al. in 2017 [170]. They reported the X-ray crystallographic characterization of $Th@C_{3v}(8)$–C_{82}, which unambiguously determined the endohedral molecular structure of actinide EMFs for the first time [171]. Following studies expand actinide EMFs to a large family of which includes mono-metallofullerenes, di-metallofullerenes and clusterfullerenes. With the experimental developments of actinide EMFs, the theoretical structural calculations, mainly contributed by Jin [172–176] and Zhao [177–182] groups, are also booming [183–185]. These studies revealed fascinating host-guest molecular structures, unique actinide-carbon cage interaction and unprecedented actinide bonding behaviors. In this section, we summarize the recent advances of actinide EMFs, focusing on their preparation and molecular and electronic structures.

2.3.1 Preparation of actinide EMFs

As mentioned above, the first actinide EMF was synthesized by the laser ablation method in 1992. However, only microscopic amount of products could be obtained, which hindered the systematic characterization of these novel compounds. Krätschmer-Huffman direct-current (DC) arc-discharge method are the most commonly used methods for milligram-scale production of EMFs, which was found to be a feasible synthetic method also for actinide EMFs [170]. Briefly, a drilled graphite rod was packed with the mixture graphite powder and metal oxides, such as ThO_2 or U_3O_8, at a metal/C atomic ratio of 1:24. This packed graphite rod was installed in an arcing reactor as the anode and then preheated under 175 A direct current for 30 min through the close contact with a graphite cathode. The preheating process could also be performed alternatively through a tubular furnace at 1000 °C for 12 h under the protection of the N_2 atmosphere. After the preheating treatment, the arcing reaction was performed between the anode and the cathode under 90–110 A direct current in a vacuumed arcing reactor with 200 Torr He as the atmosphere. If the targeted EMFs are nitride clusterfullerenes, N_2 or NH_3 is also needed as the reactive nitrogen source. After the arcing, product soot containing actinide EMFs was collected and then extracted by CS_2 solvent. The resulting fullerene solution was filtered and then concentrated for further HPLC separation. Multistage HPLC processes was then employed for the isolation and purification of the targeted actinide EMFs.

2.3.2 Structures of actinide EMFs

2.3.2.1 Mono-metallofullerenes

In 2017, Wang et al. reported the first actinide endohedral fullerene $Th@C_{3v}(8)–C_{82}$ with unambiguous structural characterization [170]. Inside this fullerene cage, the Th ion is located at an intersection of three hexagons with a short Th–C distance of 2.340(14) Å, indicating the strong Th-cage interactions. The combined experimental and theoretical study further confirmed that the encapsulated Th ion transferred four electrons to the $C_{3v}(8)–C_{82}$ cage, a unique metal-cage interaction never being revealed before. In addition, $Th@C_{3v}(8)–C_{82}$ shows strong photoluminescence (PL) emission both in CS_2 solution and in the solid state, which is rare among EMFs as previous studies have shown that, for lanthanide EMFs, the PL signals are generally quenched by the self-absorption of the fullerene cage and cannot be observed. The mechanism of this photoluminescence is proposed as the result of a charge transfer from the fullerene to the Th 6*d* orbital. This study confirms the endohedral structure of actinide EMFs for the first time and paved way to the following systematic investigations of these novel actinide compounds.

Soon after the successful synthesis and characterization of $Th@C_{3v}(8)–C_{82}$, Echegoyen, Poblet and Chen et al. reported first family of the uranium based actinide EMF, which includes $U@D_{3h}–C_{74}$, $U@C_2(5)–C_{82}$, and $U@C_{2v}(9)–C_{82}$ [186]. The theoretical results suggested that, for $U@D_{3h}–C_{74}$ and $U@C_2(5)–C_{82}$, the encapsulated U transfer 4 electron to the cages, resulting in their tetravalent electronic configurations, i.e. $U^{4+}@(D_{3h}–C_{74})^{4-}$ and $U^{4+}@(C_2(5)–C_{82})^{4}$. For $U@C_{2v}(9)–C_{82}$, however, only three electrons are transferred from U to the C_{82} cage, resulting in an open-shell electronic structure of $U^{3+}@(C_{2v}(9)–C_{82})^{3-}$. This work revealed that the oxidation states of the encapsulated U ions are variable depending on the isomeric cage structures.

Following research shows that by encapsulating U or Th ion, novel fullerene structures, which could not be obtained before, can be stabilized in the form of actinide EMFs. In 2019, Cai et al. reported three novel IPR-violating mono-metallofullerenes, including $Th@C_1(28{,}324)–C_{80}$ and two U-based mono-metallofullerenes, $U@C_1(17{,}418)–C_{76}$ and $U@C_1(28{,}324)–C_{80}$ [187]. Herein, IPR, abbreviated from the isolated pentagon rule [188], states that the pentagons in fullerenes are separated and surrounded by five hexagons. IPR-violating or non-IPR fullerenes that contain moieties with fused pentagons, such as a pentalene, are generally not stable because of the high strain of fused pentagons. In this work, X-ray crystallographic study shows that the encapsulated actinide ion is located over the [5,5] bond of the pentalene moiety of the corresponding fullerene cages. The stabilization of these non-IPR cages is caused by the four-electron transfer and strong host-guest interaction between the pentalene moiety and the encapsulated actinide ion. Theoretical studies also suggested that the actinide ion has strong covalent interaction with the fullerene cages, which attributes to the unusual stabilization of these pristine Non-IPR cages by single metal ion.

Besides Non-IPR fullerene cages, the strong actinide-cage interaction can also lead to the stabilization of novel IPR cages. Wang et al. reported a novel Th-based monometallofullerene with a chiral carbon cage, $C_1(11)–C_{86}$ [189]. The DFT result has predicted that this cage is the most thermodynamically stable isomer, which, however, has never been observed in the previously reported lanthanide EMFs. The stabilization of this chiral cage is mainly attributed to robust Th-cage interaction with a four-electron transfer, leading to a stable closed-shell electronic structure. In the following studies, Chen and his collaborator reported four novel IPR mono-metallofullerenes containing a single Th ion, i.e. $Th@T_d(2)–C_{76}$ [190], $Th@D_{5h}(6)–C_{80}$ [191], $Th@C_2(5)–C_{82}$ [192], and $Th@C_{2v}(9)–C_{82}$ [192]. Among them, the highly symmetrical fullerene cages, $T_d(2)–C_{76}$ and $D_{5h}(6)–C_{80}$, were stabilized by a single metal ion instead of a lanthanide cluster for the first time. $D_{5h}(6)–C_{80}$, which generally exhibits a hexavalent electronic configuration in lanthanide EMFs. However, in $Th@D_{5h}(6)–C_{80}$, it was stabilized by the four electron transfer from Th for the first time. In particular, for $Th@C_{2v}(9)–C_{82}$, the theoretical results pointed out that encapsulated Th ion also transfers four electrons to the cage of $C_{2v}(9)–C_{82}$, different from the three electron transfer for the above mentioned $U^{3+}@(C_{2v}(9)–C_{82})^{3-}$, which share the same fullerene cage with $Th@C_{2v}(9)–C_{82}$. This suggests that, besides the cage isomeric structure, the nature of the actinide ion also has a major impact on the metal-cage charge transfer. These works also confirmed the remarkably different electronic structures and metal-cage interactions of actinide EMFs from those of the previously reported lanthanide EMFs.

Very recently, Echegoyen et al. carried systematic structural studies on the U-based mono-metallofullerenes. In 2020, they reported the structural characterizations of three new monometallic uranium metallofullerenes, $U@D_2(21)–C_{84}$, $U@C_s(15)–C_{86}$, and $U@C_1(11)–C_{86}$ [193]. In this report, the authors proposed a topological interconversion map via either top-down or bottom-up processes based on the characterized U-based mono-metallofullerenes. In 2021, they reported the successful synthesis and structural characterizations of four novel U mono-metallofullerenes, $U@C_s(6)–C_{82}$, $U@C_2(8)–C_{84}$, $U@C_s(15)–C_{84}$, and $U@C_1(12)–C_{86}$ [194]. In this study, the charge transfer between the fullerene cage and the encapsulated metal ion was found to play a crucial role in the determination of the metal positions, in which the metal ions are always located on the symmetry plane of the fullerene cage as long as the cage is mirror-symmetrical. Although this “mirror rule” was revealed from the study of the four actinide EMFs, after a thorough survey, the authors concluded that it in fact applies to all the reported EMFs so far, including both actinide mono-metallofullerenes and lanthanide mono-metallofullerenes, regardless of the cage size and isomeric structure.

Figure 6 summarized the molecular structure of the above-discussed actinide mono-metallofullerenes.

2.3.2.2 Di-metallofullerenes

Actinide metal-metal bond has been a longstanding puzzle for actinide elementary chemistry. Though intensively studied by theoreticians, the experimental work on this kind of chemical bond is extremely rare [195]. Fullerenes, with this confined nano space and ability of stabilizing metal ions through charge transfer, became an ideal nanocontainer to study this elusive bonding motifs. Early theoretical studies have predicted the existence of actinide metal-metal bond inside fullerene cages. Lu and Wu predicted a bimetallic uranium fullerene $U_2@C_{60}$ with a U–U bond in 2007 [158]. Later, Straka et al. predicted that in $U_2@C_{80}$, the U_2 dimer bears a one-electron-two-center with a U–U distance of 3.9 Å [159]. Although many theoretical studies have predicted the existence of the U–U bond, the experimental evidence had been missing until 2018, when Zhang et al. reported the first crystallographic structure of Di-metallofullerene, $U_2@I_h(7)–C_{80}$, in which a U_2 dimer is trapped inside a highly symmetrical fullerene cage, $I_h(7)–C_{80}$ [196]. The crystallographic results show that the U–U distance is 3.79 Å, a little shorter than the predicted value. The X-ray absorption spectroscopy (XAS) showed that the U L_3-edge of $U_2@I_h(7)–C_{80}$ was similar to the reference sample of uranium sulfate (U^{3+}) and $U^{3+}@(C_{2v}(9)–C_{82})^{3-}$, proving that the oxidation states of the two U ions inside the $I_h(7)–C_{80}$ are both +3, in good agreement with the computational studies and formal state of an $(I_h(7)–C_{80})^{-6}$ cage. In particular, the theoretical calculations revealed a weak U–U bonding interaction between the two U ion, which slightly depends on the redox behavior of the fullerene. The U–U interaction is strengthened upon reduction and weakened upon oxidation because the formal oxidation states of U change from +2.5 upon reduction to +3.5 upon oxidation.

Metal-metal bond between the low valence Th(III) has been predicted by Hu and Kalsoyannis el at by quantum-chemical computational study [197]. In 2020, Zhou and Dai et al. predicted a Th–Th bond stabilized inside an $I_h(7)–C_{80}$ fullerene cage with the electronic configuration of $(Th_2)^{6+}@(I_h(7)–C_{80})^{6-}$ and the Th–Th distance of 3.803 Å [198]. This prediction was soon experimentally confirmed by Zhang et al., who reported the combined experimental and theoretical study of $Th_2@I_h(7)–C_{80}$ with precise structural characterization [199]. The crystallographic results showed that the Th–Th distance is 3.816 Å, in agreement with the theoretical prediction. The encapsulated Th ion

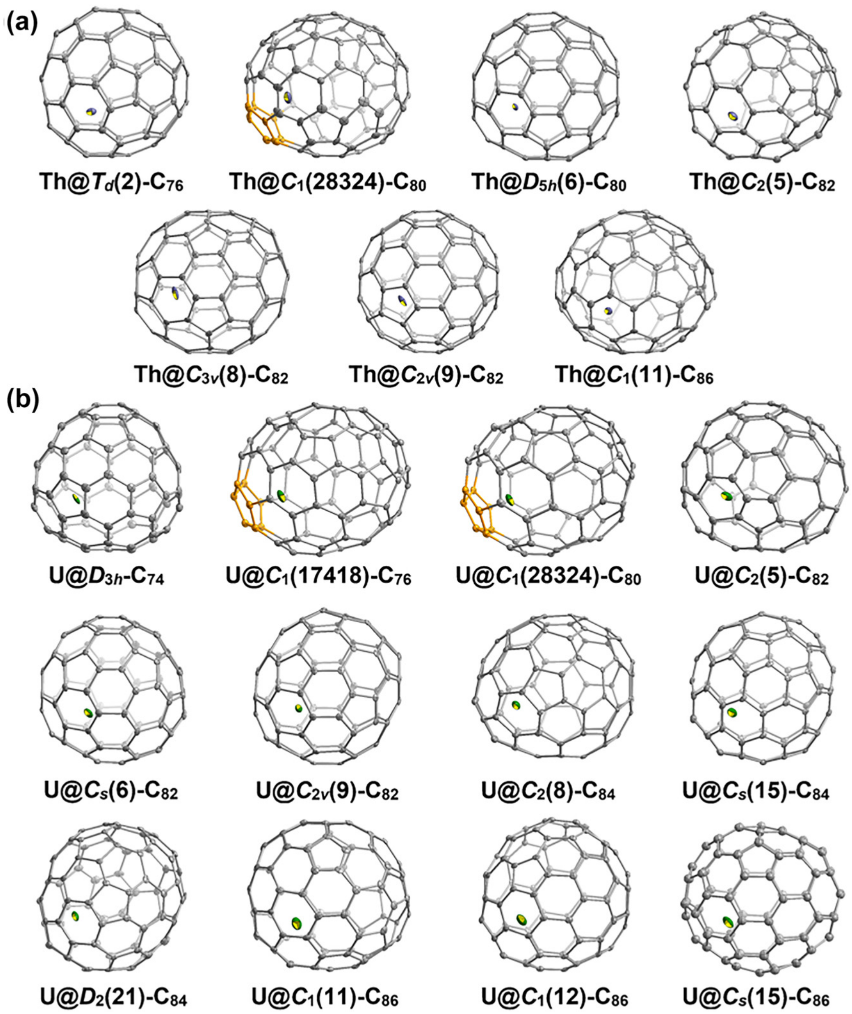

Figure 6: Molecular structures of the reported (a) Th-based mono-metallofullerenes and (b) U-based mono-metallofullerenes.

exhibited a rare oxidation state of +3, confirmed by the XANES spectroscopy with a shift to lower energy by 4.7 eV, compared to that of ThO_2 (Th^{4+}). As a result, the Th_2 dimer transfers six electrons to stabilize the $I_h(7)–C_{80}$ cage and form a strong Th–Th covalent bond with an effective bond order of 0.99. Furthermore, the theoretical results suggested that the Th–Th bond still prevails in a distance as long as 6.02 Å when encapsulated inside a giant fullerene cage, such as $D_2(821)–C_{104}$. This is caused by the large overlap of the 7*s*/6*d* hybrid Th orbitals, due to the small energy gap between the $\sigma(7s/6d_{z2})$ and $\sigma^*(7s/6d_{z2})$ orbitals.

2.3.2.3 Actinide clusterfullerenes

In 2018, Zhang et al. reported the first actinide clusterfullerene, $U_2C@I_h(7)–C_{80}$, with unambiguous structural characterizations [200]. In this novel actinide compound, an unprecedented bent U=C=U cluster is stabilized inside fullerene cage. The theoretical calculations confirmed that the oxidation states of the two encapsulated U ions are both +5. The U_2C cluster transferred a total of six electrons to the $I_h(7)–C_{80}$ cage. In particular, the encapsulated U_2C cluster has a symmetrical configuration with two equivalent U=C double bonds (2.033(5) and 2.028(5) Å), which is the shortest U–C bond observed at the time. Theoretical studies reveal that this U=C bond is the unsupported axial U=C bond, which has never been obtained in a molecular compound before. In addition, computational study also indicated that the bent in the U=C=U unit is caused by the highly electronegative central carbon, which results in an sp^1/sp^2-hybridized type geometry. The discovery of this unsupported U=C bond confirms the distinction between "diagonal" and "poly-coordinated" uranium, and between "axial" covalent and "equatorial" dative bonding mechanisms. This work provides a deeper understanding of the fundamentals of the uranium bonding behavior. Moreover, it revealed the exceptional capability of fullerenes as nanocontainer to stabilize rare and reactive actinide clusters.

Soon after this study, Fuertes-Espinosa et al. reported the isolation of a new carbide clusterfullerene, $USc_2C@C_{80}$, the first mixed-metallic actinide-based EMF, using a non-chromatographic purification methodology [201]. However, the crystallographic characterization of this novel compound was not present in this study. It was two years later, that Li et al. reported the crystallographic structure of this clusterfullerene [202]. Compared to $U_2C@C_{82}$, one U=C bond was replaced by two Sc–C single bond the USc_2C cluster, which presents a triangular configuration with a carbide bridge connected with three metal ions. The two Sc–C single-bonds were measured as 2.053(6) and 2.060(6) Å. The U=C double bond distance is 2.011(5) Å, which is even slightly shorter than in $U_2C@I_h(7)–C_{80}$. The U and two Sc ions exhibit the oxidation states of +4 and +3, respectively. Thus, the whole cluster transfers six electrons to the fullerene cage with the electronic configuration described as $(USc_2C)^{6+}@(C_{80})^{6-}$.

Besides carbide clusterfullerene containing only one carbon atom, in 2019, Zhuang et al. reported another kind of carbide clusterfullerene with a U_2C_2 cluster trapped into two highly symmetrical fullerene cages, namely, $U_2C_2@D_{3h}(7)–C_{78}$ and $U_2C_2@I_h(7)–C_{80}$ [203]. The encapsulated U_2C_2 clusters presents a quite unique butterfly-like structural configurations which two U ions bridged by a C≡C unit, which has never been reported either by experimental or theoretical study. Moreover, though adapts similar configuration in both cages, U_2C_2 is more stretched in C_{78} than in C_{80}, showing exceptional flexibility. The U–C interactions in both U_2C_2 clusters show characteristic distances for U–C single bonds. In particular, different from that in $U_2C@C_{80}$, the two encapsulated U ions in both fullerene cages exhibit the oxidation state of +4. Thus, in total, the U_2C_2 cluster also transfers six electrons to the two fullerene cages, substantially different from the 4-electron transfer from the conventional Ln_2C_2 cluster to the fullerene cage. This work further demonstrates that the combination of the unique encapsulation effect of fullerene cages and the variable oxidation states of actinide elements can lead to the stabilization of novel actinide clusters, which are not accessible by conventional synthetic methods.

In early 2021, Li et al. reported a novel uranium nitride clusterfullerene, $U_2N@I_h(7)–C_{80}$ [204]. The crystallographic results show that the two encapsulated U ions are bridged by a nitrogen atom, forming a novel U_2N cluster, which features an unusual unsymmetrical structure with the two U–N distances of 2.058(3) Å and 1.943 Å, indictive of two unsymmetrical U=N double bonds. Similar to the U_2C cluster in $U_2C@I_h(7)–C_{80}$, the configuration of the U–N–U cluster is also bent with a bond angle of 150.0(2)°. The theoretical calculations revealed that the two U ion in this cluster adapt mixed oxidation state of U(V) and U(IV), which results in the electronic configuration of $(U(V)=N=U(IV))^{6+}@(I_h(7)–C_{80})^{6-}$.

The unusual bonding behavior of U in the encapsulated cluster was further highlighted by a very recent report of $UCN@C_s(6)–C_{82}$ by Chen' et al. In this novel cyanide clusterfullerene, the encapsulated U ion is bonded to a cyanide group with an η^2 (side-on) coordination, forming a triangle cluster of UCN, unprecedented for the uranium cyanides [205]. The electronic configuration of the EMF molecule can be described as $(U^{3+}[CN]^{-})^{2+}@(C_s[6]–C_{82})^{2-}$ in which the U ion adopts formal oxidation state of +3, transferring one electron to the cyanide group and two electrons to the fullerene cage. Interestingly, in this case, the significant donation bonding from the fullerene and cyanide to the uranium makes the resulting system qualitatively difficult to distinguish from neutral UCN with U(I) encapsulated in neutral C_{82}. In other words, the theoretical analysis suggests that the oxidation state of encapsulated U shows ambiguity between U(I) and U(III).

3 Exploration on the application of actinide compounds

3.1 Adsorption and separation

The removal and separation of both radioactive and nonradioactive contaminants from aqueous solutions and gas phases have received considerable attention in recent years due to ever-increasing environmental concerns [206–208]. The stability, porosity and charge density are crucial factors for the removal efficiency of the adsorbents [209]. Actinide based MOFs are considered suitable candidates for accomplishing this task. This class of materials is now employed for a variety of guest adsorption and separation processes. In 2016, a 3D interlocked framework was prepared, which shows marked hydrolytic stability and radiation resistance. The material could also remove Cs^+ from aqueous solution with rapid adsorption kinetics. Ai et al. also directed the construction of uranyl based MOFs materials for the removal of Cs^+ from aqueous solutions [70]. In 2017, the first mesoporous cationic MOF (SCU-8) was obtained through ionothermal reaction [46]. The large pore size and void space in the framework of SCU-8 combined with the charged skeleton offer the possibility of removing anionic pollutants. Batch experiments suggest that anion pollutants with different sizes and geometries including $Cr_2O_7^{2-}$, ReO_4^-, methyl blue (MB) and perfluorooctane sulfonate (PFOS) could be efficiently removed. Actinide based cationic MOFs have also been employed for the removal of many other anionic pollutants, such as IO_3^- [59], and ReO_4^- [60, 76, 210] as developed by Chinese researcher. UOFs and TOFs could also serve as I_2 adsorbents, as demonstrated by Zhang et al. [211], Zhang et al. [212], Li et al. [55], Kong et al. [64], and Li et al. [57]. The most predominant capability of these materials is their superior resistance to radiation and marked adsorption capacity. In addition, several researchers have concentrated on dye degradation and sorption by uranyl or thorium-based MOFs, which show some advantages in terms of chemical stability or catalytic efficiency. In departure from establishing charged MOFs with promising sorption capability, this class of porous materials was also introduced into gas separation. A robust giant drum-like hydrophobic $[Co_{24}U_6]$ nanocage based MOF was developed by Luo et al. [213], and the material could selectively remove SO_2 over CO_2 and N_2 under both drying and humid conditions. DFT calculations revealed that the open U sites loaded in the structure greatly contribute to the SO_2 sorption capability. Recently, a tetrazole functionalized thorium organic framework was designed and synthesized by Xu et al. [49]. The material not only exhibits exceptional chemical resistance but is also capable of separating C_2H_4 from $C_2H_4/C_2H_2/C_2H_6$ mixture. The greater van der Waals (vdW) interaction between ethane molecules and Azole-Th-1 than ethylene is considered the direct reason that the material exhibits excellent separation capability. Chen and his collaborator developed many uranyl containing MOFs and systematically investigated the structure design strategy [214], photoluminescence [215], photocatalysis [216], and photocurrent [39]. Functionalizing the MOF skeleton with a Th^{4+} open metal site (OMS) has also been realized recently [45]. A new TOF (SCU-11) with removable coordinated water molecules was constructed. The large cavities in the framework are suitable for holding noble gases such as Kr and Xe. Actinide containing materials offer an alternative approach to both contaminant purification and small molecule separation.

Crystallization separation is a method to separate different metals by using the distinction of metal coordination properties. Compared with liquid extraction, this strategy is simple without repeated operations, and the treatment process is greener and environmentally friendly. In addition, it is fundamentally different from the traditional separation method based on the change of thermodynamic parameters with atomic number increment [217, 218].

Wang et al. reported a single-step and quantitative decontamination strategy of thorium from rare earths based on preferential coordination toward tetravalent f-cations over trivalent lanthanides using highly polarized inorganic ligands [219]. This selenite crystallization system is highly selective to trap tetravalent f-blocks while all other trivalent lanthanides completely remain in solution when they coexist. The separation factors of Th(IV)/La(III), Th(IV)/Eu(III) and Th(IV)/Yb(III) binary systems after one round of crystallization were reported as 2.1×10^5, 1.2×10^5, and 9×10^4, respectively. In addition, the first-principles calculation results illustrate that the lattice energies of tetravalent f-blocks (Ce^{4+} and Th^{4+}) compounds is significantly higher than those of trivalent lanthanide compounds, which is contrasted with typical natural and synthetic systems, where trivalent and tetravalent f-block elements often cocrystallize. This method provides a simple and environmentally friendly thorium decontamination strategy from rare earth elements (Figure 7).

3.2 Photoelectric functional materials

3.2.1 X-ray detection

UO_2^{2+}, the only species of uranium that has an emissive nature, was recently realized as a promising activator for building luminescent materials. As the last abundant naturally occurring element in the periodic table, uranium has a much higher atomic number than lead, thallium, and tungsten. This trait endows uranyl-containing materials with high radiation stopping power. Second, the luminescence originating from the charge transfer between the 5*f* orbital of uranium and the 6*d* orbital of uranyl oxygen is partially forbidden rather than totally forbidden [220]. This characteristic contrasts sharply to that of lanthanide emitters, leading to high light output and robust emission intensity [61]. In these considerations, uranyl is an excellent candidate for building radiation detection materials. First, we would like to describe the luminescence intensity variation of a uranyl-organic framework under ionizing radiation [221]. The emission intensity of the material was rapidly quenched under X- and γ-ray irradiation, indicative of high sensitivity toward ionizing radiation. The detection limits toward X- and γ-ray are all determined to be at the level of 10^{-4} Gy, representing a record value among all the chemical dosimeters before the presented material. EPR analysis revealed that stable radicals were generated under this radiation, and the removal of the radiation source didn't improve the luminescence intensity recovery. In this situation, the material is able to chemically accumulate the radiation dose. This detection method is rarely reported in chemical dosimeters, and allows for the detection of radiation at extremely low doses. This phenomenon has been observed in many other photochromic crystals, and offers a pleasurable reusability [222–224]. Radiation-

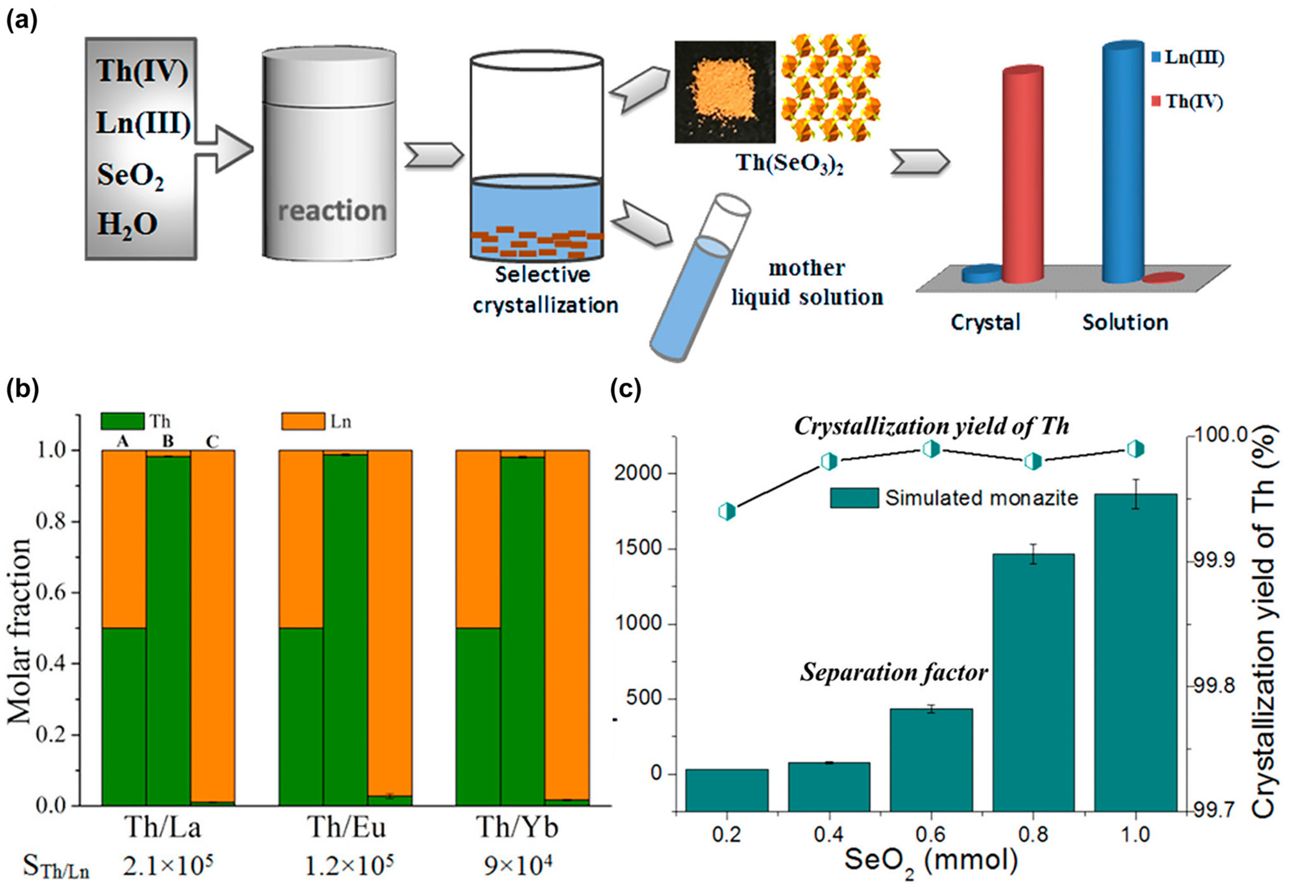

Figure 7: (a) Description of the process for the selective crystallization of tetravalent Th from REEs. (b) Separation results of Th/La, Th/Eu, Th/Yb crystallization experiment. A, B, and C represent the molar distribution of Th/Ln in the starting material, solid product, and mother liquid solution, respectively. (c) Separation results of thorium from a simulated monazite composition. Reproduced with permission [219]. Copyright 2018, American Chemical Society.

induced luminescence quenching was also observed in another 1D uranyl-bearing coordination polymer [225]. The radicals generated under UV light irradiation were also confirmed to be responsible for the emission quenching process [223, 226]. The difference comes from the position of the generated radicals and the detection sensitivity.

Another popular strategy for radiation detection is through the scintillators that can convert X-ray or γ-ray to visible light. Materials that serve as scintillators include inorganic materials [227], inorganic-organic hybrid materials [228] and plastics [72, 229]. Organic scintillators are highlighted because of their flexibility and designability. In 2018, Wang et al. reported the first case of a uranyl-organic framework based scintillator [72]. Incorporating uranyl into a robust coordination polymer, uranium-bearing scintillator (**SCU-9**) with high X-ray stopping power, high radiation and hygroscopic resistance was successfully obtained. **SCU-9** is a self-activated scintillator, which is different from some traditional scintillators such as NaI:Tl and CsI:Tl. As the X-ray power proportionally increased, the X-ray excited luminescence (XEL) intensity linearly increased in the same manner as that of the commercially available CsI:Tl scintillator, initially confirming its the practical utilization. The X-ray stopping power could also be enhanced by changing the crystal host. A series of inorganic crystals bearing uranyl with higher density were constructed, including $Na(UO_2)B_6O_{10}(OH)\cdot 2H_2O$ [230], $K(UO_2)(PO_4)\cdot 4H_2O$ (UPO), $Na_2(UO_2)(MoO_4)_2\cdot(H_2O)$ (UMO) [30], and $Na_2(UO_2)GeO_4$ (UGO) [231]. Compared with **SCU-9**, all inorganic uranyl-bearing scintillators exhibit much higher X-ray attenuation coefficiency (XAC) except for UBO. The effective atomic number (Z_{eff}) even close to that of commercial scintillators with the highest Z_{eff} value and is overwhelmingly larger than that of CsI:Tl, indicating a great promise for building more advanced uranyl-containing scintillators. Very recently, Lu et al. reported a radiation dosimeter based on a thorium containing discrete nanocluster (Th-SINAP-100). The material exhibits dual-module photochromic transitions when exposed to UV, β-ray, and γ-ray irradiation. The intermolecular charge transfer process could be facilitated by the enhanced π–π stacking interaction as confirmed by single crystal X-ray diffraction analysis and density functional theory (DFT) calculations. Uranyl or thorium-based coordination polymers are suitable candidates for the fabrication of high energy radiation detection platforms.

3.2.2 Heavy metal and organic molecule detection

Several actinide elements also exhibit bright luminescence through a charge transfer process (e.g. U^{6+}) or self-excited luminescence. Hence, fabrication of a luminescent sensor toward various ions is possible. Pioneered works are focusing on the fabrication of metal ion probes. In 2018, Liu et al. developed a 2D uranyl coordination polymer with efficient luminescence intensity [62]. The material exhibits fast luminescence quenching when soaked in aqueous solution with Fe^{3+} ions. The detection limit was determined to be 6.3×10^{-3} mg/L, which is superior to many other iron sensors. A 3D luminescent uranyl coordination polymer that can recognize Ru^{3+} ions was also found by Weng et al. [232]. Uranyl coordination polymer was also employed for anion detection by Wang et al. [233]. A rare case of uranyl coordination polymer was found to be highly selective toward MnO_4^- with a K_{sv} value of 1.88×10^4. The detection limit of MnO_4^- in water was determined to be 1.79×10^{-6} mol/L. Most recently, Li et al. reported a rare case of luminescent cationic thorium-organic framework that exhibited a marked luminescence signal change when the material was immersed in various solutions [59]. The significant luminescence change is caused by the crystal structure evolution when contacting different solutions. The material was successfully introduced for IO_3^- anion detection with high sensitivity and selectivity. These works offer an alternative approach for the fabrication of heavy metal luminescent probes. In addition, organic molecules are also intractable pollutants that may be found in natural waster systems. Fast and accurate detection of various organic contaminants is critical. The utilization of actinides containing uranyl based luminescent organic frameworks for various organic molecules has been reported by several researchers in China. These organic molecules are vary from explosive matter to antibiotic compounds such as tetracycline [234], nitrobenzene [235], arginine and so forth [233]. Zheng et al. has performed several works in terms of organic molecule detection. These uranyl containing organic frameworks show some advantages in regard to the detection sensitivity and selectivity. Actually, employing uranyl or other actinide elements as activators or metal nodes in coordination polymers for realizing heavy metal or organic molecule detection is in its infancy, large amounts of materials are visible.

3.2.3 Conducting and semiconducting materials

The oxo atoms of uranyl are considered to be chemically inert in most cases. However, Raymond et al. noted that these oxygen atoms act more than blocked coordination sites but efficient hydrogen bond acceptors [236]. The intermolecular or intramolecular hydrogen bond interactions between uranyl oxo atoms and hydrogen bond donors from ligands may significantly facilitate selective complexation to uranyl [237]. Additionally, the dioxo atoms have also been proven to have intrinsic Lewis base character which could bind to the Lewis acid center, as described with cation-cation interactions (CCIs). This distinct coordination geometry is often found in uranyl containing bimetallic compounds [3, 238–240], and has been thoroughly revealed through X-ray diffraction. However, these distinctive coordination behaviors have rarely been considered for building functional materials. In 2019, Gui et al. reported a uranyl-bearing coordination polymer (**HUP-1**), that could be used with excellent proton conductivity, which is close to that of the commercial conduction material Nafion [22]. **HUP-1** could be overall described as a layer packed structure with a dense 2D hydrogen bond network loaded in the interlayer space. The uranyl oxo atoms are involved in the composition of the hydron bond network by forming a series of $U{=}O\cdots H_3O^+$ CCI bonds. Another characteristic of the hydrogen bonds is that each H_3O^+ cation is bonded by four symmetry-related H_3O^+ cations with distances ranging from 3.053 to 3.126 Å, which is expected to have a strong repulsion effect. Nevertheless, due to the existence of the $U{=}O\cdots H_3O^+$ CCI bonds, the repulsion between these hydronium cations is effectively compensated. This endows the material with an efficient proton transfer capacity.

When the temperature and humidity were elevated to 98 °C and 98% RH, respectively, the superprotonic conductivity of **HUP-1** reached the highest level of 10^{-1} S cm^{-1}. SCXRD and PXRD analysis revealed that the structure of **HUP-1** could be transformed into another centrosymmetric crystal (**HUP-2**) with a very similar structure under this condition. The *in-situ* generated H_3PO_4 in the interlayer of **HUP-2** (termed as **H_3PO_4@HUP-2**) greatly facilitates proton transportation. Comparatively, the generated H_3PO_4 is thoroughly ordered mixing within the structure which provides more efficient conducting performance, as proven by comparision with the conduction of the H_3PO_4 + **HUP-2** mixture. These results indicate that the dioxo atoms from the axial of uranyl may serve as efficient hydrogen bond acceptors. The resulting dense and rigid hydrogen bond network could significantly facilitate the proton conductivity, and hence provide a general strategy for building proton conducting materials. Proton conduction could also be achieved in uranyl-organic framework as demonstrated by Liu et al. [241]. In contrast to **HUP-1**, the incorporation of hydrophilic sulfonate groups into the framework boosts the sorption of guest water molecules, and thus leads to high proton conductivity. These works are inspiring because they provide us with new insights into building proton conductors by employing uranyl or other actinides as functionalized moieties.

There are two kinds of semiconductors that are used for X-ray detection, including elemental semiconductors (e.g. Si, Ge) and compound semiconductors (GaAs, CdTe). In this section, we introduce uranium into compound semiconductive materials for the fabrication of direct X-ray detectors. Recently, Cheng et al. presented distinct approach to obtain efficient electron transport pathway by taking advantage of cage-to-cage interactions in a uranium organic cage (SCU-14), which lead to a promising X-ray-to-current conversion efficiency [68]. The SCU-14 crystals could be obtained through a mild solvothermal reaction. SCU-14 is assembled from polycatenation of isolated uranyl-organic cages, which contain four uranyl cation and six ligands. Uranyl plays a fundamental role in the formation of the M_4L_6 (Figure 3b) with unique configuration. The topology structure clearly demonstrates that each adamantane-shaped octahedron cage is interlocked by six identical adjacent ones through mechanical bond. A long-range π–π stacking chain is found in the interlocked skeleton, which provides an efficient electron transport pathway. The band gap of SCU-14 was determined to be 2.61 eV, a suitable value for radiation detection. Herein, combined with the high Z (atomic number) value of uranium, two important features of an ideal radiation detector are in position, including the efficient carrier transport pathway and the high attenuation efficiency. The calculated attenuation efficiency is much better than that of our recently developed Tb based MOF detector and commercial materials such as α-Se and Si, and is even close to the state-of-the-art detector CdZnTe. This confirms the above speculation that SCU-14 may potentially be used for X-ray detection. The charge-carrier mobility lifetime product ($\mu\tau$) of SCU-14 is evaluated to be 6.30×10^{-4} cm^2 V^{-1}, which is higher than those of SCU-14 and some newly developed perovskites [242–244]. A record detection sensitivity value of 54.93 μC Gy_{air}^{-1} cm^{-2} was found among reported MOF/MOC-based X-ray detectors at that time. These findings indicate that uranium may serve as a suitable metal center for building functional MOCs as well as photovoltaic materials. Another strategy for building uranium compound semiconductive X-ray detectors was recently developed by Zhang et al. [33]. In this work, we disclose the semiconductive behavior in a large mixed-valent uranium cluster $[H_3O^+](U^V[U^{VI}O_2]_8[\mu_3\text{–}O]_6[PhCOO]_2[Py(CH_2O)_2]_4[DMF]_4)$ (Compound 2) for the first time. The structure of compound 2 is composed of nine uranium centers which surrounded by $Py(CH_2O^-)_2$ and benzoic acid ligands. The most interesting finding comes from the U(V) metal center located at the center of the structure, which encompassed by other eight uranyl(VI) groups. In consideration of the unique structural trait and mixed-valent nature, distinct electronic structure is in visible. The semiconducting nature of compound 2 was firstly realized through its wide absorption spectrum (band gap = 1.96 eV). Density functional theory (DFT) analysis was initially employed in this study for a better understanding of the electronic structure and semiconductive nature. The energy gap structure of compound 2 indicates a similar band gap between calculated value (1.83 eV) and experimental value (1.96 eV). The incorporation of large amounts of uranium metal center into compound 2 may directly result in a large density (ρ) and high effective atomic number (Z_{eff}), which benefits high energy photon absorption. As speculated, the largest Z_{eff} among all the radiation detection semiconductors at that time. On the other hand, compound 2 also exhibits high X-ray mass attenuation coefficient compared with commercially available radiation detection materials and recently reported perovskites. The resistivity of the materials is calculated to be 2.3×10^{11} Ω�cm and is comparable with that of SCU-12 and commercial radiation semiconductors. The curve of photocurrent *versus* dose rate was established from 1–8 μGyS^{-1}, and it gives a sensitivity of 23.04 μC Gy^{-1} cm^{-2} at 30 V bias voltages. This value is close to commercial α-Se detector [245]. These works suggest that uranium or other actinide based semiconductors may be endowed with distinct semiconductive capabilities that traditional materials cannot be achieved.

3.3 Catalysis and activation of small molecules

3.3.1 Catalysis

The uranyl cation has proven to be an effective photoredox catalyst in visible-light-driven synthetic chemistry, which possesses a long fluorescence lifetime and high oxidizing ability in the excited state $[{}^*UO_2^{2+}]$ [246]. Two major mechanisms, single-electron transfer and hydrogen-atom transfer, have been observed in uranyl-catalyzed photoredox transformations. In 2019, Li et al. reported an effective method for the late-stage oxygenation of sulfur-containing molecules by ground-state oxygen and uranyl cations (UO_2^{2+}) as the active photocatalyst (Scheme 13a) [247]. Up to 32 sulfone and sulfoxide derivatives were synthesized in an atom- and step-efficient manner under ambient conditions. The generation of an intermediate with a UV center and an oxygen radical via a ligand-to-metal charge transfer process was critical for this reaction. Further study revealed that the interaction between this intermediate and the additives/solvents was important in adjusting the photoactivity.

Recently, Zhou et al. reported an example of uranyl-photocatalyzed hydrolysis of diaryl ethers at room temperature under blue light stimulation (Scheme 13b) [248]. Both symmetrical and unsymmetrical diaryl ethers were compatible in this reaction. C–O bond cleavage was achieved via a single-electron transfer process between the substrates and excited uranyl cations. Further ^{18}O-labeling experiments confirmed that the oxygen source was H_2O. This study exhibits the potential application of uranyl photocatalysts in the degradation of lignin.

In addition, uranyl photoredox-catalyzed oxygen atom transfer was recently reported by Hu et al. [249]. A series of phenols were synthesized by the C–N bond activation of anilines under mild conditions (Scheme 13c). Both ^{18}O and ^{15}N labeling experiments clearly indicate that the O came from H_2O and that the amino group was left as ammonium. This reaction also involves the single electron transfer process between the uranyl catalyst and the protonated aniline. Further study exhibits a hundredfold efficiency of this reaction when conducted by flow reaction.

An example of a uranyl-catalyzed 1,6-Machiel addition reaction between *p*-quinone methides and alcohol/thiol was reported by Yu et al. in 2020 (Scheme 13d) [250]. This reaction has a broad substrate scope and good functional group compatibility, and thus, a series of diarylmethane derivatives were synthesized in good yield. Later, Yu et al. found that under blue-light irradiation, uranyl could be

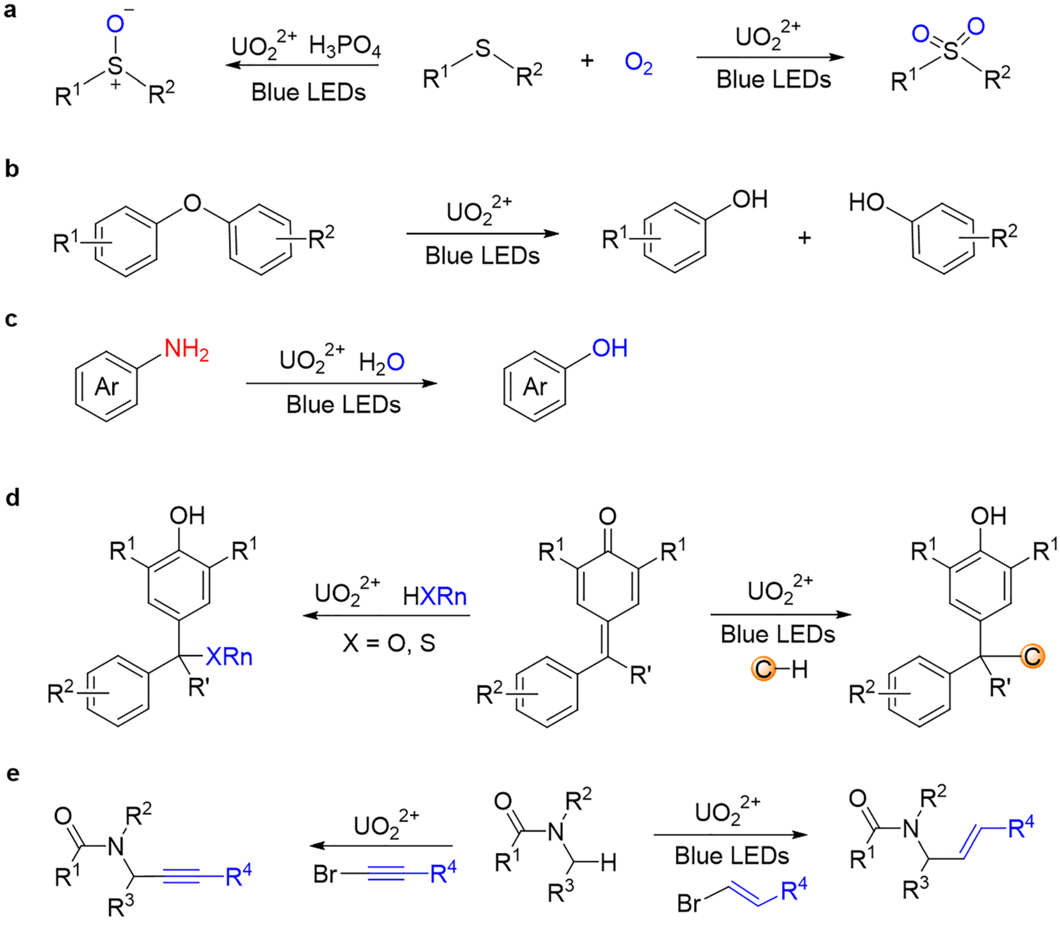

Scheme 13: Catalytic examples by actinide species. a. Reproduced with permission [247]. Copyright 2019, Wiley-VCH; b. Reproduced with permission [248]. Copyright 2021, American Chemical Society. c. Reproduced with permission [249] Copyright 2021, Oxford University Press. d. Reproduced with permission [250]. Copyright 2020, Elsevier; Reproduced with permission [251]. Copyright 2020, Wiley-VCH. e. Reproduced with permission [252]. Copyright 2020, Royal Society of Chemistry.

used as a photocatalyst to synthesize diverse diarylmethane derivatives via C(sp^3)–H activation and C–C bond formation (Scheme 13d) [251]. Further experiments and DFT calculations suggest that the hydrogen atom transfer process triggers the reaction upon light excitation. These studies highlight the potential of uranyl ions as catalysts/photocatalysts in organic chemistry.

Very recently, a uranyl-catalyzed alkynylation and olefination of amides was reported by the Mao et al. (Scheme 13e) [252]. A series of carbon-centered radicals were generated via a hydrogen atom transfer process, which could react with alkynyl and alkenyl bromides via cross-coupling reactions. Mechanistic studies and crystallographic analysis suggested that uranyl peroxide was an important intermediate in this process. This study reveals that the ligands could regulate the activity of the uranyl photocatalyst.

3.3.2 Activation of small molecules

Haber noted that uranium materials were effective catalysts for the synthesis of ammonia in an early patent [253]. However, examples of N_2 activation and cleavage by molecular uranium complexes are rare. In 2020, Xin et al. reported an example of N_2 cleaved by a heterometallic U–Rh cluster under the reduction of KC_8 (Scheme 14a) [254]. The product could further react with acid to form ammonium. The ^{15}N-labeling experiments confirmed that the two nitride atoms in complex 102 come from N_2. The U and Rh synergistic effect in the process of N_2 cleavage was further confirmed by DFT calculations. This study suggests that heterometallic complexes with U–M bonds can be used as an efficient platform for N_2 activation and conversion.

In addition to the U–M synergistic activation of N_2, a U–P synergistic strategy was also developed by the Wang et al. for the activation of N_2 and O_2 (Scheme 14b) [255]. They found that U(III)–P(III) complex 103 could react with N_2 via a 6e reduction, leading to the formation of final product 104. In this process, the two electrons derived from 1e oxidation of the two U(III) centers and the other four electrons come from formal 2e oxidation of the two P(III). Therefore, the synergism of U(III) and P(III) is critical for the 6e full reduction of N_2. In addition, the U(III)–P(III) synergistic strategy can also be used to activate two molecules of O_2 via an 8e reduction, leading to the formation of complex 105 (Scheme 14b). This study suggests that the synergism between uranium and a low-valent element is a promising strategy for small molecule activation.

Although a series of uranium-mediated activations of N_2 have been reported, examples of the activation of heavier congeners are extremely rare. Recently, Fang et al. found that the U(III)–P(III) synergistic strategy could be

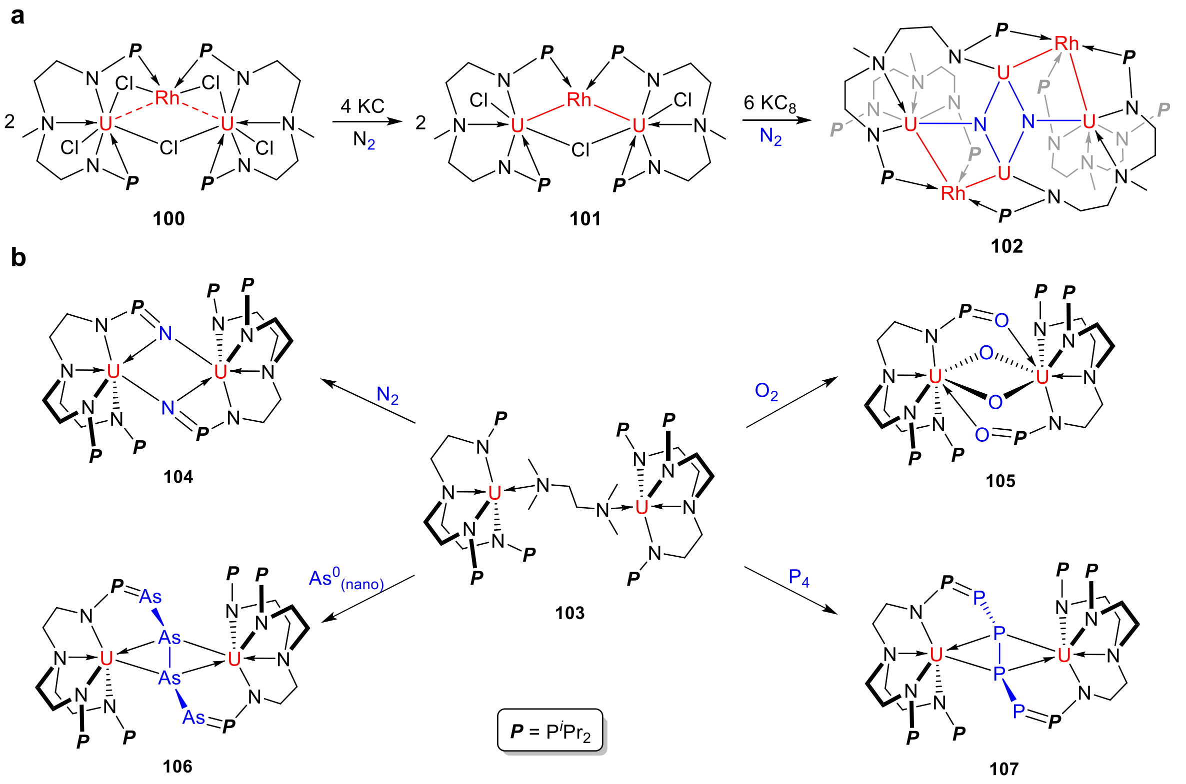

Scheme 14: Small molecule activation by actinide species. **a.** Reproduced with permission [254]. Copyright 2019, Wiley-VCH. **b.** Reproduced with permission [255]. Copyright 2021, American Chemical Society.

extended to the activation of P_4 and elemental arsenic [256]. As shown in Scheme 14b, uranium polyarsenide complex 106 with a Z-type As_4 unit was generated by the reaction of complex 103 with elemental arsenic. For comparison, the uranium polyphosphide nanochain with an E-type P4 unit was formed by the 6e-reduction of P_4. The synergistic effect between U(III) and P(III) is crucial, as confirmed by DFT calculations.

4 Outlook

Although actinide solid state chemistry research in China has been developed rapidly in recent years and has made remarkable progress, the field is still immature. Therefore, further exploration is needed in the following directions:

(i) **More attention should be given to the research on the solid state chemistry of transuranic elements, which is quite scarce in China**. Since there are only a few specially designed laboratories in China that are qualified to handle transuranium elements, the understanding of the solid-state chemistry of actinides is still mainly limited to thorium and uranium. In particular, research on transuranic organometallic chemistry still remains to be blank in China.

(ii) **There is lack of synchrotron radiation facilities for the characterization of actinide elements, especially transuranic elements in China**. Utilizing advanced characterization techniques to reveal the formation mechanism of actinide compounds and the bonding properties of actinides is helpful to deepen the understanding of the physicochemical properties of actinides.

(iii) **The functionalization of actinide compounds is mainly based on the scintillation phenomenon of uranium, and there are few explorations on the functionalization of other types of actinium compounds**. Intrinsic radioactivity endows actinides with unique properties. Using radioactivity to develop radiation-induced functional materials will greatly broaden the functionalization of actinides.

Author contributions: All the authors have accepted responsibility for the entire content of this submitted manuscript and approved submission.

Research funding: We are grateful for funding support from the National Natural Science Foundation of China (21825601, 21790374), and the Natural Science Foundation of Jiangsu Province (BK20211546).

Conflict of interest statement: The authors declare no conflicts of interest regarding this article.

References

1. International Atomic Energy Agency. *Energy, Electricity and Nuclear Power Estimates for the Period up to 2050*; IAEA: Vienna, 2021.
2. Runde W. Geochemical interactions of actinides in the environment. In *Geochemistry of Soil Radionuclides*; Soil Science Society of America: Madison, 2002; pp. 21–44.
3. Arnold P. L., Cowie B. E., Suvova M., Zegke M., Magnani N., Colineau E., Griveau J.-C., Caciuffo R., Love J. B. Axially symmetric U–O–Ln– and U–O–U-Containing molecules from the control of uranyl reduction with simple f-block halides. *Angew. Chem. Int. Ed.* 2017, *56*, 10775–10779.
4. Chen C.-S., Lee S.-F., Lii K.-H. K(UO Si_2O_6: a pentavalent–uranium silicate. *J. Am. Chem. Soc.* 2005, *127*, 12208–12209.
5. Lin C.-H., Chen C.-S., Shiryaev A. A., Zubavichus Y. V., Lii K.-H. $K_3(U_3O_6)(Si_2O_7)$ and $Rb_3(U_3O_6)(Ge_2O_7)$: a pentavalent-uranium silicate and germanate. *Inorg. Chem.* 2008, *47*, 4445–4447.
6. Liu H.-K., Chang W.-J., Lii K.-H. High-temperature, high-pressure hydrothermal synthesis and characterization of an open-framework uranyl silicate with nine-ring channels: $Cs_2UO_2Si_{10}O_{22}$. *Inorg. Chem.* 2011, *50*, 11773–11776.
7. Chen C.-S., Kao H.-M., Lii K.-H. $K_5(UO_2)_2[Si_4O_{12}(OH)]$: a uranyl silicate containing chains of four silicate tetrahedra linked by SiO…HOSi hydrogen bonds. *Inorg. Chem.* 2005, *44*, 935–940.
8. Chen C.-S., Chiang R.-K., Kao H.-M., Lii K.-H. High-temperature, high-pressure hydrothermal synthesis, crystal structure, and solid-state NMR spectroscopy of $Cs_2(UO_2)(Si_2O_6)$ and variable-temperature powder X-ray diffraction study of the hydrate phase $Cs_2(UO_2)(Si_2O_6)\cdot 0.5H_2O$. *Inorg. Chem.* 2005, *44*, 3914–3918.
9. Lin C.-H., Chiang R.-K., Lii K.-H. Synthesis of thermally stable extra-large pore crystalline materials: a uranyl germanate with 12-ring channels. *J. Am. Chem. Soc.* 2009, *131*, 2068–2069.
10. Liu H.-K., Lii K.-H. $Cs_2USi_6O_{15}$: a tetravalent uranium silicate. *Inorg. Chem.* 2011, *50*, 5870–5872.
11. Lai Y.-H., Chang Y.-C., Wong T.-F., Tai W.-J., Chang W.-J., Lii K.-H. High-temperature, high-pressure hydrothermal synthesis, crystal structures, and spectroscopic studies of a uranium(IV) phosphate ($Na_{10}U_2P_6O_{24}$) and the isotypic cerium(IV) phosphate ($Na_{10}Ce_2P_6O_{24}$). *Inorg. Chem.* 2013, *52*, 13639–13643.
12. Lee C.-S., Wang S.-L., Lii K.-H. $Cs_2K(UO)_2Si_4O_{12}$: a mixed-valence uranium(IV, V) silicate. *J. Am. Chem. Soc.* 2009, *131*, 15116–15117.
13. Nguyen Q. B., Liu H.-K., Chang W.-J., Lii K.-H. $Cs_8U^{IV}(U^{VI}O_2)_3(Ge_3O_9)_3\cdot 3H_2O$: a mixed-valence uranium germanate with 9-ring channels. *Inorg. Chem.* 2011, *50*, 4241–4243.
14. Chang Y.-C., Chang W.-J., Boudin S., Lii K.-H. High-temperature, high-pressure hydrothermal synthesis and characterization of a salt-inclusion mixed-valence uranium(V, VI) silicate: $[Na_9F_2]$ $[(U^VO_2)(U^{VI}O_2)_2(Si_2O_7)_2]$. *Inorg. Chem.* 2013, *52*, 7230–7235.
15. Lin C.-H., Lii K.-H. $A_3(U_2O_4)(Ge_2O_7)$ (A=Rb, Cs): mixed-valence uranium(V, VI) germanates. *Angew. Chem. Int. Ed.* 2008, *47*, 8711–8713.

16. Lee C.-S., Lin C.-H., Wang S.-L., Lii K.-H. $[Na_7U^{IV}O_2(U^VO)_2(U^V/^{VI}O_2)_2Si_4O_{16}]$: a mixed-valence uranium silicate. *Angew. Chem. Int. Ed.* 2010, *49*, 4254–4256.
17. Liu H.-K., Ramachandran E., Chen Y.-H., Chang W.-J., Lii K.-H. High-temperature, high-pressure hydrothermal synthesis, characterization, and structural relationships of layered uranyl arsenates. *Inorg. Chem.* 2014, *53*, 9065–9072.
18. Liu H.-K., Lii K.-H. Mixed-valence uranium(V, VI) and uranyl oxyhydroxides synthesized under high-temperature, high-pressure hydrothermal conditions: $Na_5[U_5O_{16}(OH)_2]$ and $Na_5[U_5O_{17}(OH)]$. *Inorg. Chem.* 2013, *52*, 9172–9174.
19. Xu X., Liu Z., Yang S., Chen L., Diwu J., Alekseev E. V., Chai Z., Albrecht-Schmitt T. E., Wang S. Potassium uranyl borate 3D framework compound resulted from temperature directed hydroborate condensation: structure, spectroscopy, and dissolution studies. *Dalton Trans.* 2016, *45*, 15464–15472.
20. Wang Y., Duan T., Weng Z., Ling J., Yin X., Chen L., Sheng D., Diwu J., Chai Z., Liu N., Wang S. Mild periodic acid flux and hydrothermal methods for the synthesis of crystalline f-element-bearing iodate compounds. *Inorg. Chem.* 2017, *56*, 13041–13050.
21. Gui D., Zheng T., Chen L., Wang Y., Li Y., Sheng D., Diwu J., Chai Z., Albrecht-Schmitt T. E., Wang S. Hydrolytically stable nanoporous thorium mixed phosphite and pyrophosphate framework generated from redox-active ionothermal reactions. *Inorg. Chem.* 2016, *55*, 3721–3723.
22. Daxiang G., Duan W., Shu J., Zhai F., Wang N., Wang X., Li H., Chen L., Diwu J., Chai Z., Wang S. Persistent superprotonic conductivity in the order of 10^{-1} $S{\cdot}cm^{-1}$ achieved through thermally induced structural transformation of a uranyl coordination polymer. *CCS Chem.* 2019, *1*, 197–206.
23. Zhao Y., Wang C., Su J., Wang Y., Wang Y., Wang S., Diwu J., Liu Z. Insights into the new Th (IV) sulfate fluoride complex: synthesis, crystal structures, and temperature dependent spectroscopic properties. *Spectrochim. Acta Mol. Biomol. Spectrosc.* 2015, *149*, 295–303.
24. Wang Y., Zhang L., Chen L., Li W., Dai X., Diwu J., Wang J., Chai Z., Wang S. $Th(H_2O)(I^VO_3)_2[I^{VII}{}_{0.6}{}^{V}{}_{1.76}O_7(OH)]$: a mixed-valent iodine compound containing periodate stabilized by crystallographically compatible lattice sites. *Inorg. Chem.* 2016, *55*, 12101–12104.
25. Lin J., Qie M., Zhang L., Wang X., Lin Y., Liu W., Bao H., Wang J. Probing the influence of acidity and temperature to Th(IV) on hydrolysis, nucleation, and structural topology. *Inorg. Chem.* 2017, *56*, 14198–14205.
26. Lin J., Bao H., Qie M., Silver M. A., Yue Z., Li X., Zhu L., Wang X., Zhang L., Wang J.-Q. Immobilization of alkali metal fluorides via recrystallization in a cationic lamellar material, $[Th(MoO_4)(H_2O)_4Cl]Cl{\cdot}H_2O$. *Inorg. Chem.* 2018, *57*, 6778–6782.
27. Wang Y., Yin X., Zhao Y., Gao Y., Chen L., Liu Z., Sheng D., Diwu J., Chai Z., Albrecht-Schmitt T. E., Wang S. Insertion of trivalent lanthanides into uranyl vanadate layers and frameworks. *Inorg. Chem.* 2015, *54*, 8449–8455.
28. Gui D., Dai X., Zheng T., Wang X., Silver M. A., Chen L., Zhang C., Diwu J., Zhou R., Chai Z., Wang S. An ultrastable heterobimetallic uranium(IV)/Vanadium(III) solid compound protected by a redox-active phosphite ligand: crystal structure, oxidative dissolution, and first-principles simulation. *Inorg. Chem.* 2018, *57*, 903–907.
29. Lin J., Yue Z., Silver M. A., Qie M., Wang X., Liu W., Lin X., Bao H.-L., Zhang L.-J., Wang S., Wang J.-Q. In situ reduction from uranyl ion into a tetravalent uranium trimer and hexamer featuring ion-exchange properties and the alexandrite effect. *Inorg. Chem.* 2018, *57*, 6753–6761.
30. Wang Y., Wang Y., Dai X., Liu W., Yin X., Chen L., Zhai F., Diwu J., Zhang C., Zhou R., Chai Z., Liu N., Wang S. Inorganic X-ray scintillators based on a previously unnoticed but intrinsically advantageous metal center. *Inorg. Chem.* 2019, *58*, 2807–2812.
31. Lu H., Lin J., Wang Y., Li Z.-J., Guo X., Wang J.-Q., Wang S. Unusual heterometallic cation-cation interactions in uranyl zinc germanates. *Eur. J. Inorg. Chem.* 2020, *2020*, 2182–2185.
32. Wang H.-Y., Zheng X.-Y., Long L.-S., Kong X.-J., Zheng L.-S. Sandwich-type uranyl phosphate–polyoxometalate cluster exhibiting strong luminescence. *Inorg. Chem.* 2021, *60*, 6790–6795.
33. Zhang M., Liang C., Cheng G.-D., Chen J., Wang Y., He L., Cheng L., Gong S., Zhang D., Li J., Hu S.-X., Diwu J., Wu G., Wang Y., Chai Z., Wang S. Intrinsic semiconducting behavior in a large mixed-valent uranium(V/VI) cluster. *Angew. Chem. Int. Ed.* 2021, *60*, 9886–9890.
34. Lu H., Wang X.-Y., Wang Y., Li Z.-J., Diefenbach K., Pan Q.-J., Qian Y., Wang J.-Q., Wang S., Lin J. Visible colorimetric dosimetry of UV and ionizing radiations by a dual-module photochromic nanocluster. *Nat. Commun.* 2021, *12*, 2798.
35. Lu H., Xu M., Zheng Z., Liu Q., Qian J., Zhang Z.-H., He M.-Y., Qian Y., Wang J.-Q., Lin J. Emergence of thorium-based polyoxo clusters as a platform for selective X-ray dosimetry. *Inorg. Chem.* 2021, *60*, 18629–18633.
36. Furukawa H., Cordova Kyle E., O'Keeffe M., Yaghi Omar M. The chemistry and applications of metal-organic frameworks. *Science* 2013, *341*, 1230444.
37. Lv K., Fichter S., Gu M., März J., Schmidt M. An updated status and trends in actinide metal-organic frameworks (An-MOFs): from synthesis to application. *Coord. Chem. Rev.* 2021, *446*, 214011.
38. Martin C. R., Leith G. A., Shustova N. B. Beyond structural motifs: the Frontier of actinide-containing metal–organic frameworks. *Chem. Sci.* 2021, *12*, 7214–7230.
39. Chen W., Yuan H.-M., Wang J.-Y., Liu Z.-Y., Xu J.-J., Yang M., Chen J.-S. Synthesis, structure, and photoelectronic effects of a Uranium–Zinc–Organic coordination polymer containing infinite metal oxide sheets. *J. Am. Chem. Soc.* 2003, *125*, 9266–9267.
40. Yu Z.-T., Liao Z.-L., Jiang Y.-S., Li G.-H., Chen J.-S. Water-insoluble Ag–U–organic assemblies with photocatalytic activity. *Chem. Eur J.* 2005, *11*, 2642–2650.
41. Ji C., Li J., Li Y., Zheng H. A new uranyl(VI) complex of rigid V-shaped carboxylate ligand: synthesis, structure and properties. *Inorg. Chem. Commun.* 2010, *13*, 1340–1342.
42. Liao Z.-L., Li G.-D., Wei X., Yu Y., Chen J.-S. Construction of three-dimensional uranyl–organic frameworks with benzenetricarboxylate ligands. *Eur. J. Inorg. Chem.* 2010, *2010*, 3780–3788.
43. Yu T., Qian Z.-h., Li L., Wu X.-l., He H., Qiao Y.-b., Ye G.-a. Synthesis of luminescent thorium-based metal–organic frameworks with 1,2,4,5-tetrakis(4-carboxyphenyl)benzene. *RSC Adv.* 2021, *11*, 17431–17436.
44. Li Y., Weng Z., Wang Y., Chen L., Sheng D., Diwu J., Chai Z., Albrecht-Schmitt T. E., Wang S. Surprising coordination for low-

valent actinides resembling uranyl(vi) in thorium(iv) organic hybrid layered and framework structures based on a graphene-like (6, 3) sheet topology. *Dalton Trans.* 2016, *45*, 918–921.

45. Wang Y., Liu W., Bai Z., Zheng T., Silver M. A., Li Y., Wang Y., Wang X., Diwu J., Chai Z., Wang S. Employing an unsaturated Th^{4+} site in a porous thorium–organic framework for Kr/Xe uptake and separation. *Angew. Chem. Int. Ed.* 2018, *57*, 5783–5787.
46. Li Y., Yang Z., Wang Y., Bai Z., Zheng T., Dai X., Liu S., Gui D., Liu W., Chen M., Chen L., Diwu J., Zhu L., Zhou R., Chai Z., Albrecht-Schmitt T. E., Wang S. A mesoporous cationic thorium-organic framework that rapidly traps anionic persistent organic pollutants. *Nat. Commun.* 2017, *8*, 1354.
47. Huang Z.-w., Hu K.-q., Mei L., Kong X.-h., Yu J.-p., Liu K., Zeng L.-w., Chai Z.-F., Shi W.-Q. A mixed-ligand strategy regulates thorium-based MOFs. *Dalton Trans.* 2020, *49*, 983–987.
48. Geng J.-s., Liu K., Liang Y.-y., Yu J.-p., Hu K.-q., Yuan L.-H., Feng W., Chai Z.-f., Mei L., Shi W.-q. An azobenzene-modified photoresponsive thorium–organic framework: monitoring and quantitative analysis of reversible trans–cis photoisomerization. *Inorg. Chem.* 2021, *60*, 8519–8529.
49. Xu Z., Xiong X., Xiong J., Krishna R., Li L., Fan Y., Luo F., Chen B. A robust Th-azole framework for highly efficient purification of C_2H_4 from a $C_2H_4/C_2H_2/C_2H_6$ mixture. *Nat. Commun.* 2020, *11*, 3163.
50. Gao Z., Lai Y., Tao Y., Xiao L., Zhang L., Luo F. Constructing well-defined and robust Th-MOF-supported single-site copper for production and storage of ammonia from electroreduction of nitrate. *ACS Cent. Sci.* 2021, *7*, 1066–1072.
51. Feng H., Xiong X., Gong L., Zhang H., Xu Y., Feng X., Luo F. Rational tuning of thorium-organic frameworks by reticular chemistry for boosting radionuclide sequestration. *Nano Res.* 2022, *15*, 1472–1478.
52. Wu Y.-B., Xiong C., Liu Q.-Y., Ma J.-G., Luo F., Wang Y.-L. Structural evolution from noninterpenetrated to interpenetrated thorium–organic frameworks exhibiting high propyne storage. *Inorg. Chem.* 2021, *60*, 6472–6479.
53. Li Z.-J., Ju Y., Yu B., Wu X., Lu H., Li Y., Zhou J., Guo X., Zhang Z.-H., Lin J., Wang J.-Q., Wang S. Modulated synthesis and isoreticular expansion of Th-MOFs with record high pore volume and surface area for iodine adsorption. *Chem. Commun.* 2020, *56*, 6715–6718.
54. Li Z.-J., Ju Y., Lu H., Wu X., Yu X., Li Y., Wu X., Zhang Z.-H., Lin J., Qian Y., He M.-Y., Wang J.-Q. Cover feature: boosting the iodine adsorption and radioresistance of Th–UiO–66 MOFs via aromatic substitution (Chem. Eur. J. 4/2021). *Chem. Eur J.* 2021, *27*, 1162.
55. Li Z.-J., Yue Z., Ju Y., Wu X., Ren Y., Wang S., Li Y., Zhang Z.-H., Guo X., Lin J., Wang J.-Q. Ultrastable thorium metal–organic frameworks for efficient iodine adsorption. *Inorg. Chem.* 2020, *59*, 4435–4442.
56. Ju Y., Li Z.-J., Lu H., Zhou Z., Li Y., Wu X.-L., Guo X., Qian Y., Zhang Z.-H., Lin J., Wang J.-Q., He M.-Y. Interpenetration control in thorium metal–organic frameworks: structural complexity toward iodine adsorption. *Inorg. Chem.* 2021, *60*, 5617–5626.
57. Li Z.-J., Guo S., Lu H., Xu Y., Yue Z., Weng L., Guo X., Lin J., Wang J.-Q. Unexpected structural complexity of thorium coordination polymers and polyoxo cluster built from simple formate ligands. *Inorg. Chem. Front.* 2020, *7*, 260–269.
58. Li Z.-J., Ju Y., Zhang Z., Lu H., Li Y., Zhang N., Du X.-L., Guo X., Zhang Z.-H., Qian Y., He M.-Y., Wang J.-Q., Lin J. Unveiling the unique roles of metal coordination and modulator in the polymorphism control of metal-organic frameworks. *Chem. Eur J.* 2021, *27*, 17586–17594.
59. Li Z.-J., Lei M., Bao H., Ju Y., Lu H., Li Y., Zhang Z.-H., Guo X., Qian Y., He M.-Y., Wang J.-Q., Liu W., Lin J. A cationic thorium–organic framework with triple single-crystal-to-single-crystal transformation peculiarities for ultrasensitive anion recognition. *Chem. Sci.* 2021, *12*, 15833–15842.
60. Xu H., Cao C.-S., Hu H.-S., Wang S.-B., Liu J.-C., Cheng P., Kaltsoyannis N., Li J., Zhao B. High uptake of ReO_4^- and CO_2 conversion by a radiation-resistant thorium–nickle $[Th_{48}Ni_6]$ nanocage-based metal–organic framework. *Angew. Chem. Int. Ed.* 2019, *58*, 6022–6027.
61. Denning R. G. Electronic structure and bonding in actinyl ions and their analogs. *J. Phys. Chem.* 2007, *111*, 4125–4143.
62. Liu W., Xie J., Zhang L., Silver M. A., Wang S. A hydrolytically stable uranyl organic framework for highly sensitive and selective detection of Fe^{3+} in aqueous media. *Dalton Trans.* 2018, *47*, 649–653.
63. Hu F., Di Z., Lin P., Huang P., Wu M., Jiang F., Hong M. An anionic uranium-based metal–organic framework with ultralarge nanocages for selective dye adsorption. *Cryst. Growth Des.* 2018, *18*, 576–580.
64. Kong X., Hu K., Mei L., Wu Q., Huang Z., Liu K., Chai Z., Nie C., Shi W. Construction of hybrid bimetallic uranyl compounds based on a preassembled terpyridine metalloligand. *Chem. Eur J.* 2021, *27*, 2124–2130.
65. Li H.-H., Zeng X.-H., Wu H.-Y., Jie X., Zheng S.-T., Chen Z.-R. Incorporating guest molecules into honeycomb structures constructed from uranium(VI)–polycarboxylates: structural diversities and photocatalytic activities for the degradation of organic dye. *Cryst. Growth Des.* 2015, *15*, 10–13.
66. Chen F., Wang C.-z., Li Z.-j., Lan J.-h., Ji Y.-q., Chai Z.-f. New three-fold interpenetrated uranyl organic framework constructed by terephthalic acid and imidazole derivative. *Inorg. Chem.* 2015, *54*, 3829–3834.
67. Wang Y., Liu Z., Li Y., Bai Z., Liu W., Wang Y., Xu X., Xiao C., Sheng D., Diwu J., Su J., Chai Z., Albrecht-Schmitt T. E., Wang S. Umbellate distortions of the uranyl coordination environment result in a stable and porous polycatenated framework that can effectively remove cesium from aqueous solutions. *J. Am. Chem. Soc.* 2015, *137*, 6144–6147.
68. Cheng L., Liang C., Liu W., Wang Y., Chen B., Zhang H., Wang Y., Chai Z., Wang S. Three-dimensional polycatenation of a uranium-based metal–organic cage: structural complexity and radiation detection. *J. Am. Chem. Soc.* 2020, *142*, 16218–16222.
69. Liu C., Chen F.-Y., Tian H.-R., Ai J., Yang W., Pan Q.-J., Sun Z.-M. Interpenetrated uranyl–organic frameworks with bor and pts topology: structure, spectroscopy, and computation. *Inorg. Chem.* 2017, *56*, 14147–14156.
70. Ai J., Chen F.-Y., Gao C.-Y., Tian H.-R., Pan Q.-J., Sun Z.-M. Porous anionic uranyl–organic networks for highly efficient Cs^+ adsorption and investigation of the mechanism. *Inorg. Chem.* 2018, *57*, 4419–4426.
71. Wang Y., Li Y., Bai Z., Xiao C., Liu Z., Liu W., Chen L., He W., Diwu J., Chai Z., Albrecht-Schmitt T. E., Wang S. Design and synthesis of a chiral uranium-based microporous metal organic

framework with high SHG efficiency and sequestration potential for low-valent actinides. *Dalton Trans.* 2015, *44*, 18810–18814.

72. Wang Y., Yin X., Liu W., Xie J., Chen J., Silver M. A., Sheng D., Chen L., Diwu J., Liu N., Chai Z., Albrecht-Schmitt T. E., Wang S. Emergence of uranium as a distinct metal center for building intrinsic X-ray scintillators. *Angew. Chem. Int. Ed.* 2018, *57*, 7883–7887.
73. Pang Z. h., Luo F. A highly rare 3D U–Cu metal-organic framework showing three-connected srs topology and nine-fold interpenetration. *Inorg. Chem. Commun.* 2020, *119*, 108041.
74. Huang Z.-W., Hu K.-Q., Mei L., Wang C.-Z., Chen Y.-M., Wu W.-S., Chai Z.-F., Shi W.-Q. Potassium ions induced framework interpenetration for enhancing the stability of uranium-based porphyrin MOF with visible-light-driven photocatalytic activity. *Inorg. Chem.* 2021, *60*, 651–659.
75. Yang W., Dang S., Wang H., Tian T., Pan Q.-J., Sun Z.-M. Synthesis, structures, and properties of uranyl hybrids constructed by a variety of mono- and polycarboxylic acids. *Inorg. Chem.* 2013, *52*, 12394–12402.
76. Bai Z., Wang Y., Li Y., Liu W., Chen L., Sheng D., Diwu J., Chai Z., Albrecht-Schmitt T. E., Wang S. First cationic uranyl–organic framework with anion-exchange capabilities. *Inorg. Chem.* 2016, *55*, 6358–6360.
77. Yang W., Tian W.-G., Liu X.-X., Wang L., Sun Z.-M. Syntheses, structures, luminescence, and photocatalytic properties of a series of uranyl coordination polymers. *Cryst. Growth Des.* 2014, *14*, 5904–5911.
78. Hu K.-Q., Zhu L.-Z., Wang C.-Z., Mei L., Liu Y.-H., Gao Z.-Q., Chai Z.-F., Shi W.-Q. Novel uranyl coordination polymers based on quinoline-containing dicarboxylate by altering auxiliary ligands: from 1D chain to 3D framework. *Cryst. Growth Des.* 2016, *16*, 4886–4896.
79. Wu D., Bai X., Tian H.-R., Yang W., Li Z., Huang Q., Du S., Sun Z.-M. Uranyl carboxyphosphonates derived from hydrothermal in situ ligand reaction: syntheses, structures, and computational investigations. *Inorg. Chem.* 2015, *54*, 8617–8624.
80. Zeng L.-W., Hu K.-Q., Mei L., Li F.-Z., Huang Z.-W., An S.-W., Chai Z.-F., Shi W.-Q. Structural diversity of bipyridinium-based uranyl coordination polymers: synthesis, characterization, and ion-exchange application. *Inorg. Chem.* 2019, *58*, 14075–14084.
81. Wang L.-H., Shang R., Zheng Z., Liu C.-L., Wang Z.-M. Two systems of $[DabcoH_2]^{2+}$/$[PipH_2]^{2+}$–Uranyl–Oxalate showing reversible crystal-to-crystal transformations controlled by the diammonium/uranyl/oxalate ratios in aqueous solutions ($[DabcoH_2]^{2+}$ = 1,4-Diazabicyclo-[2.2.2]-octaneH_2 and $[PipH_2]^{2+}$ = PiperazineH_2). *Cryst. Growth Des.* 2013, *13*, 2597–2606.
82. Zheng T., Gao Y., Chen L., Liu Z., Diwu J., Chai Z., Albrecht-Schmitt T. E., Wang S. A new chiral uranyl phosphonate framework consisting of achiral building units generated from ionothermal reaction: structure and spectroscopy characterizations. *Dalton Trans.* 2015, *44*, 18158–18166.
83. Mei L., Xu C., Wu Q.-y., Hu K.-q., Yuan L.-y., Chen J., Xiao C.-l., Wang S.-a., Chai Z.-f., Shi W.-q. A neptunium(v)–mediated interwoven transuranium-rotaxane network incorporating a mechanically interlocked [c2]daisy chain unit. *Chem. Commun.* 2018, *54*, 8645–8648.
84. Zhang Y., Li K., Zhang S., Wang X., Zhang H., Wang Y., Wang Y., Chai Z., Wang S. A trivalent americium organic framework with decent structural stability against self-irradiation. *Chin. J. Chem.* 2021, *40*, 801–805.
85. Wang Y., Hu S.-X., Cheng L., Liang C., Yin X., Zhang H., Li A., Sheng D., Diwu J., Wang X. Stabilization of plutonium (V) within a crown ether inclusion complex. *CCS Chem.* 2020, *2*, 425–431.
86. Li K., Hu S., Zou Q., Zhang Y., Zhang H., Zhao Y., Zhou T., Chai Z., Wang Y. Synthesis and characterizations of a plutonium(III) crown ether inclusion complex. *Inorg. Chem.* 2021, *60*, 8984–8989.
87. Krot N. N., Bessonov A. A., Grigor'ev M. S., Charushnikova I. A., Makarenkov V. I. Synthesis of new crystalline Pu(V) compounds from solutions: I. Structure and characteristics of a double Pu(V) phthalate with $[Co(NH_3)_6]^{3+}$ in the outer sphere. *Radiochemistry* 2004, *46*, 560–564.
88. Krot N. N., Bessonov A. A., Grigor'ev M. S., Charushnikova I. A., Makarenkov V. I. Synthesis of new crystalline Pu(V) compounds from solutions: III. Synthesis and study of $NaPuO_2C_2O_4{\cdot}nH_2O$ with $n = 3$, 1, and 0. *Radiochemistry* 2005, *47*, 114–118.
89. Bessonov A. A., Krot N. N., Grigor'ev M. S., Makarenkov V. I. Synthesis of new crystalline Pu(V) compounds from solutions: VII. Synthesis and study of $MPuO_2C_2O_4 \cdot nH_2O$ with $M=NH_4$ and Cs. *Radiochemistry* 2005, *47*, 468–471.
90. Bean A. C., Scott B. L., Albrecht-Schmitt T. E., Runde W. Structural and spectroscopic trends in actinyl iodates of uranium, neptunium, and plutonium. *Inorg. Chem.* 2003, *42*, 5632–5636.
91. Wang S., Villa E. M., Diwu J., Alekseev E. V., Depmeier W., Albrecht-Schmitt T. E. Role of anions and reaction conditions in the preparation of uranium(VI), neptunium(VI), and plutonium(VI) borates. *Inorg. Chem.* 2011, *50*, 2527–2533.
92. Clark D. L., Keogh D. W., Palmer P. D., Scott B. L., Tait C. D. Synthesis and structure of the first transuranium crown ether inclusion complex: $[NpO_2([18]Crown\text{-}6)]ClO_4$. *Angew. Chem. Int. Ed.* 1998, *37*, 164–166.
93. Fang B., Ren W., Hou G., Zi G., Fang D.-C., Maron L., Walter M. D. An actinide metallacyclopropene complex: synthesis, structure, reactivity, and computational studies. *J. Am. Chem. Soc.* 2014, *136*, 17249–17261.
94. Fang B., Zhang L., Hou G., Zi G., Fang D.-C., Walter M. D. C–H bond activation induced by thorium metallacyclopropene complexes: a combined experimental and computational study. *Chem. Sci.* 2015, *6*, 4897–4906.
95. Fang B., Zhang L., Hou G., Zi G., Fang D.-C., Walter M. D. Experimental and computational studies on an actinide metallacyclocumulene complex. *Organometallics* 2015, *34*, 5669–5681.
96. Fang B., Hou G., Zi G., Fang D.-C., Walter M. D. A thorium metallacyclopentadiene complex: a combined experimental and computational study. *Dalton Trans.* 2015, *44*, 7927–7934.
97. Fang B., Hou G., Zi G., Ding W., Walter M. D. Steric and electronic influences of internal alkynes on the formation of thorium metallacycles: a combined experimental and computational study. *Organometallics* 2016, *35*, 1384–1391.
98. Yang P., Zhou E., Fang B., Hou G., Zi G., Walter M. D. Preparation of $(\eta^5\text{-}C_5Me_5)_2Th(bipy)$ and its reactivity toward small molecules. *Organometallics* 2016, *35*, 2129–2139.
99. Ren W., Zi G., WalterSynthesis M. D. Structure, and reactivity of a thorium metallocene containing a 2,2′-bipyridyl ligand. *Organometallics* 2012, *31*, 672–679.
100. Ren W., Song H., Zi G., Walter M. D. A bipyridyl thorium metallocene: synthesis, structure and reactivity. *Dalton Trans.* 2012, *41*, 5965–5973.

101. Ren W., Lukens W. W., Zi G., Maron L., Walter M. D. Is the bipyridyl thorium metallocene a low-valent thorium complex? A combined experimental and computational study. *Chem. Sci.* 2013, *4*, 1168–1174.
102. Zhang L., Hou G., Zi G., Ding W., Walter M. D. Influence of the 5f orbitals on the bonding and reactivity in organoactinides: experimental and computational studies on a uranium metallacyclopropene. *J. Am. Chem. Soc.* 2016, *138*, 5130–5142.
103. Zhang L., Fang B., Hou G., Ai L., Ding W., Walter M. D., Zi G. Intrinsic reactivity of a uranium metallacyclopropene toward unsaturated organic molecules. *Dalton Trans.* 2016, *45*, 16441–16452.
104. Wang D., Ding W., Hou G., Zi G., Walter M. D. Uranium versus thorium: synthesis and reactivity of $[\eta^5\text{-1,2,4-}(Me_3C)_3C_5H_2]_2U$ $[\eta^2\text{-}C_2Ph_2]$. *Chem. Eur J.* 2021, *27*, 6767–6782.
105. Zhang L., Fang B., Hou G., Zi G., Ding W., Walter M. D. Experimental and computational studies of a uranium metallacyclocumulene. *Organometallics* 2017, *36*, 898–910.
106. Zhang L., Hou G., Zi G., Ding W., Walter M. D. Preparation of a uranium metallacyclocumulene and its reactivity towards unsaturated organic molecules. *Dalton Trans.* 2017, *46*, 3716–3728.
107. Zhang L., Zhang C., Hou G., Zi G., Walter M. D. Small-molecule activation mediated by a uranium bipyridyl metallocene. *Organometallics* 2017, *36*, 1179–1187.
108. Yu C., Liang J., Deng C., Lefèvre G., Cantat T., Diaconescu P. L., Huang W. Arene-bridged dithorium complexes: inverse sandwiches supported by a δ bonding interaction. *J. Am. Chem. Soc.* 2020, *142*, 21292–21297.
109. Xiao Y., Zhao X.-K., Wu T., Miller J. T., Hu H.-S., Li J., Huang W., Diaconescu P. L. Distinct electronic structures and bonding interactions in inverse-sandwich samarium and ytterbium biphenyl complexes. *Chem. Sci.* 2021, *12*, 227–238.
110. Liddle S. T. Inverted sandwich arene complexes of uranium. *Coord. Chem. Rev.* 2015, *293–294*, 211–227.
111. Ren W., Deng X., Zi G., Fang D.-C. The Th=C double bond: an experimental and computational study of thorium poly-carbene complexes. *Dalton Trans.* 2011, *40*, 9662–9664.
112. Su W., Pan S., Sun X., Wang S., Zhao L., Frenking G., Zhu C. Double dative bond between divalent carbon(0) and uranium. *Nat. Commun.* 2018, *9*, 4997.
113. Su W., Pan S., Sun X., Zhao L., Frenking G., Zhu C. Cerium–carbon dative interactions supported by carbodiphosphorane. *Dalton Trans.* 2019, *48*, 16108–16114.
114. Fang W., Pan S., Su W., Wang S., Zhao L., Frenking G., Zhu C. Complex featuring two double dative bonds between carbon(0) and uranium. *CCS Chem.* 2021, *4*, 1–20.
115. Su W., Ma Y., Xiang L., Wang J., Wang S., Zhao L., Frenking G., Ye Q. Isolation of a uranium(III)–carbon multiple bond complex. *Chem. Eur J.* 2021, *27*, 10006–10011.
116. Ren W., Zhao N., Chen L., Song H., Zi G. Synthesis, structure, and catalytic activity of an organothorium hydride complex. *Inorg. Chem. Commun.* 2011, *14*, 1838–1841.
117. Qin G., Wang Y., Shi X., Del Rosal I., Maron L., Cheng J. Monomeric thorium dihydrido complexes: versatile precursors to actinide metallacycles. *Chem. Commun.* 2019, *55*, 8560–8563.
118. Chen R., Qin G., Li S., Edwards A. J., Piltz R. O., Del Rosal I., Maron L., Cui D., Cheng J. Molecular thorium trihydrido clusters stabilized by cyclopentadienyl ligands. *Angew. Chem. Int. Ed.* 2020, *59*, 11250–11255.
119. Ren W., Zi G., Fang D.-C., Walter M. D. Thorium oxo and sulfido metallocenes: synthesis, structure, reactivity, and computational studies. *J. Am. Chem. Soc.* 2011, *133*, 13183–13196.
120. Ren W., Zi G., Fang D.-C., Walter M. D. A base-free thorium–terminal-imido metallocene: synthesis, structure, and reactivity. *Chem. Eur J.* 2011, *17*, 12669–12682.
121. Ren W., Zhou E., Fang B., Zi G., Fang D.-C., Walter M. D. Si–H addition followed by C–H bond activation induced by a terminal thorium imido metallocene: a combined experimental and computational study. *Chem. Sci.* 2014, *5*, 3165–3172.
122. Ren W., Zhou E., Fang B., Hou G., Zi G., Fang D.-C., Walter M. D. Experimental and computational studies on the reactivity of a terminal thorium imidometallocene towards organic azides and diazoalkanes. *Angew. Chem. Int. Ed.* 2014, *53*, 11310–11314.
123. Zhou E., Ren W., Hou G., Zi G., Fang D.-C., Walter M. D. Small molecule activation mediated by a thorium terminal imido metallocene. *Organometallics* 2015, *34*, 3637–3647.
124. Zhang C., Yang P., Zhou E., Deng X., Zi G., Walter M. D. Reactivity of a Lewis base supported thorium terminal imido metallocene toward small organic molecules. *Organometallics* 2017, *36*, 4525–4538.
125. Zhang C., Hou G., Zi G., Ding W., Walter M. D. A base-free terminal actinide phosphinidene metallocene: synthesis, structure, reactivity, and computational studies. *J. Am. Chem. Soc.* 2018, *140*, 14511–14525.
126. Wang D., Ding W., Hou G., Zi G., Walter M. D. Experimental and computational studies on a base-free terminal uranium phosphinidene metallocene. *Chem. Eur J.* 2020, *26*, 16888–16899.
127. Zhang C., Hou G., Zi G., Walter M. D. A base-free terminal thorium phosphinidene metallocene and its reactivity toward selected organic molecules. *Dalton Trans.* 2019, *48*, 2377–2387.
128. Zhang C., Wang Y., Hou G., Ding W., Zi G., Walter M. D. Experimental and computational studies on a three-membered diphosphido thorium metallaheterocycle $[\eta^5\text{-1, 3-}(Me_3C)_2C_5H_3]_2Th[\eta^2\text{-}P_2(2,\ 4,\ 6\text{-}iPr_3C_6H_2)_2]$. *Dalton Trans.* 2019, *48*, 6921–6930.
129. Wang Y., Zhang C., Zi G., Ding W., Walter M. D. Preparation of a potassium chloride bridged thorium phosphinidiide complex and its reactivity towards small organic molecules. *New J. Chem.* 2019, *43*, 9527–9539.
130. Wang D., Wang S., Hou G., Zi G., Walter M. D. A Lewis base supported terminal uranium phosphinidene metallocene. *Inorg. Chem.* 2020, *59*, 14549–14563.
131. Wang D., Wang S., Li T., Heng Y., Hou G., Zi G., Walter M. D. Reactivity studies involving a Lewis base supported terminal uranium phosphinidene metallocene $[\eta^5\text{-1, 3-}(Me_3C)_2C_5H_3]_2U(=P\text{-2, 4, 6-}^iPr_3C_6H_2)(OPMe_3)$. *Dalton Trans.* 2021, *50*, 8349–8363.
132. Guo T., Diener M. D., Chai Y., Alford M. J., Haufler R. E., McClure S. M., Ohno T., Weaver J. H., Scuseria G. E., Smalley R. E. Uranium stabilization of C28: a tetravalent fullerene. *Science* 1992, *257*, 1661–1664.
133. Wang D., Hou G., Zi G., Walter M. D. $(\eta^5\text{–}C_5Me_5)2U(=P\text{–2, 4, 6-}tBu_3C_6H_2)(OPMe_3)$ revisited—its intrinsic reactivity toward small organic molecules. *Organometallics* 2020, *39*, 4085–4101.

134. Wang D., Hou G., Zi G., Walter M. D. Influence of the Lewis base Ph_3PO on the reactivity of the uranium phosphinidene $(\eta^5\text{–}C_5Me_5)_2U(=P\text{–}2,\ 4,\ 6\text{-}{}^iPr_3C_6H_2)(OPPh_3)$. *Organometallics* 2021, *40*, 383–396.
135. Wang S., Li T., Heng Y., Hou G., Zi G., Walter M. D. Influence of the 1, 3-Bis(trimethylsilyl)cyclopentadienyl ligand on the reactivity of the uranium phosphinidene $[\eta^5\text{-}1,\ 3\text{-}(Me_3Si)_2C_5H_3]_2U(=P\text{-}2,\ 4,\ 6\text{-}{}^iPr_3C_6H_2)(OPPh_3)$. *Organometallics* 2021, *40*, 2149–2165.
136. Liu K., Yu J.-P., Wu Q.-Y., Tao X.-B., Kong X.-H., Mei L., Hu K.-Q., Yuan L.-Y., Chai Z.-F., Shi W.-Q. Rational design of a tripodal ligand for U(IV): synthesis and characterization of a U–Cl species and insights into its reactivity. *Organometallics* 2020, *39*, 4069–4077.
137. Yu J., Liu K., Wu Q., Li B., Kong X., Hu K., Mei L., Yuan L., Chai Z., Shi W. Facile access to uranium and thorium phosphaethynolate complexes supported by tren: experimental and theoretical study. *Chin. J. Chem.* 2021, *39*, 2125–2131.
138. Yang P., Zhou E., Hou G., Zi G., Ding W., Walter M. D. Experimental and computational studies on the formation of thorium–copper heterobimetallics. *Chem. Eur J.* 2016, *22*, 13845–13849.
139. Graves C. R., Scott B. L., Morris D. E., Kiplinger J. L. Facile access to pentavalent uranium organometallics: one-electron oxidation of uranium(IV) imido complexes with copper(I) salts. *J. Am. Chem. Soc.* 2007, *129*, 11914–11915.
140. Graves C. R., Yang P., Kozimor S. A., Vaughn A. E., Clark D. L., Conradson S. D., Schelter E. J., Scott B. L., Thompson J. D., Hay P. J., Morris D. E., Kiplinger J. L. Organometallic uranium(V)–Imido halide complexes: from synthesis to electronic structure and bonding. *J. Am. Chem. Soc.* 2008, *130*, 5272–5285.
141. Feng G., Zhang M., Shao D., Wang X., Wang S., Maron L., Zhu C. Transition-metal-bridged bimetallic clusters with multiple uranium–metal bonds. *Nat. Chem.* 2019, *11*, 248–253.
142. Pyykkö P., Atsumi M. Molecular single-bond covalent radii for elements 1–118. *Chem. Eur J.* 2009, *15*, 186–197.
143. Feng G., McCabe K. N., Wang S., Maron L., Zhu C. Construction of heterometallic clusters with multiple uranium–metal bonds by using dianionic nitrogen–phosphorus ligands. *Chem. Sci.* 2020, *11*, 7585–7592.
144. Lu E., Wooles A. J., Gregson M., Cobb P. J., Liddle S. T. A very short uranium(IV)–Rhodium(I) bond with net double-dative bonding character. *Angew. Chem.* 2018, *130*, 6697–6701.
145. Chi C., Wang J.-Q., Qu H., Li W.-L., Meng L., Luo M., Li J., Zhou M. Preparation and characterization of uranium–iron triple-bonded $UFe(CO)_3^-$ and $OUFe(CO)_3^-$ complexes. *Angew. Chem.* 2017, *129*, 7036–7040.
146. Feng G., Zhang M., Wang P., Wang S., Maron L., Zhu C. Identification of a uranium–rhodium triple bond in a heterometallic cluster. *Proc. Natl. Acad. Sci. USA* 2019, *116*, 201904895.
147. Ross R. B., Cardona C. M., Guldi D. M., Sankaranarayanan S. G., Reese M. O., Kopidakis N., Peet J., Walker B., Bazan G. C., Van Keuren E., Holloway B. C., Drees M. Endohedral fullerenes for organic photovoltaic devices. *Nat. Mater.* 2009, *8*, 208–212.
148. Shu C.-Y., Wang C.-R., Zhang J.-F., Gibson H. W., Dorn H. C., Corwin F. D., Fatouros P. P., Dennis T. J. S. Organophosphonate functionalized $Gd@C_{82}$ as a magnetic resonance imaging contrast agent. *Chem. Mater.* 2008, *20*, 2106–2109.
149. Liu F., Spree L., Krylov D. S., Velkos G., Avdoshenko S. M., Popov A. A. Single-electron lanthanide-lanthanide bonds inside fullerenes toward robust redox-active molecular magnets. *Acc. Chem. Res.* 2019, *52*, 2981–2993.
150. Zhang K., Wang C., Zhang M., Bai Z., Xie F.-F., Tan Y.-Z., Guo Y., Hu K.-J., Cao L., Zhang S., Tu X., Pan D., Kang L., Chen J., Wu P., Wang X., Wang J., Liu J., Song Y., Wang G., Song F., Ji W., Xie S.-Y., Shi S.-F., Reed M. A., Wang B. A $Gd@C_{82}$ single-molecule electret. *Nat. Nanotechnol.* 2020, *15*, 1019–1024.
151. Akiyama K., Zhao Y., Sueki K., Tsukada K., Haba H., Nagame Y., Kodama T., Suzuki S., Ohtsuki T., Sakaguchi M., Kikuchi K., Katada M., Nakahara H. Isolation and characterization of light actinide metallofullerenes. *J. Am. Chem. Soc.* 2001, *123*, 181–182.
152. Akiyama K., Sueki K., Tsukada K., Yaita T., Miyake Y., Haba H., Asai M., Kodama T., Kikuchi K., Ohtsuki T., Nagame Y., Katada M., Nakahara H. Study of metallofullerenes encapsulating actinides. *J. Nucl. Radiochem. Sci.* 2002, *3*, 151–154.
153. Akiyama K., Sueki K., Haba H., Tsukada K., Asai M., Yaita T., Nagame Y., Kikuchi K., Katada M., Nakahara H. Production and characterization of actinide metallofullerenes. *J. Radioanal. Nucl. Chem.* 2003, *255*, 155–158.
154. Dunk P. W., Kaiser N. K., Mulet-Gas M., Rodríguez-Fortea A., Poblet J. M., Shinohara H., Hendrickson C. L., Marshall A. G., Kroto H. W. The smallest stable fullerene, $M@C_{28}$ (M=Ti, Zr, U): stabilization and growth from carbon vapor. *J. Am. Chem. Soc.* 2012, *134*, 9380–9389.
155. Dai X., Gao Y., Jiang W., Lei Y., Wang Z. $U@C_{28}$: the electronic structure induced by the 32-electron principle. *Phys. Chem. Chem. Phys.* 2015, *17*, 23308–23311.
156. Dai X., Meng Y., Xin M., Wang F., Fei D., Jin M., Wang Z., Zhang R. Energetics and electronic properties of a neutral diuranium molecule encapsulated in C_{90} fullerene. *Procedia Chem.* 2012, *7*, 528–533.
157. Liu X., Li L., Liu B., Wang D., Zhao Y., Gao X. Theoretical study on the ground state structure of uranofullerene $U@C_{82}$. *J. Phys. Chem.* 2012, *116*, 11651–11655.
158. Wu X., Lu X. Dimetalloendofullerene $U_2@C_{60}$ has a U–U multiple bond consisting of sixfold one-electron-two-center bonds. *J. Am. Chem. Soc.* 2007, *129*, 2171–2177.
159. Foroutan-Nejad C., Vícha J., Marek R., Patzschke M., Straka M. Unwilling U–U bonding in $U_2@C_{80}$: cage-driven metal–metal bonds in di-uranium fullerenes. *Phys. Chem. Chem. Phys.* 2015, *17*, 24182–24192.
160. Manna D., Sirohiwal A., Ghanty T. K. $Pu@C_{24}$: a new example satisfying the 32-electron principle. *J. Phys. Chem. C* 2014, *118*, 7211–7221.
161. Dognon J.-P., Clavaguéra C., Pyykkö P. A predicted organometallic series following a 32-electron principle: $an@C_{28}$ (an=Th, Pa^+, U^{2+}, Pu^{4+}). *J. Am. Chem. Soc.* 2009, *131*, 238–243.
162. Ryzhkov M. V., Ivanovskii A. L., Delley B. Electronic structure of endohedral fullerenes $An@C_{28}$ (An=Th–Md). *Comput. Theor. Chem.* 2012, *985*, 46–52.
163. Ryzhkov M. V., Delley B. Electronic structure of predicted endohedral fullerenes $An@C_{40}$ (An=Th–Md). *Comput. Theor. Chem.* 2013, *1013*, 70–77.
164. Manna D., Ghanty T. K. Prediction of a new series of thermodynamically stable Actinide encapsulated fullerene

systems fulfilling the 32-electron principle. *J. Phys. Chem. C* 2012, *116*, 25630–25641.

165. Manna D., Ghanty T. K. Theoretical prediction of icosahedral U@C_{20} and analogous systems with high HOMO–LUMO gap. *J. Phys. Chem. C* 2012, *116*, 16716–16725.
166. Zhao K., Pitzer R. M. Electronic structure of C_{28}, Pa@C_{28}, and U@C_{28}. *J. Phys. Chem.* 1996, *100*, 4798–4802.
167. Manna D., Ghanty T. K. Enhancement in the stability of 36-atom fullerene through encapsulation of a uranium atom. *J. Phys. Chem. C* 2013, *117*, 17859–17869.
168. Muñoz-Castro A. U@C_{36}. Is there enough room for a second uranium? *RSC Adv.* 2016, *6*, 78176–78180.
169. Infante I., Gagliardi L., Scuseria G. E. Is fullerene C_{60} large enough to host a multiply bonded dimetal? *J. Am. Chem. Soc.* 2008, *130*, 7459–7465.
170. Wang Y., Morales-Martínez R., Zhang X., Yang W., Wang Y., Rodríguez-Fortea A., Poblet J. M., Feng L., Wang S., Chen N. Unique four-electron metal-to-cage charge transfer of Th to a C_{82} fullerene cage: complete structural characterization of Th@C_3v(8)–C_{82}. *J. Am. Chem. Soc.* 2017, *139*, 5110–5116.
171. Francis A. H. An Atlas of fullerenes by P. W. Fowler (University of Exeter), D. E. Manolopoulos (University of Nottingham). Oxford: New York. 1995. viii + 392 pp. $98.00. ISBN 0-19-855787-6. J. Am. Chem. Soc. 1996, *118*, 5161.
172. Li Y., Yang L., Wei Z., Hou Q., Li L., Jin P. Robust metal-pentagon interactions in the Th-based endohedral metallofullerenes revealed by DFT calculations. *Int. J. Quant. Chem.* 2019, *119*, e25826.
173. Jin P., Liu C., Li Y., Li L., Zhao Y. Th@C_{76}. Computational characterization of larger actinide endohedral fullerenes. *Int. J. Quant. Chem.* 2018, *118*, e25501.
174. Yang L., Li B., Gu X., Niu K., Jin P. Discovery of non-isolated-pentagon-rule fullerenes from computational characterization of U_2O@C_{72}. *Inorg. Chem.* 2021, *60*, 6492–6502.
175. Hao D., Yang L., Wei Z., Hou Q., Li L., Jin P. U_2O@C_{76}: non-isolated-pentagon-rule cages prevail with the U_2O configuration determined by cage shape and dominated by multicenter bonds. *Inorg. Chem.* 2020, *59*, 7039–7048.
176. Li Y., Yang L., Li Z., Hou Q., Li L., Jin P. U_2C unit in fullerenes: robust multicenter bonds with a cluster shape controlled by cage size and charge transfer. *Inorg. Chem.* 2019, *58*, 10648–10655.
177. Gu Y.-X., Zheng H., Zhao X. Theoretical insight into actinide monometallofullerene Th@C_{74} with four-electron-transfer characteristics. *Chem. Phys.* 2021, *549*, 111258.
178. Zhao P., Zhao X., Ehara M. Theoretical insights into monometallofullerene Th@C_{76}: strong covalent interaction between thorium and the carbon cage. *Inorg. Chem.* 2018, *57*, 2961–2964.
179. Gu Y.-X., Li Q.-Z., Zhao P., Zhao X. Encapsulation of monometal uranium into fullerenes C_{2n} ($2n$ = 70–74): important ionic $U^{4+}C_{2n}{}^{4-}$ characters and covalent U-cage bonding interactions. *Inorg. Chem.* 2019, *58*, 10629–10636.
180. Zhao Y.-X., Li M.-Y., Zhao P., Ehara M., Zhao X. New insight into U@C_{80}: missing U@D_3(31921)–C_{80} and nuanced enantiomers of U@C_1(28324)–C_{80}. *Inorg. Chem.* 2019, *58*, 14159–14166.
181. Zhao Y., Yuan K., Han Y.-B., Li M. Y., Ehara M., Zhao X. Theoretical insight into thermodynamically optimal U@C_{84}: three-electron transfer rather than four-electron transfer. *Inorg. Chem.* 2020, *59*, 12650–12658.
182. Zhao Y.-X., Yuan K., Li M.-Y., Ehara M., Zhao X. In-depth theoretical probe into novel mixed-metal uranium-based endohedral clusterfullerenes Sc_2UX@Ih(31924)–C_{80} (X = C, N). *Inorg. Chem.* 2019, *58*, 10769–10777.
183. Kaminský J., Vícha J., Bouř P., Straka M. Properties of the only thorium fullerene, Th@C_{84}, uncovered. *J. Phys. Chem.* 2017, *121*, 3128–3135.
184. Muñoz-Castro A., King R. B. Th@C_{86}, Th@C_{82}, Th@C_{80}, and Th@C_{76}: role of thorium encapsulation in determining spherical aromatic and bonding properties on medium-sized endohedral metallofullerenes. *Phys. Chem. Chem. Phys.* 2020, *22*, 23920–23928.
185. Jaroš A., Foroutan-Nejad C., Straka M. From π bonds without σ bonds to the longest metal–metal bond ever: a survey on actinide–actinide bonding in fullerenes. *Inorg. Chem.* 2020, *59*, 12608–12615.
186. Cai W., Morales-Martínez R., Zhang X., Najera D., Romero E. L., Metta-Magaña A., Rodríguez-Fortea A., Fortier S., Chen N., Poblet J. M., Echegoyen L. Single crystal structures and theoretical calculations of uranium endohedral metallofullerenes (U@C_{2n}, 2n = 74, 82) show cage isomer dependent oxidation states for U. *Chem. Sci.* 2017, *8*, 5282–5290.
187. Cai W., Abella L., Zhuang J., Zhang X., Feng L., Wang Y., Morales-Martínez R., Esper R., Boero M., Metta-Magaña A., Rodríguez-Fortea A., Poblet J. M., Echegoyen L., Chen N. Synthesis and characterization of non-isolated-pentagon-rule actinide endohedral metallofullerenes U@C_1(17418)–C_{76}, U@C_1(28324)–C_{80}, and Th@C_1(28324)–C_{80}: low-symmetry cage selection directed by a tetravalent ion. *J. Am. Chem. Soc.* 2018, *140*, 18039–18050.
188. Kroto H. W. The stability of the fullerenes Cn, with n = 24, 28, 32, 36, 50, 60 and 70. *Nature* 1987, *329*, 529–531.
189. Wang Y., Morales-Martínez R., Cai W., Zhuang J., Yang W., Echegoyen L., Poblet J. M., Rodríguez-Fortea A., Chen N. Th@C_1(11)–C_{86}: an actinide encapsulated in an unexpected C_{86} fullerene cage. *Chem. Commun.* 2019, *55*, 9271–9274.
190. Jin M., Zhuang J., Wang Y., Yang W., Liu X., Chen N. Th@T_d(19151)–C_{76}: a highly symmetric fullerene cage stabilized by a tetravalent actinide metal ion. *Inorg. Chem.* 2019, *58*, 16722–16726.
191. Yan Y., Morales-Martínez R., Zhuang J., Yao Y.-R., Li X., Poblet J. M., Rodríguez-Fortea A., Chen N. Th@D_5h(6)–C_{80}: a highly symmetric fullerene cage stabilized by a single metal ion. *Chem. Commun.* 2021, *57*, 6624–6627.
192. Meng Q., Morales-Martínez R., Zhuang J., Yao Y.-R., Wang Y., Feng L., Poblet J. M., Rodríguez-Fortea A., Chen N. Synthesis and characterization of two isomers of Th@C_{82}: Th@C_2v(9)–C_{82} and Th@C_2(5)–C_{82}. *Inorg. Chem.* 2021, *60*, 11496–11502.
193. Cai W., Alvarado J., Metta-Magaña A., Chen N., Echegoyen L. Interconversions between uranium mono-metallofullerenes: mechanistic implications and role of asymmetric cages. *J. Am. Chem. Soc.* 2020, *142*, 13112–13119.
194. Yao Y.-R., Roselló Y., Ma L., Puente Santiago A. R., Metta-Magaña A., Chen N., Rodríguez-Fortea A., Poblet J. M., Echegoyen L. Crystallographic characterization of U@C_{2n} (2n = 82–86): insights about metal–cage interactions for mono-metallofullerenes. *J. Am. Chem. Soc.* 2021, *143*, 15309–15318.

195. Boronski J. T., Seed J. A., Hunger D., Woodward A. W., van Slageren J., Wooles A. J., Natrajan L. S., Kaltsoyannis N., Liddle S. T. A crystalline tri-thorium cluster with σ-aromatic metal–metal bonding. *Nature* 2021, *598*, 72–75.
196. Zhang X., Wang Y., Morales-Martínez R., Zhong J., de Graaf C., Rodríguez-Fortea A., Poblet J. M., Echegoyen L., Feng L., Chen N. U_2@Ih(7)–C_{80}: crystallographic characterization of a long-sought dimetallic actinide endohedral fullerene. *J. Am. Chem. Soc.* 2018, *140*, 3907–3915.
197. Hu H.-S., Kaltsoyannis N. The shortest Th–Th distance from a new type of quadruple bond. *Phys. Chem. Chem. Phys.* 2017, *19*, 5070–5076.
198. Ge X., Dai X., Zhou H., Yang Z., Zhou R. Stabilization of open-shell single bonds within endohedral metallofullerene. *Inorg. Chem.* 2020, *59*, 3606–3618.
199. Zhuang J., Morales-Martínez R., Zhang J., Wang Y., Yao Y.-R., Pei C., Rodríguez-Fortea A., Wang S., Echegoyen L., de Graaf C., Poblet J. M., Chen N. Characterization of a strong covalent Th^{3+}–Th^{3+} bond inside an Ih(7)–C_{80} fullerene cage. *Nat. Commun.* 2021, *12*, 2372.
200. Zhang X., Li W., Feng L., Chen X., Hansen A., Grimme S., Fortier S., Sergentu D.-C., Duignan T. J., Autschbach J., Wang S., Wang Y., Velkos G., Popov A. A., Aghdassi N., Duhm S., Li X., Li J., Echegoyen L., Schwarz W. H. E., Chen N. A diuranium carbide cluster stabilized inside a C_{80} fullerene cage. *Nat. Commun.* 2018, *9*, 2753.
201. Fuertes-Espinosa C., Gómez-Torres A., Morales-Martínez R., Rodríguez-Fortea A., García-Simón C., Gándara F., Imaz I., Juanhuix J., Maspoch D., Poblet J. M., Echegoyen L., Ribas X. Purification of uranium-based endohedral metallofullerenes (EMFs) by selective supramolecular encapsulation and release. *Angew. Chem.* 2018, *130*, 11464–11469.
202. Li X., Yao Y.-R., Yang W., Zhuang J., Echegoyen L., Chen N. Crystallographic and spectroscopic characterization of a mixed actinide–lanthanide carbide cluster stabilized inside an Ih(7)–C_{80} fullerene cage. *Chem. Commun.* 2020, *56*, 3867–3870.
203. Zhuang J., Abella L., Sergentu D.-C., Yao Y.-R., Jin M., Yang W., Zhang X., Li X., Zhang D., Zhao Y., Li X., Wang S., Echegoyen L., Autschbach J., Chen N. Diuranium(IV) carbide cluster U_2C_2 stabilized inside fullerene cages. *J. Am. Chem. Soc.* 2019, *141*, 20249–20260.
204. Li X., Roselló Y., Yao Y.-R., Zhuang J., Zhang X., Rodríguez-Fortea A., de Graaf C., Echegoyen L., Poblet J. M., Chen N. U_2N@Ih(7)–C80: fullerene cage encapsulating an unsymmetrical U(iv)=N=U(v) cluster. *Chem. Sci.* 2021, *12*, 282–292.
205. Meng Q., Abella L., Yang W., Yao Y.-R., Liu X., Zhuang J., Li X., Echegoyen L., Autschbach J., Chen N. UCN@Cs(6)–C_{82}: an encapsulated triangular UCN cluster with ambiguous U oxidation state [U(III) versus U(I)]. *J. Am. Chem. Soc.* 2021, *143*, 16226–16234.
206. Ma X., Chai Y., Li P., Wang B. Metal–organic framework films and their potential applications in environmental pollution control. *Acc. Chem. Res.* 2019, *52*, 1461–1470.
207. Liu J., Wöll C. Surface-supported metal–organic framework thin films: fabrication methods, applications, and challenges. *Chem. Soc. Rev.* 2017, *46*, 5730–5770.
208. Hashim M. A., Mukhopadhyay S., Sahu J. N., Sengupta B. Remediation technologies for heavy metal contaminated groundwater. *J. Environ. Manag.* 2011, *92*, 2355–2388.
209. Yu F., Li Y., Han S., Ma J. Adsorptive removal of antibiotics from aqueous solution using carbon materials. *Chemosphere* 2016, *153*, 365–385.
210. Kang K., Dai X., Shen N., Xie R., Zhang X., Lei L., Wang S., Xiao C. Unveiling the uncommon fluorescent recognition mechanism towards pertechnetate using a cationic metal–organic framework bearing N-heterocyclic AIE molecules. *Chem. Eur J.* 2021, *27*, 5632–5637.
211. Zhang N., Sun L.-X., Bai F.-Y., Xing Y.-H. Thorium–organic framework constructed with a semirigid triazine hexacarboxylic acid ligand: unique structure with thorium oxide wheel clusters and iodine adsorption behavior. *Inorg. Chem.* 2020, *59*, 3964–3973.
212. Zhang N., Xing Y.-H., Bai F.-Y. A uranyl-organic framework featuring two-dimensional graphene-like layered topology for efficient iodine and dyes capture. *Inorg. Chem.* 2019, *58*, 6866–6876.
213. Luo F., Fan Y., Feng X., Krishna R., Yin M. Constructing robust gigantic drum-like hydrophobic [$Co_{24}U_6$] nanocage in metal-organic framework for high-performance SO_2 removal at humidity condition. *J. Mater. Chem.* 2021, *9*; https://doi.org/10.1039/D0TA10004H.
214. Jiang Y.-S., Li G.-H., Tian Y., Liao Z.-L., Chen J.-S. Uranyl pyridine-dicarboxylate compounds with clustered water molecules. *Inorg. Chem. Commun.* 2006, *9*, 595–598.
215. Jiang Y.-S., Yu Z.-T., Liao Z.-L., Li G.-H., Chen J. Syntheses and photoluminescent properties of two uranyl-containing compounds with extended structures. *Polyhedron* 2006, *25*, 1359–1366.
216. Guo Y., Li L., Li Y., Li Z., Wang X., Wanggh G. Adsorption and photocatalytic reduction activity of uranium(VI) on zinc oxide/rectorite composite enhanced with methanol as sacrificial organics. *J. Radioanal. Nucl. Chem.* 2016, *310*, 833–890.
217. Yin X., Wang Y., Bai X., Wang Y., Chen L., Xiao C., Diwu J., Du S., Chai Z., Albrecht-Schmitt T. E., Wang S. Rare earth separations by selective borate crystallization. *Nat. Commun.* 2017, *8*, 14438.
218. Yin X., Wang Y., Li X., Xie J., Silver M. A., Chen L., Sheng D., Ji G., Chai Z., Wang S. Competing crystallization between lanthanide and actinide in acidic solution leading to their efficient separation. *Chin. J. Chem.* 2019, *37*, 53–57.
219. Wang Y., Lu H., Dai X., Duan T., Bai X., Cai Y., Yin X., Chen L., Diwu J., Du S., Zhou R., Chai Z., Albrecht-Schmitt T. E., Liu N., Wang S. Facile and efficient decontamination of thorium from rare earths based on selective selenite crystallization. *Inorg. Chem.* 2018, *57*, 1880–1887.
220. Jones D. L., Andrews M. B., Swinburne A. N., Botchway S. W., Ward A. D., Lloyd J. R., Natrajan L. S. Fluorescence spectroscopy and microscopy as tools for monitoring redox transformations of uranium in biological systems. *Chem. Sci.* 2015, *6*, 5133–5138.
221. Xie J., Wang Y., Liu W., Yin X., Chen L., Zou Y., Diwu J., Chai Z., Albrecht-Schmitt T. E., Liu G., Wang S. Highly sensitive detection of ionizing radiations by a photoluminescent uranyl organic framework. *Angew. Chem. Int. Ed.* 2017, *56*, 7500–7504.
222. Xu G., Guo G.-C., Wang M.-S., Zhang Z.-J., Chen W.-T., Huang J.-S. Photochromism of a methyl viologen bismuth(III) chloride: structural variation before and after UV irradiation. *Angew. Chem. Int. Ed.* 2007, *46*, 3249–3251.

223. Li H.-Y., Wei Y.-L., Dong X.-Y., Zang S.-Q., Mak T. C. W. Novel Tb-MOF embedded with viologen species for multi-photofunctionality: photochromism, photomodulated fluorescence, and luminescent pH sensing. *Chem. Mater.* 2015, *27*, 1327–1331.
224. Williams D. E., Martin C. R., Dolgopolova E. A., Swifton A., Godfrey D. C., Ejegbavwo O. A., Pellechia P. J., Smith M. D., Shustova N. B. Flipping the switch: fast photoisomerization in a confined environment. *J. Am. Chem. Soc.* 2018, *140*, 7611–7622.
225. Liu W., Dai X., Xie J., Silver M. A., Zhang D., Wang Y., Cai Y., Diwu J., Wang J., Zhou R., Chai Z., Wang S. Highly sensitive detection of UV radiation using a uranium coordination polymer. *ACS Appl. Mater. Interfaces* 2018, *10*, 4844–4850.
226. Zhang Q., Sun H., Wang X., Hao X., An S. Reversible luminescence modulation upon photochromic reactions in rare-earth doped ferroelectric oxides by in situ photoluminescence spectroscopy. *ACS Appl. Mater. Interfaces* 2015, *7*, 25289–25297.
227. Zhu W., Ma W., Su Y., Chen Z., Chen X., Ma Y., Bai L., Xiao W., Liu T., Zhu H., Liu X., Liu H., Liu X., Yang Y. Low-dose real-time X-ray imaging with nontoxic double perovskite scintillators. *Light Sci. Appl.* 2020, *9*, 1–10.
228. Peng J., Ye K., Xu Y., Cui L., Li R., Peng H., Lin Q. X-ray detection based on crushed perovskite crystal/polymer composites. *Sensor Actuator Phys.* 2020, *312*, 112132.
229. Jones A., Aspinall M., Joyce M. A remotely triggered fast neutron detection instrument based on a plastic organic scintillator. *Rev. Sci. Instrum.* 2018, *89*, 023115.
230. Wang S., Alekseev E. V., Ling J., Liu G., Depmeier W., Albrecht-Schmitt T. E. Polarity and chirality in uranyl borates: insights into understanding the vitrification of nuclear waste and the development of nonlinear optical materials. *Chem. Mater.* 2010, *22*, 2155–2163.
231. Li H., Langer E. M., Kegler P., Modolo G., Alekseev E. V. formation of open framework uranium germanates: the influence of mixed molten flux and charge density dependence in U-silicate and U-germanate families. *Inorg. Chem.* 2018, *57*, 11201–11216.
232. Tian H.-H., Chen L.-T., Zhang R.-L., Zhao J., Liu C.-Y., Weng N. A novel stable 3D luminescent uranyl complex for highly efficient and sensitive recognition of Ru^{3+} and biomolecules. *J. Solid State Chem.* 2017, *258*, 674–681.
233. Wang L., Tu B., Xu W., Fu Y., Zheng Y. Uranyl organic framework as a highly selective and sensitive turn-on and turn-off luminescent sensor for dual functional detection arginine and MnO_4^-. *Inorg. Chem.* 2020, *59*, 5004–5017.
234. Wang L., Xu W., Li W.-Y., Xie M., Zheng Y.-Q. A water-stable uranyl organic framework as a highly selective and sensitive bifunctional luminescent probe for Fe^{3+} and tetracycline hydrochloride. *Chem. Asian J.* 2019, *14*, 4246–4254.
235. Song J., Gao X., Wang Z.-N., Li C.-R., Xu Q., Bai F.-Y., Shi Z.-F., Xing Y.-H. Multifunctional uranyl hybrid materials: structural diversities as a function of pH, luminescence with potential nitrobenzene sensing, and photoelectric behavior as p-type semiconductors. *Inorg. Chem.* 2015, *54*, 9046–9059.
236. Franczyk T. S., Czerwinski K. R., Raymond K. N. Stereognostic coordination chemistry. 1. The design and synthesis of chelators for the uranyl ion. *J. Am. Chem. Soc.* 1992, *114*, 8138–8146.
237. Zhou L., Bosscher M., Zhang C., Özçubukçu S., Zhang L., Zhang W., Li C. J., Liu J., Jensen M. P., Lai L., He C. A protein engineered to bind uranyl selectively and with femtomolar affinity. *Nat. Chem.* 2014, *6*, 236–241.
238. Juillerat C. A., Moore E. E., Besmann T., zur Loye H.-C. Observation of an unusual uranyl cation–cation interaction in the strongly fluorescent layered uranyl phosphates $Rb_6[(UO_2)_7O_4(PO_4)_4]$ and $Cs_6[(UO_2)_7O_4(PO_4)_4]$. *Inorg. Chem.* 2018, *57*, 3675–3678.
239. Liu S.-P., Chen M.-L., Chang B.-C., Lii K.-H. Flux synthesis, crystal structure, and photoluminescence of a heterometallic uranyl-europium germanate with U=O–Eu linkage: $K_4[(UO_2)Eu_2(Ge_2O_7)_2]$. *Inorg. Chem.* 2013, *52*, 3990–3994.
240. Volkringer C., Henry N., Grandjean S., Loiseau T. Uranyl and/or rare-earth mellitates in extended organic–inorganic networks: a unique case of heterometallic cation–cation interaction with UVI=O–LnIII bonding (Ln = Ce, Nd). *J. Am. Chem. Soc.* 2012, *134*, 1275–1283.
241. Liu D.-D., Wang Y.-L., Luo F., Liu Q.-Y. Rare three-dimensional uranyl–biphenyl-3,3′-disulfonyl-4,4′-dicarboxylate frameworks: crystal structures, proton conductivity, and luminescence. *Inorg. Chem.* 2020, *59*, 2952–2960.
242. Liang C., Zhang S., Cheng L., Xie J., Zhai F., He Y., Wang Y., Chai Z., Wang S. Thermoplastic membranes incorporating semiconductive metal–organic frameworks: an advance on flexible X-ray detectors. *Angew. Chem.* 2020, *132*, 11954–11958.
243. Wang Y., Liu X., Li X., Zhai F., Yan S., Liu N., Chai Z., Xu Y., Ouyang X., Wang S. Direct radiation detection by a semiconductive metal–organic framework. *J. Am. Chem. Soc.* 2019, *141*, 8030–8034.
244. Yakunin S., Sytnyk M., Kriegner D., Shrestha S., Richter M., Matt G. J., Azimi H., Brabec C. J., Stangl J., Kovalenko M. V., Heiss W. Detection of X-ray photons by solution-processed lead halide perovskites. *Nat. Photonics* 2015, *9*, 444–449.
245. Mirzaei A., Huh J.-S., Kim S. S., Kim H. W. Room temperature hard radiation detectors based on solid state compound semiconductors: an overview. *Electron. Mater. Lett.* 2018, *14*, 261–287.
246. Hu D., Jiang X. Perspectives for uranyl photoredox catalysis. *Synlett* 2021, *32*, 1330–1342.
247. Li Y., Rizvi S. A.-e.-A., Hu D., Sun D., Gao A., Zhou Y., Li J., Jiang X. Selective late-stage oxygenation of sulfides with ground-state oxygen by uranyl photocatalysis. *Angew. Chem. Int. Ed.* 2019, *58*, 13499–13506.
248. Zhou Y., Hu D., Li D., Jiang X. Uranyl-photocatalyzed hydrolysis of diaryl ethers at ambient environment for the directional degradation of 4-O-5 lignin. *JACS Au* 2021, *1*, 1141–1146.
249. Hu D., Zhou Y., Jiang X. From aniline to phenol: carbon-nitrogen bond activation via uranyl photoredox catalysis. *Natl. Sci. Rev.* 2021, *9*, 156–163.
250. Yu J., Chen S., Liu K., Yuan L., Zhao Y., Chai Z., Mei L. Facile construction of diverse diarylmethane scaffolds via uranyl-catalyzed 1, 6-addition reaction. *Tetrahedron Lett.* 2020, *61*, 152076.
251. Yu J., Zhao C., Zhou R., Gao W., Wang S., Liu K., Chen S., Hu K., Mei L., Yuan L., Chai Z., Hu H., Shi W. Visible-light-enabled C–H functionalization by a direct hydrogen atom transfer uranyl photocatalyst. *Chem. Eur J.* 2020, *26*, 16521–16529.
252. Mao Y., Liu Y., Yu L., Ni S., Wang Y., Pan Y. Uranyl-catalysed C–H alkynylation and olefination. *Org. Chem. Front.* 2021, *8*, 5968–5974.

253. Haber F. *Ammonia*. German patent DE 1909, 229126.
254. Xin X., Douair I., Zhao Y., Wang S., Maron L., Zhu C. Dinitrogen cleavage by a heterometallic cluster featuring multiple uranium–rhodium bonds. *J. Am. Chem. Soc.* 2020, *142*, 15004–15011.
255. Wang P., Douair I., Zhao Y., Wang S., Zhu J., Maron L., Zhu C. Facile dinitrogen and dioxygen cleavage by a uranium(III) complex: cooperativity between the non-innocent ligand and the uranium center. *Angew. Chem. Int. Ed.* 2021, *60*, 473–479.
256. Fang W., Douair I., Hauser A., Li K., Zhao Y., Roesky P. W., Wang S., Maron L., Zhu C. Uranium(III)–Phosphorus(III) synergistic activation of white phosphorus and arsenic. *CCS Chem.* 2021, *4*, 3268–3276.